

Ultraviolet-to-far-infra-red self-consistent analysis of the stellar populations of massive starburst galaxies at intermediate redshifts

Néstor Espino-Briones^{1,2★}, Pablo G. Pérez-González^{3,1}, Jaime Zamorano¹ and Lucía Rodríguez-Muñoz⁴

¹Departamento de Física de la Tierra y Astrofísica, Fac. CC. Físicas, Universidad Complutense de Madrid, Plaza de las Ciencias 1, Madrid, E-28040, Spain

²Instituto Nacional de Astrofísica, Óptica y Electrónica, Luis E. Erro No. 1, Tonantzintla, C.P. 72840, Puebla, México

³Centro de Astrobiología, Instituto Nacional de Técnica Aeroespacial, Carretera de Ajalvir km 4, Torrejón de Ardoz, Madrid, E-28850, Spain

⁴Dipartimento di Fisica e Astronomia “Galileo Galilei”, Università degli Studi di Padova, Vicolo dell’Osservatorio 3, I-35122 Padova, Italy

Accepted 2022 March 9. Received 2022 March 4; in original form 2021 August 23

ABSTRACT

We study in detail the properties of the stellar populations of 111 massive ($\log(M_\star/M_\odot) \geq 10$) dusty (FIR-selected) starburst ($SFR/SFR_{\text{MS}} > 2$) galaxies at $0.7 < z < 1.2$. For that purpose, we use self-consistent methods that analyse the UV-to-FIR broadband observations in terms of the stellar light and dust re-emission with energy-balance techniques. We find that the emission of our starburst galaxies can be interpreted as a recent star formation episode superimposed on a more evolved stellar population. On average, the burst age is ~ 80 Myr and its attenuation ~ 2.4 mag. Assuming our starburst galaxies at half their lifetimes, we infer a duration of the starburst phase of ~ 160 Myr. The median stellar mass and SFR are $\log(M_\star/M_\odot) \sim 10.6$ and $\sim 220 M_\odot \text{ yr}^{-1}$. Assuming this SFR and the inferred duration of the starburst phase, the stellar mass added during this phase corresponds to ~ 40 per cent the median stellar mass of our sample. The young-population age determines the position of our galaxies in the $M_\star - SFR$ plane. Galaxies located at the largest distances of the MS present shorter young-population ages. The properties of the underlying stellar population cannot be constrained accurately with our broadband data. We also discuss the impact of including the FIR data and energy-balance techniques in the analysis of the properties of the stellar populations in starburst galaxies.

Key words: galaxies – galaxies: starburst – galaxies: photometry – infrared: galaxies – galaxies: evolution

1 INTRODUCTION

Studying the processes governing the formation and evolution of galaxies, deep optical and infra-red (IR) surveys have determined that most of the star-forming galaxies up to $z \sim 5$ exhibit a correlation between their stellar mass (M_\star) and star formation rate (SFR), which is alluded to as main sequence (MS; e.g., Noeske et al. 2007; Salim et al. 2007; Drory & Alvarez 2008). The scatter of the MS at fixed stellar mass is modest (~ 0.3 dex; e.g., Noeske et al. 2007; Kurczynski et al. 2016), which is explained as evidence of a steady star-formation mode which requires smooth gas accretion from the intergalactic medium (Renzini 2009; Genzel et al. 2010). The outliers above the MS are classified as starburst¹ galaxies. Examples of these objects with very prominent star formation are typically dust-enshrouded systems

like ultra luminous red galaxies (ULIRGs, Sanders & Mirabel 1996; Elbaz et al. 2007), and high-redshift ($z \gtrsim 2$) submillimetre galaxies (SMGs; Tacconi et al. 2008; Gómez-Guijarro et al. 2018). Dusty star-forming galaxies (dSFGs) dominate the star-forming population in the mass range $\log(M_\star/M_\odot) \sim 10.0 - 10.5$ at $z < 1.5$, and they are a factor 3 – 5 more important than unobscured star-forming galaxies at $\log(M_\star/M_\odot) \gtrsim 10.5$ (Martis et al. 2016). For $\log(M_\star/M_\odot) > 10.5$ and at $0 < z < 2.5$, more than 90 per cent of the total (ultraviolet+IR) star formation is obscured (Whitaker et al. 2017). Novel observations have disclosed the appearance of a significant dusty starburst population up to $z \sim 4 - 5$ (Bisigello et al. 2018; Donevski et al. 2020).

The elevated SFR s of starbursts are probably triggered by extreme processes like mergers (e.g., Di Matteo et al. 2008; Cibinel et al. 2019) or disc instabilities (e.g., Ceverino et al. 2010; Romeo & Fathi 2016). These intense SFR s are expected to persist for short time-scales ($\sim 100 - 400$ Myr; Tacconi et al. 2008; Miettinen et al. 2017) due to the limited gas supply.

A distinct interpretation for starbursts –derived from $z \gtrsim 1$ far-IR (FIR) selected samples– suggests that outliers of the MS

★ E-mail: nespino@ucm.es, permanent: nespitron@gmail.com

¹ In this paper, we use the term ‘starburst’ to refer to galaxies whose SFR is at least twice that on the MS at fixed M_\star (i.e., 1σ above the MS), and the term ‘starburst phase’ to allude to the time-scale in which such elevated SFR is sustained.

correspond to high specific SFR galaxies housing young stellar populations. These galaxies are captured while still assembling most of their M_\star in order to arrive to the MS (Mancuso et al. 2016).

A way to understand the starburst event in the evolution of galaxies is estimating their physical properties, e.g., M_\star and SFR . For that purpose, multi-wavelength observations are typically used, normally biased towards the rest-frame ultraviolet (UV) and optical ranges. However, for dusty starbursts, the impact of dust in the spectral energy distributions (SEDs) of galaxies—absorbing the UV to near infra-red (NIR) photons—is very significant. Consequently, only taking into account that this absorbed energy is re-emitted in the FIR window, we can more robustly determine the stellar population properties of starburst galaxies.

Stellar population synthesis (SPS) models are widely used to extract the physical properties of dusty starbursts. Going beyond the determination of basic properties such as M_\star and SFR , they can also be used to explore star formation histories (SFHs), stellar ages, and dust content of galaxies from their observed UV-to-FIR SEDs (see review in Conroy 2013).

The gross effect of dust attenuation in the emission of the stellar populations of a galaxy is typically represented with an attenuation curve (e.g., Calzetti et al. 2000; Charlot & Fall 2000). The amount of dust attenuation needs to be heavily constrained in order to avoid an age-attenuation degeneracy (Pforr et al. 2012; Conroy 2013). FIR data can help to constrain the stellar-light attenuation, if it is imposed an energy balance between the stellar light absorbed by dust and its re-emission (Takagi et al. 1999; Burgarella et al. 2005). Hence, energy-balance techniques arise as a good choice to model the observed UV-to-FIR SEDs of dusty starbursts (e.g., da Cunha et al. 2008; Noll et al. 2009).

The possibility to carry out a detailed analysis of the dust emission from intermediate redshift galaxies has been significantly enhanced by missions such as *Spitzer* and *Herschel*. The *Herschel Space Observatory* (Pilbratt et al. 2010) observed at FIR wavelengths across and beyond the dust-emission peak of starburst galaxies allowing to constrain properly their total IR luminosity (L_{TIR}^2). The Spectral and Photometric Image REceiver (SPIRE; Griffin et al. 2010) mapped $\sim 350 \text{ deg}^2$ at 250, 350 and 500 μm for the *Herschel* Multi-tiered Extragalactic Survey (HerMES; Oliver et al. 2012). The large area surveys carried out by IR missions are limited in depth restricting statistical studies to the most luminous and massive sources. Nevertheless, dust-obscured star formation is paramount to understand the cosmic evolution of the star-forming population.

The main goal of this paper is understanding the implications of the starburst event in terms of the stellar population properties of galaxies above the MS. For that purpose, we aim at determining such properties at intermediate ($z \sim 1$) redshift, an epoch when dSFGs practically dominate the production of stars in the Universe (e.g., Pérez-González et al. 2005; Le Floch et al. 2005; Casey et al. 2014). We use a FIR-selected sample to ensure that we constrain the peak of the dust emission in an accurate manner, and thus we select bona fide starburst galaxies. These ~ 100 dusty starbursts are introduced making publicly available their UV-to-FIR photometry. Combining these multi-wavelength data, we fit observed UV-to-FIR SEDs with self-consistent models that consider the obscuration of starlight and dust emission with energy-balance techniques. We use two codes which manage this self-consistent analysis to determine the stellar-population properties of our dusty starburst sample. Utilising different codes, we assess the robustness and identify systemat-

ics on the derived solutions. Considering the dusty and starbursting nature of our objects, the method we use is fitting two stellar populations (depicted by a young population on top of an evolved one) models to their observed SED with and without FIR data. By doing this, we check the impact of the FIR information in breaking the age-attenuation degeneracy and in the derivation of stellar parameters. In particular, we investigate the time-scales of galaxies in the starburst phase, and the amount of stellar mass assembled in such phase.

The paper is structured as follows: In Section 2 we detail the multi-wavelength data compiled and catalogued for this work. Section 3 describes our FIR photometric extraction and band-merging methodology. In Section 4, we detail our procedure to derive photometric redshifts, and to select massive dusty starbursts using such photometric and spectroscopic redshift estimates. Section 5 explains our auto-consistent SED fitting methods to explore the stellar properties of dusty starbursts. In Section 6, we assess the importance of the FIR-data usage in the determination of such properties. Section 7 contextualises our characterization of the starburst stellar parameters with other samples. Finally, a summary and the main conclusions of this work are given in Section 8.

Throughout, we adopt $\Omega_M = 0.3$, $\Omega_\Lambda = 0.7$, $h = 0.7$ cosmology. All magnitudes quoted are in AB system. All statistical properties are reported as 50th^{+to 84th percentile}_{-to 16th percentile}.

2 DATA DESCRIPTION AND REDUCTION

This work is based on the analysis of a sample of galaxies selected in the *Subaru/XMM-Newton* Deep Survey field (SXDS³; $\alpha = 02^{\text{h}}18^{\text{m}}00^{\text{s}}$, $\delta = -05^\circ00'00''$). This field is a broad-area ($\sim 1 \text{ deg}^2$) sky region counting with multi-wavelength data gathered for studying the evolution of galaxies and the nature of extragalactic X-ray sources (Furusawa et al. 2008). We have collected a variety of UV-to-FIR observations, the main characteristics of these data are described in Table 1 and in the following Subsections. Since in this work we are interested in IR-bright galaxies, we first describe the *Spitzer* and *Herschel* data used to select the sample of FIR emitters, and then we present the rest of ancillary datasets assembled for our analysis.

2.1 *Spitzer* data

Spitzer observations of the SXDS/UDS field with both the IRAC and MIPS instruments were carried out within the legacy program for UDS (hereafter SpUDS; Dunlop et al. 2007). The available basic calibrated data (BCD) products for all wavelengths between 3.6 and 70 μm were downloaded from the *Spitzer* heritage archive, reduced and calibrated.

For the MIPS-24 data, artefact and background removal, flat-fielding and mosaicking were done using MOPEX (version 18.3.1; Makovoz & Khan 2005). We used an output square pixel of 1.2 arcsec. The average exposure time is $\sim 3300 \text{ s}$ per pixel. Source detection and photometry for the MIPS-24 mosaic were carried out with an iterative procedure, which uses a point spread function (PSF) technique plus aperture correction (see, e.g., Pérez-González et al. 2005). We identified sources with SEXTRACTOR (Bertin & Arnouts 1996) using the coverage map as a weighting image, performing a

² Hereafter, the integrated luminosity from 8 to 1000 μm .

³ The SXDS field is also referred as the UDS (ultra deep survey) included in the *UKIRT* infrared deep sky survey (UKIDSS; Lawrence et al. 2007)

series of detection passes to remove bright sources and allow the detection of fainter emitters. Photometry was measured following a PSF-fitting method and using the *phot* and *allstar* tasks from the DAOPHOT package in the Image Reduction and Analysis Facility (IRAF⁴). Given the full width half maximum (FWHM) of the MIPS-24 PSF (~ 6 arcsec), some sources are overlapped. Although *allstar* deals with this crowdedness effectuating concurrent fits to multiple objects, six passes were required to recover the faintest sources. We extracted PSF photometry from all the sources of these passes together. The errors of the MIPS-24 photometry were derived from the sky uncertainty. The largest sky rms determination between *phot* and *allstar* is compared with 3 other sky rms estimates (as described in appendix A of Pérez-González et al. 2008). The final error is set to the largest value of the 5 estimations. Our final MIPS-24 catalogue has a median 5σ threshold of ~ 70 μ Jy.

For the MIPS-70 data, dark horizontal and vertical stripes were removed by filtering with the *cleanup70.tcsh* script of the germanium reprocessing tools (GERT) and the mosaic was built with MOPEX. The presence of bright sources in the mosaic produces a boost of the filtering effect, causing a partial subtraction of source flux. We got rid of such problem following the procedure described in Frayer et al. (2009, see their sections 3.1–3.3). Our final mosaic has a square-pixel size of 4.0 arcsec, and an average exposure time of ~ 1430 s per pixel. MIPS-70 photometry was also carried out with a PSF technique plus aperture correction, but using a prior-based method which takes advantage of the depth of the IRAC and MIPS-24 observations (see Section 3.1). The errors of the MIPS-70 photometry were estimated from the sky uncertainty in a similar way to that described for the MIPS-24 photometry. Our final MIPS-70 catalogue has median 5σ threshold of ~ 9 mJy.

To check the robustness of our MIPS catalogues, we computed differential source number counts, and we compared them with MIPS counts presented in the literature. For the MIPS-24 data, our results and those of Papovich et al. (2004) present differences smaller than 10 per cent in median for the flux interval $0.07 - 5$ mJy. For the MIPS-70 data, our results are consistent within 5 per cent with those derived by Frayer et al. (2006) for GOODS-N at flux densities between $\sim 6 - 10$ mJy (after performing completeness corrections). Our values are also compatible within 20 per cent with the results estimated by Frayer et al. (2009) for COSMOS within the flux range $\sim 10 - 100$ mJy.

SpUDS IRAC observations were carried out in map mode for its four channels, 3.6, 4.5, 5.8, and 8.0 μ m. The average exposure time per pixel is ~ 8700 s for the 4 channels. All the data were reduced with the *Spitzer* pipeline which produces BCD, and were mosaicked using the technique of Huang et al. (2004), which comprises pointing honing, distortion correction, and mosaicking using a pixel scale half of the original (~ 0.6 arcsec) with a drizzling strategy. Source extraction and photometry were performed as explained in the appendix A of Pérez-González et al. (2008). We detected sources with SEXTRACTOR in the 3.6 and 4.5- μ m images separately, and then we combined both lists of sources. Aperture photometry was determined for each channel IRAC image, fixing the IRAC 3.6 + 4.5 positions in the four IRAC bands, and forcing measurements. We obtained final integrated fluxes measuring in circular apertures of 2-arcsec radius, and applying aperture corrections

based on empirical PSFs. The limiting magnitudes (defined as the third quartile of the magnitude distribution of our sample, hereafter also for mid-infrared (MIR), NIR, UV and optical data) are indicated in Table 1. The photometric uncertainties in the IRAC catalogues were set to the largest value obtained with the 3 sky rms estimates method described in the appendix A of Pérez-González et al. (2008).

2.2 Herschel data

The FIR information used in this study includes Photodetector Array Camera and Spectrometer (PACS; Poglitsch et al. 2010) and SPIRE data for the UDS field, which was observed as part of the key program guaranteed time (KPGT) HerMES. We downloaded all public PACS data inside the UDS region from the *Herschel* science archive, including targets with longer exposure time as: UDS-SCUBA (also for HerMES), and the open-time cycle 2 (OT2) UDS-CANDELS (PI Mark Dickinson). Regarding SPIRE, we downloaded also data from shallow observations taken using PACS/SPIRE parallel mode (for XMM VIDEO 1, which is in HerMES too) and data from deep observations taken by UDS-CANDELS. We built the mosaics using the *Herschel* interactive processing environment (HIPE) version 11, which includes the common PACS (Wieprecht et al. 2009) and SPIRE (Dowell et al. 2010) photometer pipelines, and some tailor-made methods for reducing data of both instruments.

We used output pixel sizes of 1.2 and 2.4 arcsec for the PACS 100 and 160- μ m mosaics. Source detection and photometry, for both PACS bands, were carried out based in a prior-position method (see Section 3.1) and PSF (FWHM $\sim 7, 12$ arcsec for the green and red filters) fitting. We applied correction factors to the PACS fluxes to account for the finite sizes of the PSFs and for losses due to the high-pass filtering performed by the reduction pipeline (Popesso et al. 2012; Balog et al. 2014). The errors of the PACS 100 and 160- μ m photometry were estimated from the sky uncertainty in a similar way to that described for the MIPS-24 photometry (see Section 2.1). Considering that we have used PACS data with different exposure times, and that such differences are appreciable in the sky level of the mosaic, we did catalogues for 3 different areas: UDS-CANDELS, UDS-SCUBA and UDS-NORMAL. The median 5σ sensitivities of the PACS filters in these areas are detailed in Table 1.

The SPIRE observations of the SXDS/UDS field were done in scan map mode. Timelines are processed for each bolometer in the 3 channels, using the SPIRE photometer pipeline. The timelines of the full set of observations were gridded on to sky to create the mosaics for each bolometer array. These mosaics were made using the destriper algorithm and the naive map-maker (Roseboom et al. 2010; Smith et al. 2012), included in HIPE, with default pixel sizes of 6, 10 and 14 arcsec for the 250, 350 and 500- μ m bands.

The PSF sizes of the SPIRE channels are large (FWHM $\sim 18, 25$ and 36 arcsec), and the 3 bands are confusion limited ($5\sigma_{\text{conf}} \sim 29, 32, 34$ mJy; Nguyen et al. 2010). Source detection and photometry for the 3 SPIRE bands were also carried out with a prior-position method (see Section 3.1) and PSF fitting. Then, we applied a calibration based on the beam sizes which were assumed Gaussians, and a correction factor (~ 10 per cent) to consider losses due to pixelation in the PSFs. The errors of the SPIRE 250, 350 and 500- μ m photometry were estimated from the sky uncertainty (see Section 2.1). Although we used SPIRE data with different exposure times inside the UDS region, the background of the SPIRE maps appears uniform. The final catalogues have median 5σ thresholds of $\sim 13, 18$, and 18 mJy for the SPIRE 250, 350 and 500- μ m channels.

⁴ IRAF is distributed by the national optical astronomy observatory, which is operated by the association of universities for research in astronomy (AURA), Inc., under cooperative agreement with the national science foundation.

Table 1. Characteristics of the data compiled for the SXDS/UDS field. (1) Name of the observing band. (2) Effective wavelength of the filter+detector. (3) Third quartile of the magnitude (flux) distribution (limiting magnitudes for the FUV to IRAC-8.0 bands). (4) Magnitudes (fluxes) of a detection with SNR=5. (5) Median of the PSF FWHM in arcseconds. (6) Area covered by the surveys in deg^2 . (7) Source density per square arcminute up to the m_{Q_3} for FUV to 8- μm bands and up to $m_{5\sigma}$ for the 24 to 500- μm channels. (8) Source from which the data were obtained.

^a PACS limiting magnitudes for regions with different exposure time: UDS-CANDELS, UDS-SCUBA, and UDS-NORMAL, respectively. ^a *Spitzer* Program #40021 (PI: Dunlop). ^b *Herschel* Program, Proposal ID: KPGT_soliver_1 (PI: Oliver). ^c *Herschel* Program, Proposal ID: OT2_mdickins_1 (PI: Dickinson)

	Band (1)	λ_{eff} (2)	m_{Q_3} (3)	$m_{5\sigma}$ (4)	FWHM (5)	Area (6)	Surf. Dens. (7)	Source (8)
UV, optical and NIR Data	FUV	153.9 nm	24.8	24.4	5.5	3.2	2.0	GALEX GTO
	NUV	231.6 nm	24.4	24.2	5.5	3.2	4.4	GALEX GTO
	<i>B</i>	441.9 nm	27.6	29.2	0.9	1.2	135.3	Subaru/Suprime-Cam
	<i>V</i>	545.6 nm	27.3	28.9	0.9	1.2	143.9	Subaru/Suprime-Cam
	<i>R_c</i>	651.8 nm	27.1	28.8	0.8	1.2	130.2	Subaru/Suprime-Cam
	<i>i'</i>	766.9 nm	27.0	28.7	0.9	1.2	137.3	Subaru/Suprime-Cam
	<i>z'</i>	906.8 nm	26.4	28.0	0.9	1.2	108.9	Subaru/Suprime-Cam
	<i>J</i>	1.25 μm	24.2	25.4	0.8	0.8	55.3	UKIRT/WFCAM
	<i>H</i>	1.64 μm	23.0	24.1	0.8	0.8	40.3	UKIRT/WFCAM
	<i>K</i>	2.21 μm	22.9	24.1	0.8	0.8	56.7	UKIRT/WFCAM
Mid/Far Infrared Data	IRAC-3.6	3.56 μm	24.2	23.1	2.1	1.0	36.6	<i>Spitzer</i> GTO ^a
	IRAC-4.5	4.50 μm	24.3	23.2	2.1	1.0	35.1	<i>Spitzer</i> GTO ^a
	IRAC-5.8	5.74 μm	23.3	22.0	2.3	1.0	25.9	<i>Spitzer</i> GTO ^a
	IRAC-8.0	7.93 μm	23.3	21.8	2.3	1.0	23.9	<i>Spitzer</i> GTO ^a
	MIPS-24	23.8 μm	19.4 (63 μJy)	19.3 (70 μJy)	6	1.2	6.0	<i>Spitzer</i> GTO ^a
	MIPS-70	72.5 μm	14.7 (5 mJy)	14.0 (9 mJy)	18	1.2	0.1	<i>Spitzer</i> GTO ^a
	PACS-100 ^a	102.4 μm	...	16.3 (1.1 mJy)	7	0.1	4.2	<i>Herschel</i> OT2 ^c
			...	15.4 (2.4 mJy)		0.2	1.3	<i>Herschel</i> KPGT ^b
			...	14.9 (4.1 mJy)		0.6	0.7	<i>Herschel</i> KPGT ^b
	PACS-160 ^a	165.6 μm	...	15.2 (3.1 mJy)	12	0.1	3.3	<i>Herschel</i> OT2 ^c
			...	14.5 (5.8 mJy)		0.2	1.5	<i>Herschel</i> KPGT ^b
			...	14.0 (8.9 mJy)		0.6	0.8	<i>Herschel</i> KPGT ^b
	SPIRE-250	253.2 μm	14.7 (4.8 mJy)	13.6 (13 mJy)	18	2.0	0.8	<i>Herschel</i> KPGT ^b
	SPIRE-350	355.9 μm	14.6 (5.5 mJy)	13.3 (18 mJy)	26	2.0	0.2	<i>Herschel</i> KPGT ^b
	SPIRE-500	511.3 μm	14.6 (5.5 mJy)	13.3 (18 mJy)	36	2.0	0.1	<i>Herschel</i> KPGT ^b

To test the reliability of our *Herschel* catalogues, we computed source differential number counts, and we compared them with literature. For our final sample of starbursts (see Section 4.2), fractions of ~ 92 and ~ 91 per cent of the flux measurements are in the ranges $\sim 4 - 40$ and $\sim 7 - 60$ mJy for PACS-100 and -160, respectively. For these flux ranges, our counts present differences smaller than 25 and 20 per cent with the previous estimates for different fields of Berta et al. (2011) and Magnelli et al. (2013). For the SPIRE channels, the flux densities of our starburst sample range in $\sim 10 - 95$, $\sim 15 - 60$, and $\sim 15 - 35$ mJy for 250, 350 and 500 μm , respectively. In these flux ranges, our counts show differences smaller than 15, 20 and 20 per cent with the earlier estimations of Oliver et al. (2010) for HerMES, and the ones of Béthermin et al. (2012) for COSMOS and GOODS-N. For the SPIRE bands, we also compared the flux densities estimated for our starburst sample in our prior-based catalogue (see Section 3.1) with those provided by Swinbank et al. (2014, estimated with priors too). Both methods yield compatible SPIRE flux densities to $\lesssim 20$ per cent accuracy.

2.3 UV, optical, NIR and spectroscopic data

In this Section, we describe the UV-to-NIR and spectroscopic datasets of the SXDS/UDS field compiled for counterpart identification of each FIR emitter, and photometric redshift estimations. Table 1 summarises the main characteristics of all data collections including wavelengths, the third quartile of the source magnitude distribution (giving information about the depth of the catalogs), magnitudes corresponding to the 5σ threshold above the sky level, FWHM of the PSFs, areas of the surveys, source number densities, and the survey from which data were obtained for each band.

The *Galaxy evolution explorer* (GALEX; Martin et al. 2005) observed the SXDS field, as a part of the data for *XMM-Newton* large scale structure survey, in both GALEX filters. We downloaded the reduced images and photometric catalogues for the area overlapping with the SXDS/UDS field. These images have an average exposure time of ~ 24 ks in both channels.

The ground-based optical imaging of the SXDS field was taken with Suprime-Cam (Miyazaki et al. 2002) on the *Subaru* tele-

scope. Five continuous cross-shaped Suprime-Cam pointings were required to cover the SXDS field. The *Subaru* imaging data used in our study comprised the broadband filters B , V , R_c , i' and z' . We downloaded the five tile images of each one of the 5 filters for SXDS data release 1. Then, we performed source detection and photometry using *SEXTRACTOR* with typical methods.

The SXDS field was also observed with the *United Kingdom infrared* telescope wide field camera (*UKIRT* WFCAM; Casali et al. 2007) for the ultra deep survey (UDS; Almani et al. in preparation) which is the deepest constituent of the *UKIRT* infrared deep sky survey (UKIDSS; Lawrence et al. 2007). The area of the UDS field was covered using the nominal observing mode. The UDS data used in our study encompass imaging in the broadband filters J , H and K . We downloaded the four tiles of object and confidence images for these 3 filters from WFCAM science archive in its data release 8. We carried out source extraction and photometry in each filter tile using *SEXTRACTOR* with standard procedures.

Various surveys have done a spectroscopic follow-up in the SXDS/UDS field. Multi-object spectra were taken by Geach et al. (2007) using the low-dispersion survey spectrograph (LDSS2) on the *Magellan* telescope. They were studying galaxies belonging to groups and clusters at $z \sim 0.5$. Spectra of galaxies of a cluster candidate at $z \sim 1.4$ were obtained by van Breukelen et al. (2007) using the deep imaging multi-object spectrograph (DEIMOS) on the *Keck-2* telescope. Faint quasi-stellar objects at $1.57 < z < 3.29$ were followed by Smail et al. (2008) using the AAOmega spectrograph on the *Anglo-Australian* telescope. X-ray sources were also followed using the faint object camera spectrograph (FOCAS) on the *Subaru* telescope by Akiyama et al. (2015), who also observed the bright sources in the SXDS region with the 2-degree field (2dF) spectrograph, obtaining redshifts in the range $0.1 < z < 4.0$. The UDSz program (PI O. Almaini; see also McLure et al. 2013; Bradshaw et al. 2013) has targeted ~ 3500 NIR-selected galaxies using the focal reducer and low-dispersion spectrograph (FORS2) or the visible multi-object spectrograph (VIMOS), obtaining 1512 secure redshifts in the range $0 < z < 4.8$.

3 FAR INFRARED AND MERGED CATALOGUES

In this Section, we present the prior-based FIR photometric catalogues and the band-merging technique used to characterize our sources through the analysis of UV-to-FIR SEDs.

The FIR photometric extraction follows the method described in Pérez-González et al. (2010); see also Rawle et al. (2016) and Rodríguez-Muñoz et al. (2019). The UV-to-FIR spectro-photometric merged catalogue of the SXDS/UDS field was built within the RAINBOW cosmological database⁵ scheme (Pérez-González et al. 2008; Barro et al. 2011a). We briefly describe these methods in the following 2 Subsections.

3.1 Prior-based FIR cataloguing

Our method to detect sources in the MIPS-70, PACS, and SPIRE data combines high-confidence direct-detection positions (see Section 2.1) with prior-based positions.

First, we cross-correlated the MIPS-70 direct-detection catalogue with the MIPS-24 one in a 3-arcsec radius. We compared the WCS of both catalogues, getting an rms accuracy smaller than

1.4 arcsec. The PACS, and SPIRE-250 mosaics were aligned to MIPS-24 astrometry using an overall X-Y offset based on the positions of the brightest (few tens) *Herschel* point sources, obtaining a WCS rms accuracy smaller than 0.9, 1.3, and 3 arcsec between the MIPS-24, and PACS-100/160, and SPIRE-250 mosaics. The SPIRE-350 and -500 images were aligned to the WCS of the SPIRE-250 and -350 mosaics, getting WCS alignments with rms smaller than 5 and 7 arcsec between the SPIRE 350 and 250, and the 500 and 350- μ m maps, respectively. Thus, the overall WCS rms accuracy obtained for each FIR band is smaller or similar than half of its pixel size.

Source detection and photometry in the MIPS-70 and *Herschel* bands depend on the prior catalogues obtained using the higher-spatial resolution IRAC and MIPS-24 mosaics, and on direct detections on each FIR band. The different PSF sizes of the IRAC and MIPS-24 filters compared to the MIPS-70 and *Herschel* bands implied that we may have several prior sources merged in one single source in the redder bands, i.e., we assumed that sources that can be deblended in longer wavelength data must be separated by a minimum distance. We did some testing to find the optimal distance for each FIR band. In order to cope with this, 2 procedures were implemented. First, the IRAC and MIPS-24 prior catalogues were cut to a 5σ threshold to avoid spurious identifications in the FIR catalogues. Then, we purged the input prior list by substituting close (within distances smaller than the MIPS-70 and *Herschel* PSF FWHM) groups of prior sources with a single pseudo-source located in the position of the brightest source of that group. The adoption of a position for a pseudo-source is not crucial, because small centring offsets are permitted within the concurrent PSF fitting method.

For the MIPS-70 map, we grouped prior positions within $3/4$ of the MIPS-70 FWHM diameters of each other. We combined the purged list of prior sources with the $\geq 5\sigma$ direct-detection MIPS-70 list and applied the PSF fitting technique as described in Section 2.1.

For the PACS maps, we combined positions obtained by direct detections from several passes in the respective mosaic, with those of the prior sources inside each PACS map. We dealt with the different PSF sizes of the IRAC and MIPS-24 bands, and the PACS channels by grouping objects within 5 and 7 arcsec diameters of a given candidate for the 100 and 160- μ m filters, keeping only a direct detection or a pseudo-source. We fitted empirical PSFs to the purged candidate list of each band as explained in Section 2.2, tolerating small concomitant recentring offsets.

For the SPIRE-250 map, the same procedure used for PACS mosaics was followed, changing the prior catalogue grouping diameter to 12 arcsec. For the SPIRE-350 and 500- μ m mosaics, we used as prior 250 and 350- μ m source positions, respectively. For these two redder channels, the grouping diameters were 12 and 17 arcsec, but we gave preference to prior positions compared to direct-detection ones. We employed the PSF fitting technique fed by the purged list of candidates of the 3 channels as described in Section 2.2. We did not allow recentring in the *phot+allstar* tasks for the 350 and 500- μ m bands. Then, the final detections in the 350 and 500- μ m bands are based on SPIRE-250 positions.

3.2 Spectro-photometric merged catalogues

Our main goal is studying the relation between the stellar and dust emission of starburst galaxies, which requires UV-optical-NIR SEDs for each FIR source. In this work, we have focused on the common ~ 0.7 deg² surveyed by *Spitzer*, *Herschel*, *Subaru* and *UKIRT* telescopes, selecting galaxies in the FIR and looking for counter-

⁵ https://arcoirix.cab.inta-csic.es/Rainbow_navigator_public/

parts in the other datasets. Our selection includes objects with at least 2 MIPS-70 and/or *Herschel* fluxes above a 4σ threshold and a 5 σ MIPS-24 detection, which acts as a bridge between the wide-beam FIR bands and the higher spatial resolution UV/optical/NIR filters.

The RAINBOW code matches the source coordinates from a master selection catalogue (24 μm in our case) to a referential optical band (R_c in our study). This reference helps to diminish the radius of the subsequent cross-correlations with the other photometric bands and the spectroscopic catalogue. A 2.5-arcsec radius was used to match the positions of the 24- μm source list and the R_c objects. Within this radius, multiple optical identifications were found for several sources (20 per cent of the total number of MIPS-24 emitters). In such case, all optical objects within this radius were kept as possible counterpart for the 24- μm source. Starting from the R_c coordinates, aperture-matched photometry was carried out in the available UV, optical, NIR, and IRAC bands, and we also looked for a spectroscopic redshift using a 0.8-arcsec search radius. Photometric uncertainties from optical to IRAC images are computed, concurrently to the measurement of flux density, using the 3 estimates method mentioned in Section 2.1 (for a full description of the RAINBOW procedures, see Pérez-González et al. 2008; Barro et al. 2011a).

Considering the different PSF sizes for the MIPS-70 and *Herschel* channels, distinct radii were used to cross-match the referential identifications with the FIR bands (4.0, 2.8, 3.5, 6.0, 9.0 and 12.0 arcsec for MIPS 70 μm , PACS 100 and 160 μm , SPIRE 250, 350 and 500 μm). For the MIPS and *Herschel* channels, the integrated flux was assumed to be that determined from the PSF fitting and aperture correction (see Sections 2.1 and 2.2). In the case of multiple referential identifications, i.e., multiple sources in the optical/NIR bands matching the same FIR detection, we have assigned to these multiple identifications only one FIR counterpart, their corresponding match from each one of the MIPS and *Herschel* channels.

It is interesting to evaluate how many 24- μm sources are associated to a given 4σ source detected at longer wavelengths. On average, one MIPS-70, PACS or SPIRE-250 source can be identified with ~ 1.3 MIPS-24 objects. In particular, a significant fraction of ~ 80 per cent of MIPS-70, PACS or SPIRE-250 sources have only one MIPS-24 counterpart, ~ 10 per cent have 2, and ~ 10 per cent have more than 2. For 350 and 500- μm sources the average number of MIPS-24 possible counterparts rises to ~ 2 .

We might also consider how many optical counterparts are associated to the 4σ -FIR identifications for the multi-wavelength catalogue. The fraction of MIPS-70, PACS-100/160 objects with 1 and 2 optical counterpart(s) is ~ 70 and 20 per cent, and the fraction of sources with more than 2 associations is ~ 10 per cent in both cases. A fraction of ~ 60 per cent of SPIRE-250 objects have only one optical counterpart, ~ 35 per cent have 2-3 optical matches, and ~ 5 per cent have more than 3. A fraction of ~ 80 per cent of SPIRE-350 sources have 1-3 optical counterparts, and ~ 20 per cent have 4-7 optical matches. A fraction of ~ 70 per cent of 500- μm objects have 1-3 optical counterparts, and ~ 30 per cent have 4-8 optical matches.

Thus, we have selected a sample of 2999 sources detected in 2 or more FIR bands (apart from the MIPS-24 detection) at the 4σ level (at least) in an area of 0.7 deg^2 . These sources are identified with 3925 optical objects satisfying the limiting magnitude criteria of Table 1, and the average number of optical counterparts for the FIR sources is ~ 1.3 . We note, however, that ~ 80 per cent of the MIPS-24 galaxies can be identified unambiguously with an

optical source. Since MIPS-70 and *Herschel* data present worse spatial resolutions, an uncertainty remains on the assignment of FIR fluxes to the correct (or most probable) UV/optical/NIR/MIR (and MIPS-24) counterpart. To cope with such uncertainty, it is compelling to assess how many of these 4σ -threshold FIR sources present a PACS detection. As mentioned above, ~ 80 per cent of the PACS sources exhibit a single MIPS-24 association and only one optical counterpart. There are 2536 sources detected in 2 or more FIR filters including a PACS channel, which are associated to 3245 optical objects.

4 SELECTION OF A SAMPLE OF DUSTY STARBURSTS AT $z \sim 1$

In this Section, we describe how we built a sample of *bona fide* dusty starburst galaxies when the span of the peak of the cosmic dusty SFR density ends ($z \sim 1$, Casey et al. 2012; Brisbin et al. 2017). To build such a sample, we need reliable (spectroscopic or photometric) redshifts, stellar masses, and *SFRs* for the IR emitters described in the previous Section. In order to have reliable *SFR* estimations for our galaxies, we considered a *main sample* composed by sources with a MIPS-24 detection and measured high-confidence fluxes in at least 2 more FIR bands ($\lambda_{\text{obs}} \geq 70 \mu\text{m}$) including a PACS detection, for which accurate total IR luminosities could be estimated. We added a *complementary sample* with sources only detected by MIPS at 24 μm (some also detected in 1 FIR filter) in order to maximize the completeness of our final sample, although admitting the lower reliability of their IR-based *SFR* estimations. Focusing on the main sample (see Section 4.2), and considering that the space density of ULIRGs decreases 2 orders of magnitude from $z \sim 2$ to $z \sim 0.6$ (Dudzevičiūtė et al. 2020), we decided to centre our analysis on the redshift range $0.7 \leq z \leq 1.2$.

In the following Sections, we describe how we estimated photometric redshifts, stellar masses, and *SFRs* for the IR sources presented in Section 3. Then, we select starburst galaxies, defined as those sources which are significantly and reliably above the MS of galaxies in the *SFR* vs. M_\star plane. Finally, we give statistical properties of our final sample of galaxies (adding up the main and complementary samples).

4.1 Estimations of photometric redshifts, stellar masses and *SFRs*

We estimated photometric redshifts (z_{phot}) using the EAZY code (Brammer et al. 2008), and the SEDs described in the previous Section for the parent sample formed by the 3925 MIPS-24 emitters which are covered by the IRAC, WFCAM, and Suprime-Cam surveys. In our SED analysis, we only considered fluxes measured at the $\geq 4\sigma$ level.

In order to calibrate our photometric redshifts, we used spectroscopic redshifts, which were available for about one third of the parent sample, virtually all (~ 90 per cent) at $z < 1.3$, and ~ 30 per cent at $0.7 \leq z \leq 1.2$, our range of interest. The photometric redshift accuracy was quantified using the normalized median absolute deviation of $\Delta z = z_{\text{phot}} - z_{\text{spec}}$ (σ_{NMAD} , Ilbert et al. 2006). The scatter of the whole spectroscopic sample is $\sigma_{\text{NMAD}} = 0.030$, and the median of the common used estimator results $|\Delta z|/(1 + z_{\text{spec}}) = 0.020$. Defining η as the fraction of outliers with $|\Delta z|/(1 + z_{\text{spec}}) > 0.2$, we get $\eta = 12$ per cent. For sources at $0.7 \leq z \leq 1.2$, the values are $\sigma_{\text{NMAD}}^z = 0.028$, and $\eta^z = 10$ per cent.

Our σ_{NMAD}^z value is similar to that ($\sigma_{\text{NMAD}}^B = 0.025$) estimated for each subsample of MIPS-24 emitters derived from WFC3-F160W-selected objects in the GOODS-S, UDS and EGS fields (Barro et al. 2019), but obtaining a higher η value (10 compared with 4 per cent). Our statistics for the reliability of photometric redshifts are also similar to those found by other authors focused in the analysis of FIR sources (see, e.g., Berta et al. 2011; Casey et al. 2012).

Using these photometric or spectroscopic (when available) redshifts, we estimated stellar masses and $SFRs$. Previous to such estimations, we excluded from our work all X-ray emitters (using the catalogue from Akiyama et al. 2015), which account for 4 per cent of the parent sample. Another 4 per cent of sources were identified as obscured active galactic nuclei (AGN) candidates without X-ray counterpart using the criteria in Donley et al. (2012). Thus, the total fraction of AGN candidates is ~ 8 per cent, which is similar with that obtained from other *Herschel*-based studies (e.g., a 7 per cent is found in Gruppioni et al. 2013).

Stellar masses were derived from UV, optical and NIR data by selecting the best-fitting template of a reference set constructed using one and two stellar populations (see Pérez-González et al. 2008).

Concerning total $SFRs$, we calculated $SFR_{\text{UV+IR}}$ for the parent sample of galaxies using the recipe found in Bell et al. (2005), which considers the unobscured UV luminosity jointly with UV photons absorbed by dust and re-emitted in the IR (see Kennicutt 1998). The equation providing $SFRs$ from UV and total IR luminosities—assuming a Salpeter (1955) initial mass function (IMF)—is:

$$SFR_{\text{UV+IR}} (M_{\odot} \text{ yr}^{-1}) = 1.8 \times 10^{-10} [3.3L(0.28) + L_{\text{TIR}}] / L_{\odot}, \quad (1)$$

where $L(0.28) = \nu L_{\nu}(0.28)$ is the monochromatic luminosity at $0.28 \mu\text{m}$ rest frame, obtained by interpolating in the best-fitting stellar population model used for the M_{\star} estimation.

The total IR luminosities, L_{TIR} , are derived from *Spitzer* and *Herschel* data by computing the median value of the luminosities provided by the best-fitting templates extracted from the libraries of dust emission models given in Chary & Elbaz (2001), Dale & Helou (2002), and Rieke et al. (2009) (hereafter CE01, DH02, and R+09). When several IR fluxes are available (MIPS-24 plus other PACS and/or SPIRE bands), all libraries provide similar results, with differences lower than 0.15 dex and a typical rms scatter around 0.05 dex. When only the $24\text{-}\mu\text{m}$ measurement is available, the estimations are more uncertain, since a large extrapolation is needed to translate from a single monochromatic luminosity in the rest-frame MIR to the L_{TIR} which is dominated by the dust-peak emission, typically located at 50 to $200 \mu\text{m}$. In order to account for this issue, we used the method described in Rujopakarn et al. (2013), especially designed to cope with the lack of FIR data for MIPS-24 emitters, to get total IR luminosities for MIPS-only sources, L_{TIR}^{R+13} . We compared the L_{TIR}^{R+13} values with L_{TIR} estimations for *Herschel* sources. This comparison showed a ~ 0.2 -dex scatter between both estimates. Using the L_{TIR}^{R+13} and the 3 IR model libraries, we computed the expected fluxes for the undetected FIR bands. We only kept in our sample those galaxies whose synthetic fluxes are compatible with a non-detection in the FIR channels (compared to 5σ -detection thresholds). For complementary sources, we assigned the 0.2-dex scatter as uncertainty for each FIR synthetic flux.

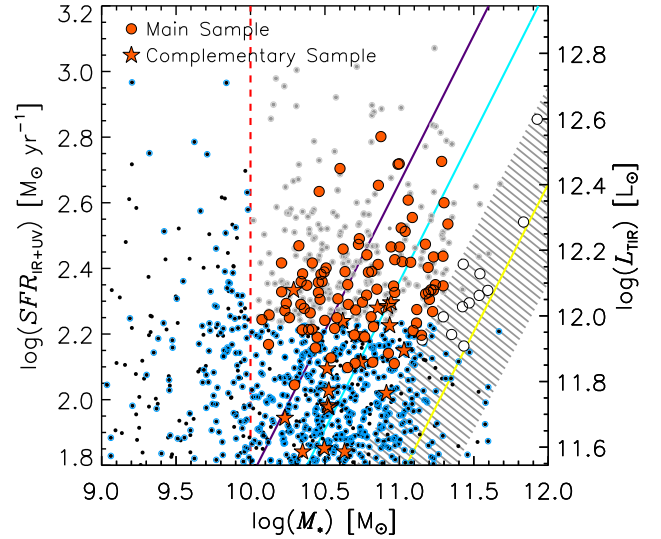


Figure 1. Stellar mass, M_{\star} , vs. total SFR , $SFR_{\text{IR+UV}}$, plot for the galaxies in our sample with $24\text{-}\mu\text{m}$ counterpart (filled black circles) and with PACS association (open blue circles) at $0.7 \leq z \leq 1.2$. We display the relation for the main sequence at $z \sim 1$ of Elbaz et al. (2007, solid yellow line) with its 68% confidence level (hashed grey area). The filled grey circles depict values for the 237 dSFGs satisfying the L_{TIR} and M_{\star} criteria. The dashed red line marks the M_{\star} lower limit. The filled orange circles show values for the IR-bright starburst of the main sample (with $SFR_{\text{IR+UV}}$ above the $MS+1\sigma$ scatter). The filled orange stars show values for dusty starbursts in the complementary sample. The open black circles show IR-bright objects inside the $MS \pm 1\sigma$ area, which are excluded from this study. The solid cyan and solid purple line depict the aforementioned MS plus 2σ and 3σ scatter, respectively.

4.2 Selection of dusty massive starburst galaxies and construction of the final sample

From now on, we restrict our work to galaxies in the redshift range $0.7 \leq z \leq 1.2$. The choice of the redshift limits is based on 2 points: (1) We are interested in studying IR-bright starbursts when the span of the peak of the cosmic dusty SFR density ends. We define such starbursts as dSFGs whose position in the SFR vs. M_{\star} plane is at least 1σ above the MS (see below). (2) We want to maximize the number of sources in our sample, especially those for which accurate total IR luminosities can be obtained (so we are certain about their dusty starburst nature), which implies detections in several FIR bands. We are also interested in assessing the duration of the starburst phase of powerful sources in the galaxy evolution scheme, so we cut the sample at $L_{\text{TIR}} \gtrsim 10^{12} L_{\odot}$. We note that PACS detections account for 91, 81, and 54 per cent at $0.7 \leq z < 1.0$, $1.0 \leq z < 1.2$, and $1.2 \leq z < 1.3$. Thus, we imposed $z = 1.2$ as our upper limit in redshift, ensuring that most of our dSFGs present a PACS detection. The L_{TIR} cut roughly translates to $\log(M_{\star}/M_{\odot}) > 10$ at $z \sim 1$ (see discussion below). We note that galaxies at $z \geq 1$ with masses $\log(M_{\star}/M_{\odot}) < 10$ are scarcely detected in the PACS data of the SXDS/UDS field (see Fig. 1). Thus, we impose this mass as lower limit for our selection. Concerning the lower redshift limit, it is basically ruled by the low space density of ULIRGs at $z \sim 0.6$.

We visually checked the MIPS, IRAC, Suprime-Cam, WFCAM, PACS and SPIRE images of the 237 dSFGs satisfying the aforementioned redshift, L_{TIR} and stellar-mass criteria, which conform our starburst candidates. As mentioned in Section 3.2, the

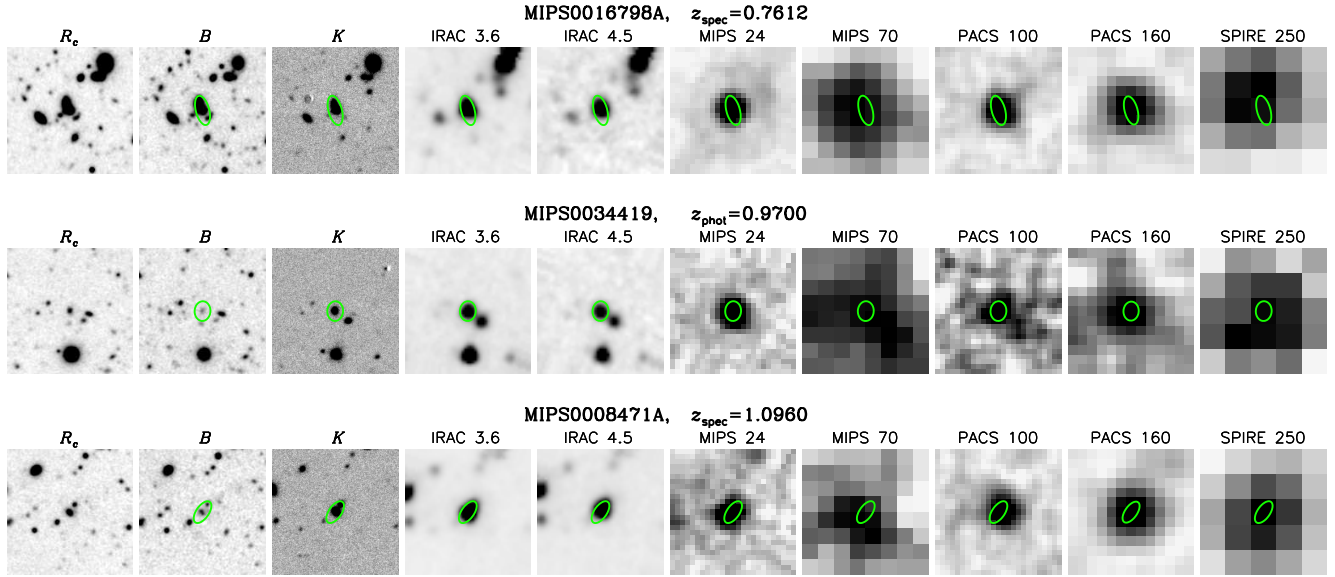


Figure 2. Thumbnails of 3 dusty starburst galaxies from our main sample ordered by increasing redshift. From left to right, we show 30 per 30 arcsec postage stamps in the *Subaru*/Suprime-Cam R_c and B , and *UKIRT*/WFCAM K bands, *Spitzer*/IRAC 3.6 and 4.5 μm and MIPS channels, and *Herschel*/PACS and SPIRE 250 μm bands. The green ellipse shows the aperture best enclosing each one of the optical/NIR identifications with the less possible contamination from other objects. The first and third row show examples of sources where several debledged counterparts in the optical were merged based on their proximity and similar redshift. In the upper part of each thumbnail we present the ID of the source, and the photometric or spectroscopic redshift. The thumbnails of the rest of the main sample and the complementary sample can be found as online material.

MIPS-24 detections connect the wide-beam FIR channels with the higher-resolution UV/optical/NIR bands. Thus, we used the 24- μm detections to constrain the identification at other wavelengths (to the red and the blue). During this visual inspection process, we removed SPIRE fluxes from the SEDs when we noticed significant emission from near MIPS-24 neighbour(s) of the main 24- μm counterpart. The presence of such bright MIPS-24 neighbours can produce unphysical jumps in the FIR SED (see ‘clean index’, [Elbaz et al. 2011](#)). A fraction of 24 per cent of the 237 dSFGs have MIPS-24 neighbours causing unreliable photometry in the FIR bands. Given the ~ 6 arcsec angular resolution of MIPS-24, blending of several optical sources within a MIPS-24 resolution element is possible. Then, an unambiguous optical counterpart cannot always be ascertained. Hence, we examined whether the position of the optical source was centred at the location of its MIPS-24 counterpart, and if there was any close optical neighbour possibly emitting at 24 μm . If such neighbour was at similar z_{spec} or z_{phot} (implying that they are probably interacting), we merged the sources into the same object, adding up the fluxes in each band and repeating the z_{phot} and M_\star estimations (see, e.g., [Cibinel et al. 2019](#)). Another 14 per cent of the dSFGs presented near optical companions (at different z_{spec} or z_{phot}) indicating not being the most probable counterpart. In particular, around one fifth and one twelfth of the 147 trustworthy IR-bright dSFGs could be identified with 2 and 3 optical counterparts of very similar redshift.

After this sample purging, we repeated the L_{TIR} estimations by fitting the reliable observed fluxes at wavelengths ≥ 70 μm to the IR libraries of CE01, DH02, and R+09. We assumed the best-fitting result as $L_{\text{TIR}}^{\text{ref}}$. We did not use the MIPS-24 flux to avoid PAH absorptions and emissions (probed by 24- μm band in the redshift range $0.7 \leq z \leq 1.2$) to affect the fits, and thus obtaining a better characterization of the FIR SED peak, which dominates the L_{TIR} estimations. In any case, we verified that similar L_{TIR} results (with differences < 0.1 dex) are derived when including the 24- μm flux

in the fit. The $L_{\text{TIR}}^{\text{ref}}$ uncertainties (hereafter $\sigma_{L_{\text{TIR}}}$) are calculated by adding in quadrature the dispersion between the L_{TIR} estimates (for $\lambda_{\text{obs}} \geq 70 \mu\text{m}$) of the 3 IR libraries, and a constant value of 0.022 dex (equivalent to 5% of the galaxy L_{TIR}). This constant value is used to consider uncertainties in the absolute calibration and the confusion noise of the MIPS, PACS and SPIRE instruments.

In order to select dusty starburst galaxies at intermediate redshift, we built a SFR vs. stellar mass plot for the dSFGs drawn from the parent sample and lying at $0.7 \leq z \lesssim 1.2$, distinguishing the 105 reliable IR-bright dSFGs resulting with $\log(L_{\text{TIR}}/L_\odot) \gtrsim 11.8$ and $\log(M_\star/M_\odot) \geq 10$. This is shown in Fig. 1. Most of these IR-bright galaxies are located well above the so-called $z \sim 1$ MS of the $SFR - M_\star$ relation (see, e.g., [Elbaz et al. 2007](#); [Schreiber et al. 2015](#)).

Based on Fig. 1, we selected 93 dusty starburst galaxies – detected by MIPS and *Herschel* – which lie above the MS at least at the 1σ level. This is what we call the main sample of dusty starbursts. We added to our work 18 starburst galaxies detected by MIPS at 24 μm (some also detected in 1 FIR filter), constituting the complementary sample. In total, our final sample is composed by 111 sources. Postage stamps of some of the galaxies in our final sample can be found in Fig. 2.

4.3 Closing remarks of the sample

Our final sample of massive dusty starbursts lies at $0.7 \leq z \lesssim 1.2$, it consists of 111 galaxies, 93 in the main sample, and 18 in the complementary sample. There are 13 (~ 12 per cent) galaxies with spectroscopic redshifts, and the normalized median absolute deviation estimated using only these values is $\sigma_{\text{NMAD}} = 0.012$. Our massive dusty starbursts are detected in at least 10 optical to NIR, MIPS-24, and (only for the main sample) 2+ FIR bands. They have median, and 16 and 84-percentile values of $M_\star = 5.3^{+7.7}_{-3.0} \times 10^{10} M_\odot$, $z = 1.09^{+0.06}_{-0.21}$, and $L_{\text{TIR}}^{\text{ref}} = 1.11^{+0.48}_{-0.38} \times 10^{12} L_\odot$.

Table 2. Dusty-starburst main-sample multi-band photometry. (1) Name of the galaxy. (2,3) Right ascension and declination (J2000) in degrees. (4) Photometric or spectroscopic redshift (z_{spec} indicated by a †). (33-39) Flux densities in MIPS 24, 70; PACS 100, 160; SPIRE 250, 350, 500 in mJy. (5-11,19-25) Observed magnitude in FUV, NUV; B , V , R_c , i' , z' ; J , H , K ; IRAC 3.6-8.0 in the AB photometric system. (40-46) Associated uncertainties to MIPS 24, 70; PACS 100, 160; SPIRE 250, 350, 500 in mJy determined as described in Sections 2.1 and 2.2. (12-18,26-32) Associated uncertainties to FUV, NUV; B , V , R_c , i' , z' ; J , H , K ; IRAC 3.6-8.0 as obtained from the aperture matched cataloguing (see Section 3.2). “...” indicate bands without detections or without reliable photometric measurements.

(This Table and that for the complementary sample are available in its entirety in the online journal.)

Galaxy	α	δ	z^\dagger	FUV Δ FUV J ΔJ S_{24} ΔS_{24}	NUV Δ NUV H ΔH S_{70} ΔS_{70}	B ΔB K ΔK S_{100} ΔS_{100}	V ΔV $[3.6]$ $\Delta[3.6]$ S_{160} ΔS_{160}	R_c ΔR_c $[4.5]$ $\Delta[4.5]$ S_{250} ΔS_{250}	i' $\Delta i'$ $[5.8]$ $\Delta[5.8]$ S_{350} ΔS_{350}	z' $\Delta z'$ $[8.0]$ $\Delta[8.0]$ S_{500} ΔS_{500}
(1)	(2)	(3)	(4)	(5)	(6)	(7)	(8)	(9)	(10)	(11)
				(12)	(13)	(14)	(15)	(16)	(17)	(18)
				(19)	(20)	(21)	(22)	(23)	(24)	(25)
				(26)	(27)	(28)	(29)	(30)	(31)	(32)
				(33)	(34)	(35)	(36)	(37)	(38)	(39)
				(40)	(41)	(42)	(43)	(44)	(45)	(46)
MIPS0000648A	34.586462	-5.201155	1.1900	24.48	24.19	23.70	23.13	22.33
				0.02	0.02	0.01	0.01	0.01
				21.80	21.35	20.71	20.08	20.05	20.26	20.21
				0.02	0.02	0.01	0.04	0.04	0.05	0.06
				0.20	...	8.67	23.02	26.21	16.33	...
				0.02	...	0.69	1.84	2.41	3.33	...
MIPS0000826	34.894621	-5.300254	0.7200	24.21	23.29	22.33	21.62	21.28
				0.02	0.01	0.01	0.01	0.01
				20.71	20.24	19.70	19.30	19.62	19.38	18.86
				0.01	0.02	0.01	0.04	0.04	0.04	0.05
				2.09	66.27	90.70	105.05	65.59
				0.04	2.92	7.08	8.40	4.39
MIPS0002196_1	34.474978	-5.038923	1.0980†	26.05	25.37	24.65	23.66	22.84
				0.05	0.04	0.03	0.02	0.01
				21.95	21.35	20.58	19.85	19.87	20.12	19.64
				0.02	0.02	0.01	0.03	0.03	0.04	0.06
				0.67	...	15.20	26.28	28.00	18.68	...
				0.02	...	1.25	2.26	2.60	3.53	...

The multi-band photometry catalogue, used in the rest of the paper, for our final sample of IR-bright starburst galaxies in SXDS/UDS field is presented in Table 2.

In the next Section, we describe our method to study the stellar population properties of our final sample of massive dusty starburst galaxies at the peak span end of the cosmic dusty SFR density. Our results are presented and compared with the literature in Sections 6 and 7.

5 SELF-CONSISTENT SED MODELLING

In order to derive stellar population properties of $0.7 \leq z \lesssim 1.2$ starburst ($\geq 1\sigma$ above the $z = 1$ MS) galaxies, their UV-to-FIR rest-frame SEDs are modelled in a self-consistent way, accounting for their dust content and the attenuation of the stellar light produced by that dust. In our analysis we use the CIGALE (Noll et al. 2009) and SYNTHESIZER (Pérez-González et al. 2003, 2008) codes, which

cope with the auto-consistent modelling of the stellar emission, and dust attenuation and re-emission using energy balance techniques.

Studying the stellar population properties of dSFGs, *Spitzer* observations have shown that SMGs house old stellar populations in place at $z \sim 2$ (Borys et al. 2005). In addition, submillimetre data have evinced that these old populations are accompanied of dust-enshrouded young stellar populations in an ongoing burst (Dye et al. 2008). Dunlop (2011) has shown that nothing more complex than a SFH depicted by an old and a young population is necessary to fit the observed SEDs of SMGs. Buat et al. (2014) indicate that two stellar population (2P) models are the best fits for the observed UV-to-FIR SEDs of PACS-detected galaxies at $1 < z < 3$. The young population accounts for most of the UV emission, and the old population might significantly contribute or even dominate the optical/NIR emission. Such 2P SFHs have been used in many papers focusing on the study of star-forming galaxies, whose nature is not easily explained with more classical and simple SFHs such as decaying exponential or even delayed forms (Gawiser et al. 2007; Lee et al. 2009;

Table 3. Input parameters of the CIGALE and their explored range.

Parameter	Symbol	Range
Metallicity	Z	$Z_{\odot} = 0.02$
e -folding times of the old stellar population in Gyr	τ_{old}	0.1, 1, 3, 10
Ages of the old stellar population in Gyr	t_{old}	3, 5, 7 for $0.7 < z \leq 0.8$ 2, 4, 6 for $0.8 < z \leq 1.0$ 1, 3, 5 for $1.0 < z \lesssim 1.2$
e -folding time of the young stellar population in Gyr	τ_{you}	20
Ages of the young stellar population in Myr	t_{you}	1, 10, 25, 50, 75, 100, 200, 300, 400, 500, 600, 700, 800, 900, 1000
Mass fraction of young population or burst intensity	b_{you}	0, 0.001, 0.005, 0.01, 0.05, 0.06, 0.07, 0.08 0.09, 0.1, 0.2, 0.3, 0.4, 0.5, 0.6, 0.7
V-band attenuation for the young population in mag	$A_{V,\text{you}}$	0.15, 0.30, 0.45, 0.6, 0.75, 0.9, 1.05, 1.2, 1.35, 1.5, 1.65, 1.8, 1.95, 2.1, 2.25, 2.4, 2.55, 2.7, 2.85, 3.0, 3.15, 3.3, 3.45, 3.6, 3.75, 3.9, 4.05, 4.2
Reduction factor of $A_{V,\text{you}}$ for $A_{V,\text{old}}$	f_{att}	0, 0.25, 0.5, 0.75, 1

Table 4. Input parameters of the SYNTHESIZER code and their explored range

Parameter	Symbol	Range
Metallicity	Z	$Z_{\odot} = 0.02$
e -folding times of the old stellar population in Gyr	τ_{old}	from 0.1 to 10 in logarithmic intervals of 0.5 dex
Ages of the old stellar population in Gyr	t_{old}	3, 4, 5, 6, 7 for $0.7 < z \leq 0.8$ 2, 3, 4, 5, 6 for $0.8 < z \leq 1.0$ 1, 1.5, 2, 3, 4, 5 for $1.0 < z \lesssim 1.2$
V-band attenuation for the old population in mag	$A_{V,\text{old}}$	from 0 to 1.5 in increments of 0.1
e -folding time of the young stellar population in Gyr	τ_{you}	16, 20
Ages of the young stellar population in Myr	t_{you}	1, 1.5, 2, 2.5, 3, 3.5, 4, 4.5, 5, 5.5, 6, 6.5, 7, 7.5, 8, 8.5, 9, 9.5, 10, 15, 20, 25, 30, 35, 40, 45, 50, 55, 60, 65, 70, 75, 80, 85, 90, 95, 100, 200, 300, 400, 500, 600, 700, 800, 900, 1000
Mass fraction of young population or burst intensity	b_{you}	from 0.1 to 0.7 in increments of 0.05
V-band attenuation for the young population in mag	$A_{V,\text{you}}$	from 0 to 4.2 in increments of 0.1

Casey et al. 2014; De Geyter et al. 2015; Ciesla et al. 2017). More importantly for our work, 2P models have been proved to recover accurately the stellar masses of simulated SMGs (Michałowski et al. 2014), and the photometric masses derived with these 2P models agree well with the dynamical masses of local starburst galaxies (Bergvall et al. 2016).

In our work, the two populations are represented by a recent burst with roughly constant SFH overlapped to and old population with decreasing SFH. In both cases, the star formation events are implemented with decaying exponentials. Both populations are linked with the so-called burst intensity, defined in terms of stellar masses for the young stars and the entire galaxy ($b_{\text{you}} = M_{\star,\text{you}}/M_{\star}$). The SFHs are parametrized with τ_{old} , t_{old} , τ_{you} , and t_{you} , which stand for the decay factors and ages for the old and young populations.

Both bursts are recreated using single stellar populations of Maraston (2005) models, which treat minutely the thermally pulsating asymptotic giant branch stars emission, necessary for the

determination of rest-frame NIR colors and luminosities of stellar populations with ages $\sim 0.1 - 1$ Gyr (Tonini et al. 2009; Lacey et al. 2016). However, the contribution of these stars to the NIR luminosity is still debated (Zibetti et al. 2013). We assume a Salpeter (1955) IMF.

Solar metallicity, Z_{\odot} , is adopted for both populations, considering that is unfeasible to break the age-metallicity degeneracy with broadband data (O’Connell 1986), and that $z \gtrsim 1$ dSFGs typically present metallicities near this value (Swinbank et al. 2004; Wardlow et al. 2017; Boogaard et al. 2019) for the masses we probe in our work. The effects of dust on the UV-optical light coming from both populations are considered using the Calzetti et al. (2000, hereafter C+00) attenuation law, derived for nearby starburst galaxies. Salmon et al. (2016) studied a galaxy sample at $z \sim 1.5 - 3$ from the CANDELS survey with MIPS-24 detections, using different assumptions about the attenuation law. They found that highly at-

tenuated stellar populations have a starburst-like law. Therefore, we consider the assumption of the C+00 law adequate.

In our study, the amount of attenuation in the V band of both populations is constrained balancing the absorbed energy with the luminosity re-emitted by dust at IR wavelengths (the L_{TIR}). This is what we call the FIR prior, and it represents the main characteristic of our auto-consistent approach. For CIGALE, the attenuation in V of the young population (A_V^{you}) is estimated first, then a reduction factor relative to this A_V^{you} is applied to get the attenuation for the old stars, $A_V^{\text{old}} = A_V^{\text{you}} f_{\text{att}}$. For the SYNTHESIZER code A_V^{you} and A_V^{old} are estimated independently.

The CIGALE code estimates L_{TIR} using the DH02 templates (the default library in CIGALE FORTRAN 2013/11/18), which are linked to the attenuated SPS models. The full UV-to-FIR set of models are compared with the observed galaxy photometry using a χ^2 minimization. All available data points with $\lambda_{\text{obs}} < 550 \mu\text{m}$ are included in our fits, except MIPS-24 data (see Section 4.2). The full set of values of the input parameters are listed in Table 3. Following Giovannoli et al. (2011), we fixed $\tau_{\text{you}} = 20$ Gyr to consider constant SFHs for the young population. CIGALE uses a Bayesian-like analysis to derive galaxy properties. The input parameters, and values as M_\star , and SFR are derived from their probability distribution function. The expected value and the standard deviation for each parameter are determined as detailed in the ‘sum’ method of Noll et al. (2009).

In the SYNTHESIZER code, the dust-absorbed UV-optical stellar energy of the models is constrained according to the MIR-FIR energy re-radiated by dust, our $L_{\text{TIR}}^{\text{ref}}$, i.e., using the FIR prior. We included in the stellar population fits all available data points for $\lambda_{\text{obs}} \leq 4.5 \mu\text{m}$ because the integrated emission in this range should be dominated by stars for the galaxies in our sample. Uncertainties in the derived parameters and degeneracies in the solutions are analysed using a Monte-Carlo algorithm, varying randomly each observed flux within a Gaussian distribution of width equal to its corresponding photometric error, and repeating the fit with all the feasible models 3000 times. Then, clusters of solutions are identified using a k -means method (Pérez-González et al. 2013), assigning a statistical significance to each cluster, defined as the fraction of the 3000 solutions, which belonged to it. So we grouped solutions providing similar results and calculated the median value and the scatter of each group in the multi-dimensional space formed by the fitted parameters. We considered the most significant cluster as the best solution.

The input parameters assumed for the SYNTHESIZER code are listed in Table 4. The SYNTHESIZER parameters and fitting procedure are similar to those used by CIGALE.

6 IMPORTANCE OF THE FIR PRIOR IN THE CHARACTERIZATION OF THE STELLAR POPULATIONS

In this Section, we evaluate the utility of using the FIR prior in the SED fitting. For that purpose, we compare the solutions obtained with 2P models including and excluding the FIR constraint. Both sets of solutions are derived with the SYNTHESIZER and CIGALE codes (see Section 5). With this exercise, we are able to test the value of employing the FIR prior to constrain the attenuation of the stellar emission, and to quantify the impact of this constraint in the estimation of stellar parameters of dusty starbursts. It is important to mention that the trustworthiness and accuracy of the resulting stellar properties will depend on the photometric uncertainties and

the degeneracies (e.g., age-dust, age-burst strength) between such properties.

Considering that a starburst galaxy is defined by means of its stellar mass and SFR , we compare first the values derived for these properties and then the results for attenuation and age for each modelling case and code.

6.1 Effect of the FIR prior in the determination of stellar masses

The CIGALE and SYNTHESIZER codes supply mass-to-light ratios for all photometric bands used in the fits, which can be compared to the measured fluxes and provide stellar mass estimates (weighted with flux errors).

For the SYNTHESIZER code, the stellar masses estimated using the FIR prior for the entire sample are in the range $5.8 \times 10^9 < M_{\star}^{\text{SYN,FIR}}/M_{\odot} < 1.5 \times 10^{11}$ with a median of $3.8^{+3.4}_{-2.2} \times 10^{10} M_{\odot}$, and a median uncertainty of 0.07 dex. The stellar masses obtained without the FIR data range between $6.0 \times 10^9 < M_{\star}^{\text{SYN,noFIR}}/M_{\odot} < 1.6 \times 10^{11}$, with a median of $3.4^{+2.4}_{-1.3} \times 10^{10} M_{\odot}$, and a median error of 0.06 dex. The median difference between the stellar masses estimated with FIR models, and those derived with the non-FIR ones is 10 per cent. The stellar mass ratios range between $0.2 \leq M_{\star}^{\text{SYN,noFIR}}/M_{\star}^{\text{SYN,FIR}} < 5.7$, with a fraction of ~ 14 per cent of all objects showing mass differences greater than a factor of 2. We find that the mass ratio increases as the difference in the attenuations for the old population, $A_{V,\text{old}}^{\text{SYN,noFIR}} - A_{V,\text{old}}^{\text{SYN,FIR}}$, rises. This suggests that including the FIR data in the fitting can help to diminish the uncertainty in the old-population attenuation, $A_{V,\text{old}}^{\text{FIR}}$, which improves the determination of stellar masses of dusty starbursts (see, e.g., da Cunha et al. 2015).

For CIGALE and the whole sample, the stellar masses obtained using the FIR prior are in the range $7.9 \times 10^9 < M_{\star}^{\text{CIG,FIR}}/M_{\odot} < 2.2 \times 10^{11}$, with a median of $5.2^{+4.8}_{-3.2} \times 10^{10} M_{\odot}$, and a median uncertainty of 0.14 dex. The stellar masses estimated without the FIR data range between $8.9 \times 10^9 < M_{\star}^{\text{CIG,noFIR}}/M_{\odot} < 1.9 \times 10^{11}$, with a median of $4.0^{+4.7}_{-2.3} \times 10^{10} M_{\odot}$, and a median error of 0.22 dex. On median, the stellar masses determined with FIR models are 15 per cent larger than those derived with non-FIR models, which is consistent with what was found for SYNTHESIZER. The stellar mass ratio values range in $0.2 \leq M_{\star}^{\text{CIG,noFIR}}/M_{\star}^{\text{CIG,FIR}} < 1.7$, with a fraction of ~ 6 per cent of all galaxies showing mass differences greater than a factor of 2. We find that the mass ratio decreases as the difference in the burst intensity, $b_{\text{you}}^{\text{CIG,noFIR}} - b_{\text{you}}^{\text{CIG,FIR}}$, increases. This indicates that using the FIR prior aids to reduce the uncertainty in the determination of the parameters of the young stellar population (via better constraining the SFR and $t_{\text{you}}^{\text{FIR}}$, see Sections 6.2 and 6.3), which influences the stellar mass estimations.

It is noteworthy that both codes behave in the same way, providing larger stellar masses on median when using the FIR prior.

Summarising the results obtained with both codes, although there is not a significant difference between the stellar mass values derived with and without using the FIR prior, the FIR data seem to help to reduce the uncertainty in the determination of the parameters of the old and young stellar populations. This hypothesis will be tested in the following Subsections.

6.2 Effect of the FIR prior in the determination of SFR s

We compare now the SFR s derived with the 2P models estimated by SYNTHESIZER and CIGALE (with and without the FIR prior) with

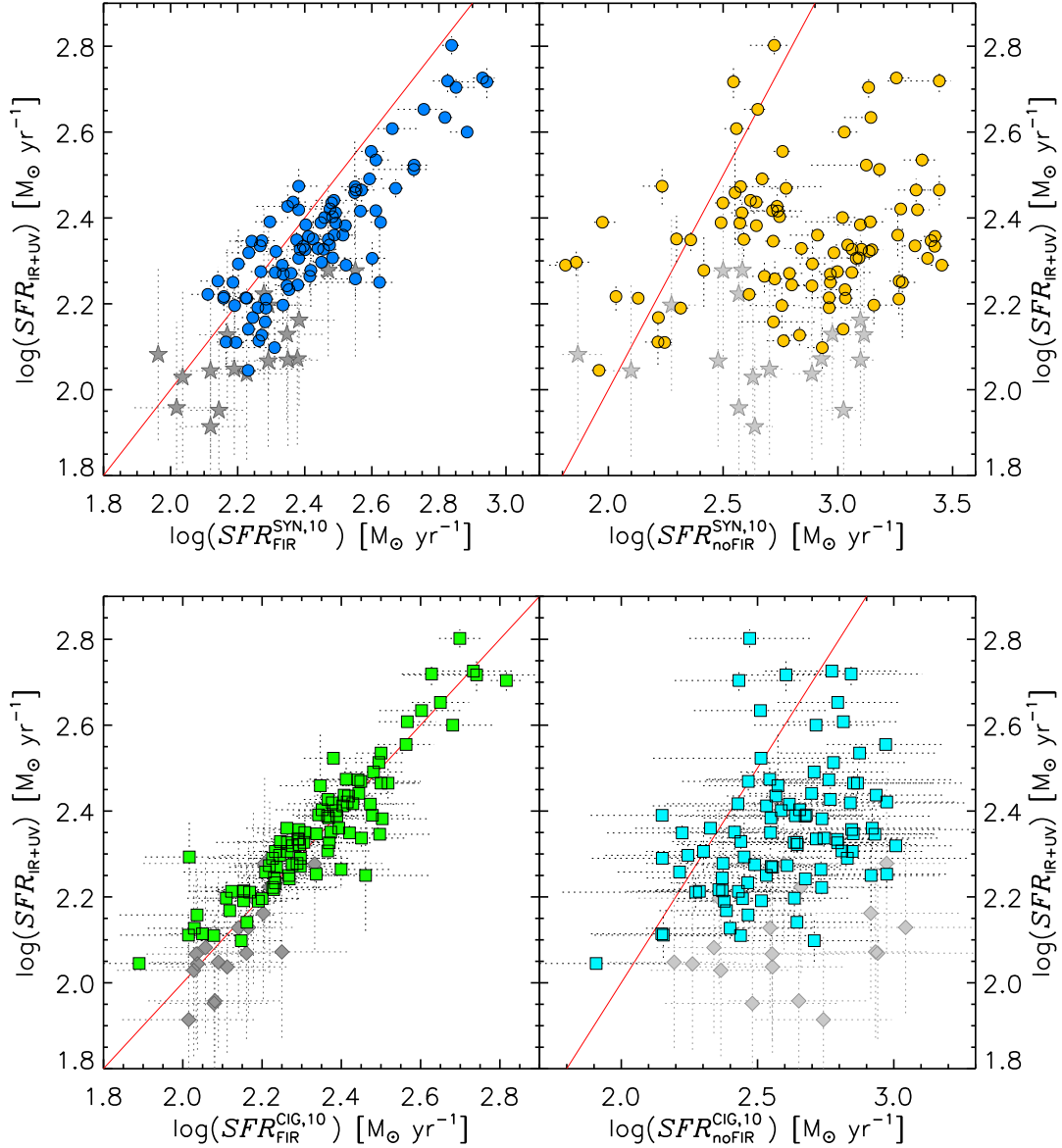


Figure 3. Comparison between the SFR s determined with the observed FIR and UV and those derived with 2P models (averaged over the last 10 Myr) with (left) and without (right) the FIR prior from the SYNTHESIZER (top) and CIGALE (bottom) codes. The filled circles (filled stars) with error bars show the median values and the 1σ uncertainties for the main (complementary) sample derived from the logarithmic space with the SYNTHESIZER code. The filled squares (filled diamonds) stand for the expected values and standard deviations determined with the CIGALE. The solid lines show the one-to-one relation.

SFR s based on observables, namely the FIR and UV emission (SFR_{UV+IR}). In order to do a fair comparison between SFR_{UV+IR} and SED-derived SFR values, we should consider that Kennicutt (1998) assumed a constant SFH with bursts lasting 10 – 100 Myr. Hence, our SED-derived SFR values are averaged over the last 10 Myr to put both SFR estimates in a similar time-scale. The comparison of SFR s is plotted in Fig. 3.

We estimated the contribution of the unobscured-UV luminosity to SFR_{UV+IR} for our whole sample and it is less than 5 per cent on average. Considering this minimal contribution, the main source of uncertainty in the SFR_{UV+IR} values is due to our L_{TIR}^{ref} estimations, whose rms error is lower than 0.13 dex for the main sample, and 0.2 dex for the complementary one. For the full sample, the SFR_{UV+IR} values range in $82 < SFR_{UV+IR} < 635 \text{ M}_\odot \text{ yr}^{-1}$, with median of $203^{+89}_{-69} \text{ M}_\odot \text{ yr}^{-1}$.

For our whole sample, the SYNTHESIZER 10-Myr-averaged SFR s derived using the FIR data range in $91 < SFR_{FIR}^{SYN,10} < 878 \text{ M}_\odot \text{ yr}^{-1}$, with median of $241^{+155}_{-74} \text{ M}_\odot \text{ yr}^{-1}$, and median uncertainty of ~ 11 per cent. The left panels of Fig. 3 show that the FIR prior succeeds to make the SED-based SFR s more similar to the observed SFR s, although we detect an offset, which we attribute to the distinct assumptions about the SFH and typical age of the recent burst. The median difference between the $SFR_{FIR}^{SYN,10}$ and SFR_{UV+IR} results is ~ 25 per cent. When no FIR prior is used, the comparison of SFR s is basically a scatter plot.

The SYNTHESIZER 10-Myr-averaged SFR s estimated without the FIR prior range in $65 < SFR_{noFIR}^{SYN,10} < 2838 \text{ M}_\odot \text{ yr}^{-1}$, with median of $681^{+836}_{-380} \text{ M}_\odot \text{ yr}^{-1}$, and a median error of 12 per cent. For 60 per cent of all galaxies, the SFR s derived without the FIR prior

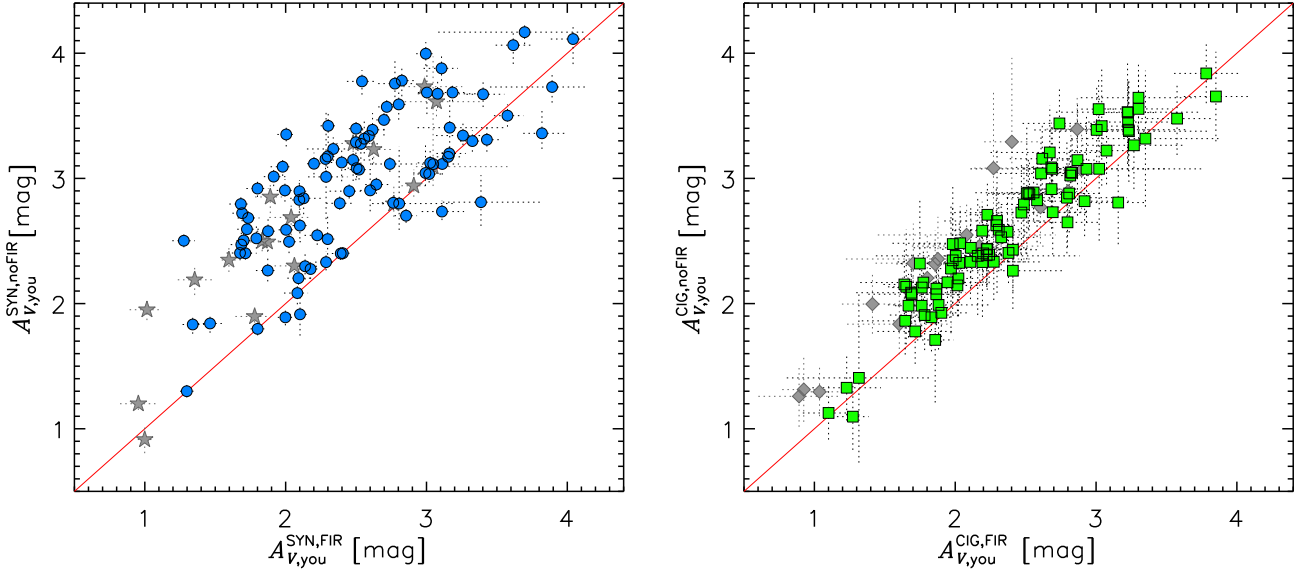


Figure 4. Comparison between the attenuations of the young population using the FIR prior on x-axis, and those derived without the FIR constraint on y-axis, estimated with the SYNTHESIZER (*left panel*) and the CIGALE (*right panel*) codes. The filled circles (filled stars) with error bars show the median values and 1σ uncertainties for the main (complementary) sample estimated with the SYNTHESIZER code. The filled squares (filled diamonds) with error bars stand for the expected values and standard deviations derived with the CIGALE.

are 0.3 dex larger than those estimated using the UV+FIR data. The median difference between the models without the FIR prior and our fiducial models, $\log(SFR_{\text{noFIR}}^{\text{SYN},10}) - \log(SFR_{\text{FIR}}^{\text{SYN},10})$, is 0.48 dex (a factor ~ 3), but differences for individual objects can reach values larger than 1 dex.

For the whole sample, the CIGALE 10-Myr-averaged $SFRs$ derived using the FIR prior range in $77 < SFR_{\text{FIR}}^{\text{CIG},10} < 656 \text{ M}_{\odot}\text{yr}^{-1}$, with median of $196^{+105}_{-65} \text{ M}_{\odot}\text{yr}^{-1}$, and a median uncertainty of ~ 26 per cent. In the lower panels of Fig. 3, it is evident that the $SFR_{\text{FIR}}^{\text{CIG},10}$ values are in better agreement with $SFR_{\text{UV+IR}}$ results than the $SFR_{\text{noFIR}}^{\text{CIG},10}$ values. The median difference between the $SFR_{\text{FIR}}^{\text{CIG},10}$ and $SFR_{\text{UV+IR}}$ results is ~ 3 per cent. The CIGALE 10-Myr-averaged $SFRs$ derived without the FIR constraint range in $80 < SFR_{\text{noFIR}}^{\text{CIG},10} < 1106 \text{ M}_{\odot}\text{yr}^{-1}$, with median of $402^{+302}_{-170} \text{ M}_{\odot}\text{yr}^{-1}$, and a median error of ~ 60 per cent. The median difference between models without the FIR prior and models using the FIR data, $\log(SFR_{\text{noFIR}}^{\text{CIG},10}) - \log(SFR_{\text{FIR}}^{\text{CIG},10})$ is 0.28 dex, which is similar to the median $SFR_{\text{noFIR}}^{\text{CIG},10}$ errors.

Summarising, $SFRs$ estimated with observables only match SED-based $SFRs$ for 2P models when using the FIR constraint. Both types of calculations agree reasonably well for the 2 codes used in our work, although SYNTHESIZER provides slightly larger values than the UV+FIR data. We find that the SYNTHESIZER $SFRs$ become larger than the ones based on UV+FIR data as the young-population age decreases. The galaxies where the $SFR_{\text{UV+IR}} > SFR_{\text{FIR}}^{\text{SYN},10}$ are the ones with the largest young-population ages ($\gtrsim 300$ Myr), for which the Kennicutt (1998) conversion is less accurate. Thus, the explanation is tracked down in the more complex SFHs considered by SYNTHESIZER compared to the assumptions in Kennicutt (1998), as explained in the next Subsection.

Considering that we are studying dusty starburst galaxies, we can refer to SFR and L_{TIR} in an interchangeable way. Then, the

scatter plots shown in the right panels of Fig. 3 clearly evince that 2P models without the FIR information fail to reproduce the dust emission. A similar conclusion has been found by Hunt et al. (2019) studying a nearby galaxy sample using codes managing energy-balance techniques.

6.3 Effect of the FIR prior in the determination of the properties of the young population

Here we compare the young-population parameters derived with the CIGALE and SYNTHESIZER codes for each 2P case, to study what causes the difference between the SED-derived SFR values of both 2P models.

In Figure 4, we compare the attenuations of the young stellar population in our sample of dusty starbursts for the 2 types of models and codes. The SYNTHESIZER young attenuations derived using the FIR prior range in $0.9 < A_{V,\text{you}}^{\text{SYN},\text{FIR}} < 4.1$ mag, with median of $2.4^{+0.7}_{-0.6}$ mag, and a median uncertainty of 0.1 mag. The results computed without the FIR data are in the range $0.9 < A_{V,\text{you}}^{\text{SYN},\text{noFIR}} < 4.2$ mag, with median of $2.9^{+0.6}_{-0.6}$ mag, and a median error of 0.1 mag. The median difference of $(A_{V,\text{you}}^{\text{SYN},\text{noFIR}} - A_{V,\text{you}}^{\text{SYN},\text{FIR}})$ is 0.6 mag, but individual objects can reach differences of 1.3 mag.

The CIGALE results are very similar to the SYNTHESIZER ones. The values determined with the FIR constraint range in $0.8 < A_{V,\text{you}}^{\text{CIG},\text{FIR}} < 3.9$ mag, with median of $2.3^{+0.7}_{-0.6}$ mag, and a median uncertainty of 0.2 mag. The solutions estimated omitting the FIR data are in the range $1.0 < A_{V,\text{you}}^{\text{CIG},\text{noFIR}} < 3.9$ mag, with median of $2.5^{+0.8}_{-0.5}$ mag, and a median error of 0.3 mag. The median difference of $(A_{V,\text{you}}^{\text{CIG},\text{noFIR}} - A_{V,\text{you}}^{\text{CIG},\text{FIR}})$ is 0.2 mag, which is comparable to the median uncertainties, but individual sources can reach differences of 0.9 mag.

These comparisons evidence that the absence of FIR photom-

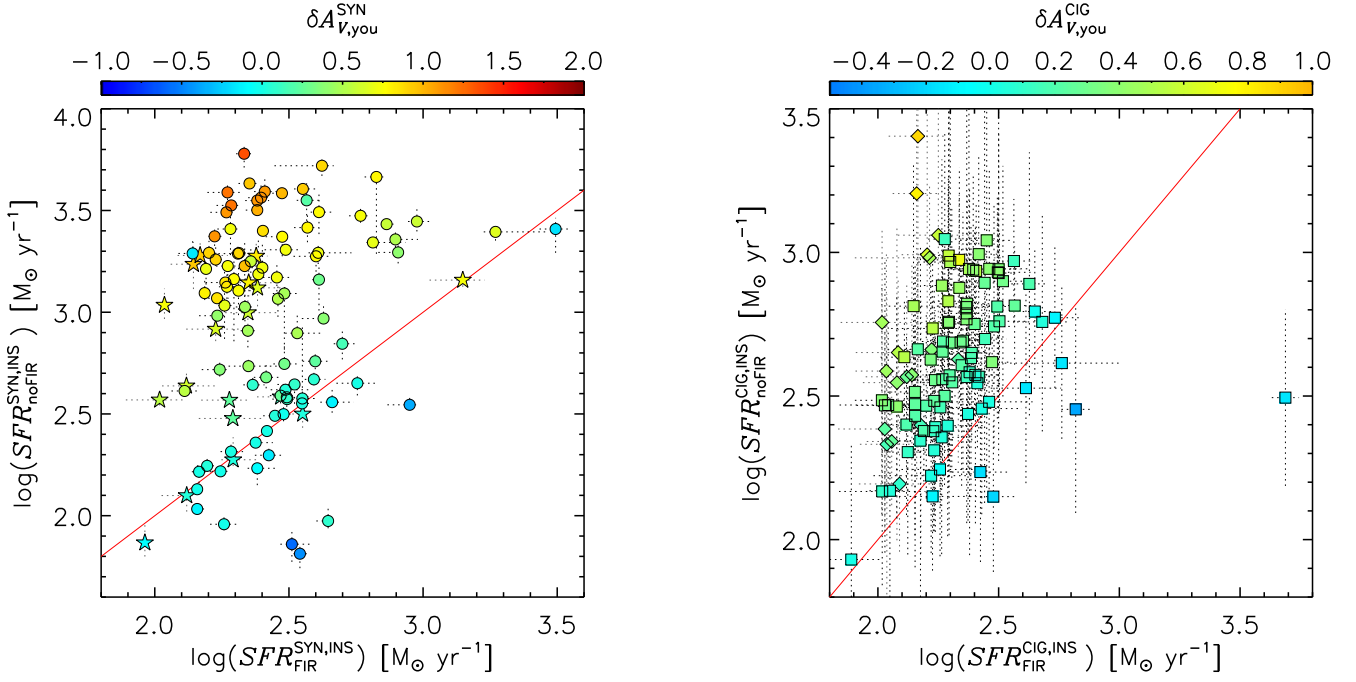


Figure 5. Comparison between the instantaneous SFR s estimated with the FIR prior on x-axis, and those obtained when the FIR data are missing on y-axis derived from the 2P models with the SYNTHESIZER (left panel) and the CIGALE (right panel) codes. The filled circles (filled stars) with error bars depict the median values and 1σ uncertainties for the main (complementary) sample determined with the SYNTHESIZER code. The filled squares (filled diamonds) with error bars stand for the expected values and standard deviations derived with the CIGALE. The difference between $A_{V,\text{you}}^{\text{noFIR}}$ and $A_{V,\text{you}}^{\text{FIR}}$, $\delta A_{V,\text{you}}$, is distinguished by colour for each code.

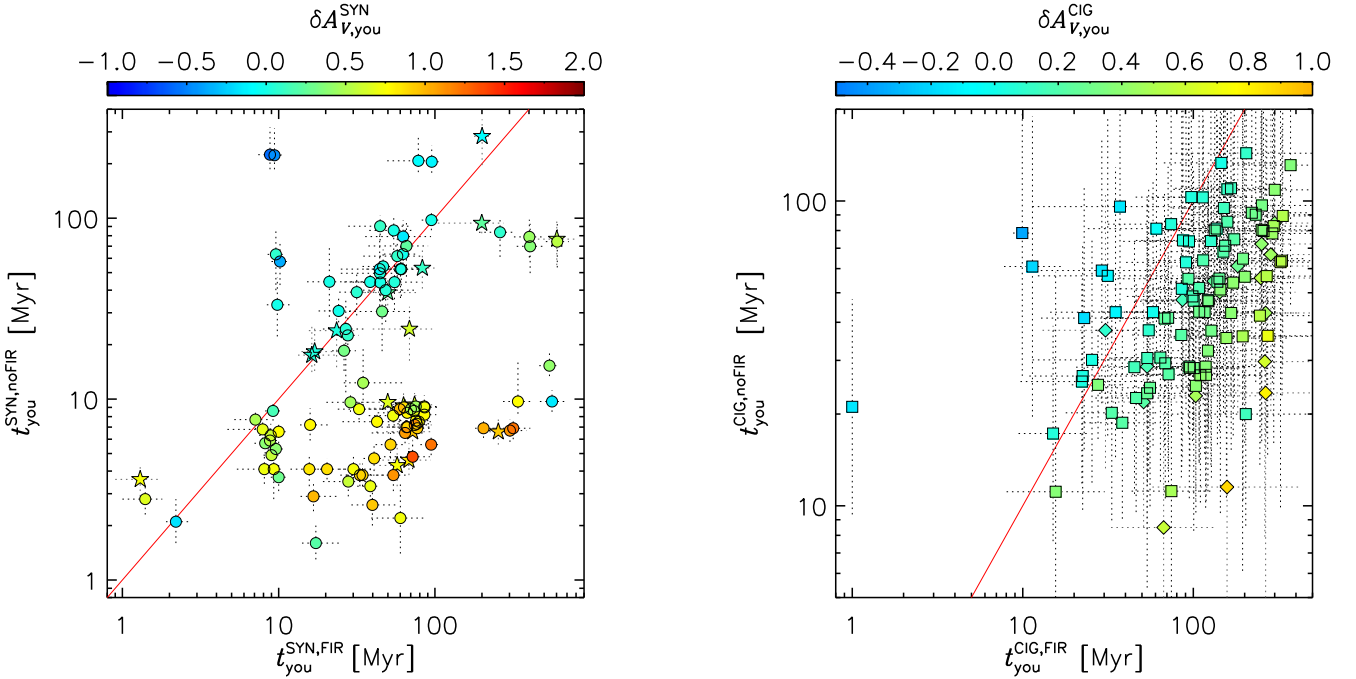


Figure 6. Comparison between the ages of the young population of the 2P models using the FIR prior on x-axis, and those determined when the FIR is omitted on y-axis estimated with the SYNTHESIZER (left panel) and the CIGALE (right panel) codes. The filled circles (filled stars) with error bars show the median values and 1σ uncertainties for the main (complementary) sample estimated with the SYNTHESIZER code. The filled squares (filled diamonds) with error bars stand for the expected values and standard deviations derived with the CIGALE. The difference between $A_{V,\text{you}}^{\text{noFIR}}$ and $A_{V,\text{you}}^{\text{FIR}}$, $\delta A_{V,\text{you}}$, is distinguished by colour for each code.

etry results mostly in an overestimation of the young-population attenuation values when 2P models are considered. However, there is not a significant difference on the median values obtained for the young-population attenuation with and without the FIR data, which may suggest that these attenuation differences are not the main source of discrepancy between the SED-based and observable-based SFR s.

As a further check of the influence of the overestimation of $A_{V,you}^{noFIR}$ in the 2P-SED-based SFR determination, we show in Fig. 5 the comparison of the instantaneous SFR s derived with and without the FIR prior from the results of both codes, with the differences for the attenuation of the young population, $\delta A_{V,you} = (A_{V,you}^{noFIR} - A_{V,you}^{FIR})$, distinguished by colour. It is clear that the 2P-SED-derived SFR differences are mainly controlled by the young-population attenuation, with larger SFR s obtained for objects with larger (overestimated, as demonstrated with the FIR-prior models) $A_{V,you}$ values. The objects which do not follow the progression of the $\delta A_{V,you}^{SYN}$ colour-bar are galaxies obtaining $t_{you}^{SYN} \lesssim 10$ Myr in one of the two modelling cases. This $\delta \log SFR - \delta A_{V,you}$ dependence is more accentuated for the SYNTHESIZER code results, but it is also discernible in the CIGALE solutions.

Now we study the behaviour of the ages of the young population. The SYNTHESIZER values derived using the FIR prior range between $1 < t_{you}^{SYN,FIR} < 607$ Myr, with median of 52^{+34}_{-42} Myr, and a median uncertainty of ~ 27 per cent. The results determined without the FIR data are in the range $1 < t_{you}^{SYN,noFIR} < 284$ Myr, with median of 9^{+54}_{-5} Myr, and a median error of ~ 18 per cent. The CIGALE solutions derived employing the FIR constraint range between $1 \leq t_{you}^{CIG,FIR} < 372$ Myr, with median of 116^{+135}_{-71} Myr, and a median uncertainty of ~ 80 per cent. The results calculated without the FIR prior are in the range $8 < t_{you}^{CIG,noFIR} < 144$ Myr, with median of 47^{+36}_{-22} Myr, and a median error of ~ 130 per cent.

The CIGALE large errors evidence the age-dust degeneracy in the 2P-noFIR models, i.e., without the FIR constraint there are a lot of models, encompassing a large range in $t_{you}^{CIG,noFIR}$ and $A_{V,you}^{CIG,noFIR}$, providing similar UV-to-NIR SEDs that compare equally well with the observed flux data points. Even when using the FIR prior, significant differences in age and attenuation estimations are seen for some galaxies from the 2 codes used in our work. This means that the broad-band UV-to-FIR SEDs can be reproduced by relatively young (50 Myr) starbursts with relatively large attenuations and SFR s (cf. Fig. 3), or by older stars (around 100 Myr) but less extinguished and with more moderated SFR s (comparable to those obtained from observables and the Kennicutt 1998 calibration).

In Figure 6, we compare the ages of the young stellar population in our sample of massive dusty starbursts for the 2 types of models and codes, colour-coding the points by the differences in the young-population attenuation. Distinctly, galaxies presenting larger attenuations have shorter young-population ages in both modelling cases and codes, which is another manifestation of the age-attenuation degeneracy. For objects with $\delta A_{V,you} > 0.3$ mag, the difference in young population ages of each set of models is larger than a factor of ~ 8 and ~ 4 on median for SYNTHESIZER and CIGALE. There are some galaxies with $\delta A_{V,you} > 0.3$ mag and young-population age differences shorter than a factor 2. This is not surprising because the presence of FIR data helps to break the age-dust degeneracy, but the young-population age is also degenerated with the intensity of the most recent burst (i.e., SFR and total mass created by the starburst). To exemplify the degeneracy between the age and the stellar mass of the young population, we return to our as-

sumed SFHs. The instantaneous SFR (our SFR^{INS}) is dominated by the contribution of the young population (which is what can be expected in dSFGs). Hence, we can approximate $SFR^{INS} \simeq SFR_{you}^{INS}$, with SFR_{you}^{INS} coming from a constant recent SFH by definition. This SFR_{you}^{INS} can be expressed as $M_{\star,you}/t_{you}$ or $M_{\star}(b/t)_{you}$, in terms of the stellar mass for the young population and the total. Then, the specific SFR for a galaxy is $sSFR^{INS} \simeq (b/t)_{you}$. Considering similar stellar masses for both 2P cases, we can refer to SFR or $sSFR$ in an interchangeable way. Then, the relation of SFR differences and young-population attenuation variations between both cases can be expressed in terms of $(b/t)_{you}$ differences and $A_{V,you}$ variations. With this in mind, we can provide a better panorama of the degeneracies presented in both 2P cases. The $A_{V,you}^{FIR}$ values are driven by the FIR prior, the L_{TIR} , which helps to break the age-dust degeneracy. The b_{you} and t_{you} are directly related with the $sSFR^{INS}$ values, where b_{you} and t_{you} are degenerated. Thus, a high value of b_{you} connected to a large value of t_{you} (i.e., a long burst forming large amounts of stars) is difficult to be disentangled from a small b_{you} associated to a small value of t_{you} (i.e., a young burst forming less stellar mass). The sources which do not follow the sequence of the $\delta A_{V,you}$ colour-bar in Figs. 5 and 6 are mainly objects presenting extreme differences in the $(b/t)_{you}$ ratio between each 2P case.

6.4 Effect of the FIR prior in the determination of the properties of the old population

Here we compare the old-population parameters estimated with the CIGALE and SYNTHESIZER codes for each 2P case. The properties of the old population of our sample of dusty massive starbursts are difficult to determine because the oldest stars are outshined by the most recent star formation event (Maraston et al. 2010).

The SYNTHESIZER old attenuations obtained using the FIR prior range in $0.0 < A_{V,old}^{SYN,FIR} < 1.5$ mag, with median of $0.1^{+0.7}_{-0.1}$ mag, and a median uncertainty of 0.1 mag. The results estimated without the FIR data are in the range $0.0 < A_{V,old}^{SYN,noFIR} < 1.5$ mag, with median of $0.2^{+0.8}_{-0.2}$ mag, and a median error of 0.1 mag. Significant differences in the derived $A_{V,old}^{SYN}$ values between the 2P models with and without FIR prior translate into M_{\star}^{SYN} estimates that differ by a factor > 2 (see Section 6.1).

For the CIGALE, the values derived with the FIR constraint range in $0.0 < A_{V,old}^{CIG,FIR} < 1.7$ mag, with median of $0.9^{+0.3}_{-0.8}$ mag, and a median uncertainty of 0.6 mag. The solutions computed omitting the FIR data are in the range $0.0 < A_{V,old}^{CIG,noFIR} < 1.8$ mag, with median of $1.0^{+0.3}_{-1.0}$ mag, and a median error of 0.8 mag.

Now we investigate the ages of the old population. The SYNTHESIZER values derived using the FIR prior range between $0.9 < t_{old}^{SYN,FIR} < 6.0$ Gyr, with median of $1.4^{+1.1}_{-0.4}$ Gyr, and a median uncertainty of 0.3 Gyr. The results determined without the FIR data are in the range $0.9 < t_{old}^{SYN,noFIR} < 4.7$ Gyr, with median of $1.4^{+0.7}_{-0.4}$ Gyr, and a median error of 0.2 Gyr. The CIGALE solutions obtained employing the FIR constraint range between $1.1 < t_{old}^{CIG,FIR} < 5.6$ Gyr, with median of $3.3^{+0.8}_{-0.5}$ Gyr, and a median uncertainty of 1.6 Gyr. The results calculated without the FIR data are in the range $1.5 < t_{old}^{CIG,noFIR} < 5.3$ Gyr, with median of $3.4^{+0.9}_{-0.2}$ Gyr, and a median error of 1.5 Gyr. For the old-population age, the values obtained by each code and both 2P cases are very similar for all the galaxies. Only for a small fraction of galaxies, 21 and 13 per cent of all our sample, the ages of the old stars differ significantly when comparing SYNTHESIZER and CIGALE results with

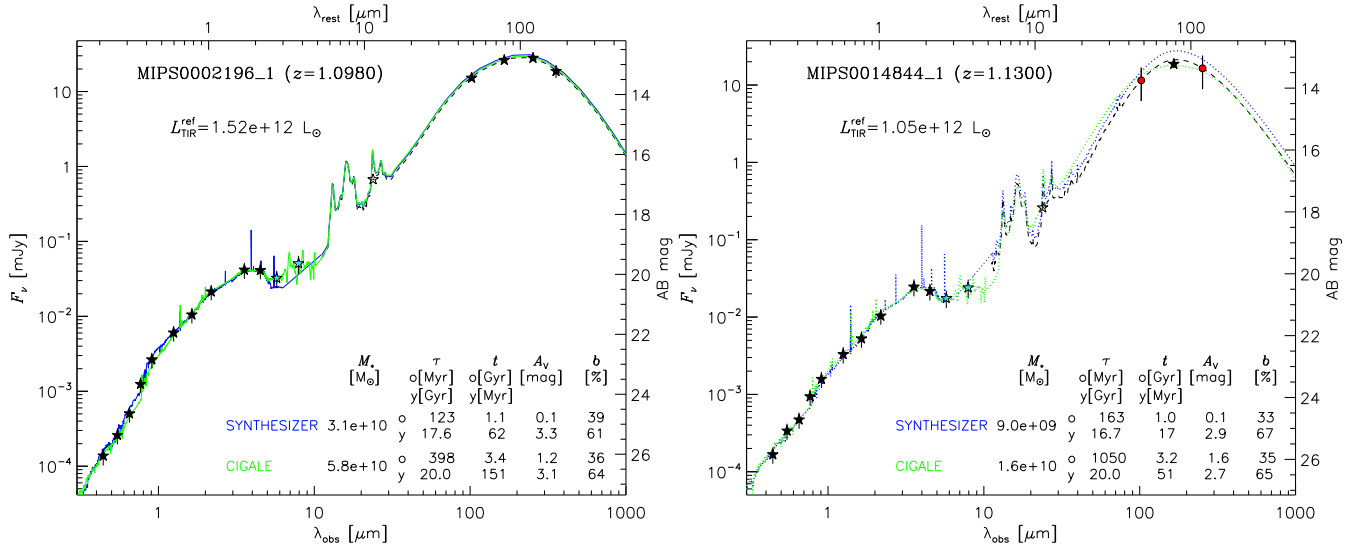


Figure 7. Two examples of the resulting fit to the UV-to-FIR SED for our $0.7 \leq z \leq 1.2$ dusty starbursts. *Left panel:* Results of the fitting process for the most significant cluster identified with the SYNTHESIZER code (solid blue line), and the fit obtained with the Bayesian analysis of the CIGALE (solid green line) for a source in the main sample. The parameter values obtained from each code are also shown. The fit to the FIR photometry ($\lambda_{\text{obs}} \geq 70 \mu\text{m}$, dashed black line) and its associated $L_{\text{TIR}}^{\text{ref}}$ are indicated. Photometric data points include uncertainties, only the filled black stars are used in the SYNTHESIZER fit, while the filled black and cyan stars are used in the CIGALE fit. *Right panel:* The same as left panel for a source in the complementary sample. The fits obtained for the SYNTHESIZER and the CIGALE codes are shown with a dotted blue line and a dotted green line. The filled red circles stand for synthetic fluxes in the FIR filters (see Section 4.1), and they are also used in the fit from each code. The UV-to-FIR SEDs of all galaxies are presented as online material.

and without FIR prior. Therefore, the addition of FIR data has a minor impact in the determination of the ages of the old population. This is expected because the FIR photometry traces the dust content of the galaxies, which is related to the most recent star formation events.

Buat et al. (2014) studied a sample of $z > 1$ galaxies with CIGALE using 2P models and the FIR prior. These authors found compatible trends in the ages of both populations with and without the addition of FIR information. Hence, our findings are similar to their results for the old stellar population, but not for the young population case. We have reported a significant change in the young population ages for more than half of the objects in our sample when the FIR data are omitted (see Fig. 6).

7 A COMPREHENSIVE VIEW ON THE NATURE OF $0.7 < z < 1.2$ MASSIVE DUSTY STARBURSTS

In Section 6 we studied how the inclusion of FIR data in the modelling procedure affects the results about the stellar properties of massive dusty starburst galaxies at intermediate redshift. In this Section, we discuss the models simultaneously reproducing the stellar and dust emission (i.e., using the FIR prior) and compare the solutions obtained by SYNTHESIZER and CIGALE, putting them in the context of other works found in the literature.

In Table 5 we present the results of the 2P-FIR models applied to our sample of dusty star-forming galaxies. We show in Fig. 7 the complete UV-to-FIR SEDs for one source in the main sample and one galaxy in the complementary sample. We also provide the results of the median solution of the most significant cluster derived from the Monte-Carlo simulation analysis with the SYNTHESIZER code, and the average parameter values estimated with the CIGALE from the Bayesian analysis of its full set of models. We evaluated the goodness of the fits, using a reduced χ^2 -estimator including

the UV-to-MIR and FIR part of the spectrum of each galaxy (see, Fig. 7) separately. Although the SYNTHESIZER code performs better than CIGALE in the FIR spectral range (χ^2_{TIR} median, and 16 and 84-percentile of $1.5^{+2.1}_{-1.2}$ and $3.6^{+9.2}_{-3.3}$, respectively), we do not find any statistically relevant difference in the quality of the fits provided by the 2 codes.

7.1 Discussion about the properties of the young stellar population

Here we compare the young-population parameters derived from the models including a FIR prior provided by the SYNTHESIZER and CIGALE codes. These parameters are also contrasted with results from the literature. Given that we fixed the value of the metallicity for both codes and also τ_{you} is unvaried (assuming a constant SFH), we focus our discussion on the attenuation $A_{V,\text{you}}^{\text{FIR}}$, the age $t_{\text{you}}^{\text{FIR}}$, and the recent burst intensity $b_{\text{you}}^{\text{FIR}}$. The distributions of values for these properties are presented in Fig. 8, and their median solutions are shown in Table 6, both for the full sample of massive dusty starburst galaxies.

7.1.1 Discussion about the attenuation of the young stellar population

The typical attenuation of the young stellar population in our sample of massive dusty starburst galaxies is 2.4 mag. The 2 codes used in our paper provide similar results for $A_{V,\text{you}}^{\text{FIR}}$ (within 0.1 mag, on median), as expected considering the energy balance approach that the codes use. In fact, there is a clear correlation between each set of estimated values with Spearman correlation coefficient of $r_s = 0.96$, and an associated probability of no correlation of $p_s = 7.0 \times 10^{-45}$. The majority of our objects (70 per cent) presents $A_{V,\text{you}}^{\text{FIR}} > 2$ mag,

Table 5. Stellar population synthesis results for main-sample dusty starbursts. Median and 1σ error values are shown for each parameter derived with the SYNTHESIZER code. The expected and standard deviation (or upper and lower limits when changing from logarithmic space to linear space) values are quoted for each parameter estimated with the CIGALE. (1) Name of the galaxy. (2) Photometric or spectroscopic redshift (z_{spec} indicated by a \dagger). (3) Code used to derive the parameters. (4) Stellar mass (in solar units) and its uncertainty derived from the logarithmic space. (5) Parameter values for the old or the young population. (6) e -folding time and its uncertainty (old population in Myr and young population in Gyr). (7) Age and its uncertainty (old population in Gyr and young population in Myr). (8) Attenuation in the V -band and its uncertainty in mag. (9) Metallicity value (fixed to the solar value) in solar units. (10) Most recent burst intensity fraction and its uncertainty in percentage. (This Table and that for the complementary sample are available in its entirety in the online journal.)

Galaxy	z^\dagger	Code	$\log M_\star$ [M_\odot]	Pop.	τ old [Myr] you [Gyr]	Age old [Gyr] you [Myr]	A_V [mag]	Z [Z_\odot]	b [%]
(1)	(2)	(3)	(4)	(5)	(6)	(7)	(8)	(9)	(10)
MIPS0000517A	1.0500	SYNTHESIZER	$10.0^{+0.1}_{-0.1}$	old	230^{+43}_{-125}	$1.0^{+0.2}_{-0.1}$	$0.0^{+0.1}_{-0.0}$	1.0	
				you	$18.5^{+3.1}_{-3.2}$	39^{+6}_{-7}	$1.9^{+0.1}_{-0.1}$	1.0	69^{+2}_{-23}
		CIGALE	10.1 ± 0.2	old	1280^{+5762}_{-1047}	3.2 ± 1.6	$1.0^{+0.7}_{-0.7}$	1.0	
				you	20.0	46^{+34}_{-20}	1.9 ± 0.2	1.0	61 ± 26
MIPS0000648A	1.1900	SYNTHESIZER	$10.4^{+0.1}_{-0.1}$	old	162^{+46}_{-45}	$1.0^{+0.1}_{-0.1}$	$0.0^{+0.1}_{-0.0}$	1.0	
				you	$17.7^{+3.4}_{-2.7}$	45^{+21}_{-19}	$2.3^{+0.1}_{-0.1}$	1.0	51^{+13}_{-16}
		CIGALE	10.6 ± 0.1	old	1189^{+5363}_{-973}	3.2 ± 1.6	$1.2^{+0.7}_{-0.7}$	1.0	
				you	20.0	100^{+90}_{-47}	2.2 ± 0.2	1.0	57 ± 27
MIPS0000816_1	0.9300	SYNTHESIZER	$10.2^{+0.2}_{-0.2}$	old	141^{+113}_{-45}	$2.4^{+1.0}_{-0.5}$	$0.0^{+0.3}_{-0.0}$	1.0	
				you	$18.9^{+2.9}_{-3.2}$	8^{+1}_{-1}	$1.5^{+0.1}_{-0.1}$	1.0	21^{+18}_{-10}
		CIGALE	9.9 ± 0.3	old	1285^{+5815}_{-1053}	4.1 ± 1.6	$0.5^{+0.4}_{-0.4}$	1.0	
				you	20.0	22^{+29}_{-13}	1.1 ± 0.2	1.0	49 ± 30
MIPS0000826	0.7200	SYNTHESIZER	$10.5^{+0.1}_{-0.1}$	old	247^{+32}_{-37}	$3.0^{+0.4}_{-0.3}$	$0.0^{+0.1}_{-0.0}$	1.0	
				you	$19.8^{+2.5}_{-2.4}$	9^{+1}_{-1}	$3.2^{+0.1}_{-0.1}$	1.0	25^{+3}_{-5}
		CIGALE	10.7 ± 0.1	old	314^{+686}_{-215}	5.5 ± 1.4	$0.0^{+0.1}_{-0.0}$	1.0	
				you	20.0	10^{+1}_{-1}	3.2 ± 0.2	1.0	11 ± 4
MIPS0002196_1	1.0980 \dagger	SYNTHESIZER	$10.5^{+0.1}_{-0.1}$	old	123^{+50}_{-25}	$1.1^{+0.4}_{-0.2}$	$0.1^{+0.1}_{-0.1}$	1.0	
				you	$17.6^{+3.4}_{-2.7}$	62^{+17}_{-15}	$3.3^{+0.1}_{-0.1}$	1.0	61^{+6}_{-7}
		CIGALE	10.8 ± 0.1	old	398^{+1650}_{-320}	3.4 ± 1.6	$1.2^{+1.1}_{-1.1}$	1.0	
				you	20.0	151^{+150}_{-75}	3.1 ± 0.2	1.0	64 ± 25

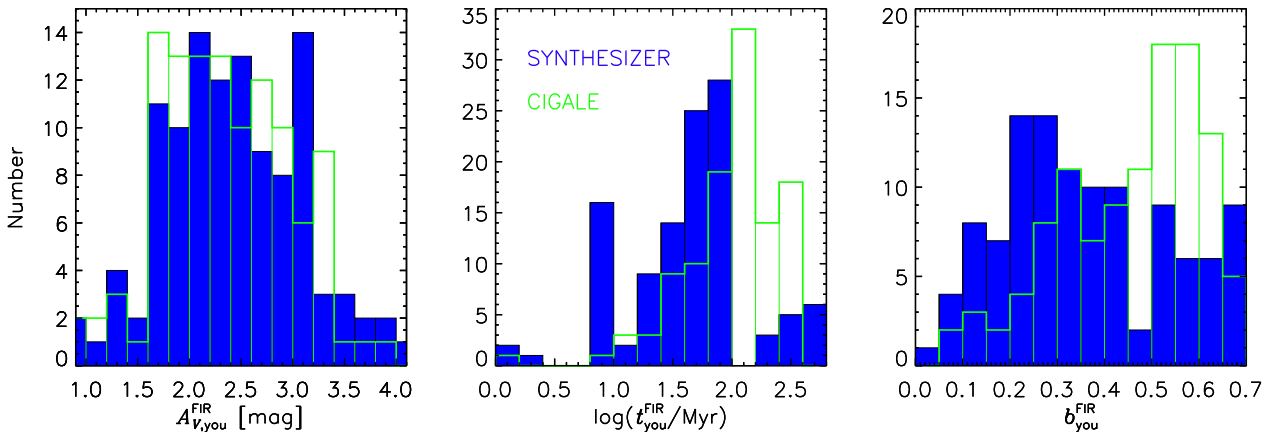


Figure 8. Properties of the young stellar population of the whole sample of dusty starbursts derived using the FIR prior. From left to right, attenuation, age, and burst intensity. The fill blue histograms stand for the results determined with the SYNTHESIZER code. The open green histograms show the results obtained with the CIGALE.

which is not surprising given that our sample selection is based on the FIR emission.

We have compared our results about attenuation with other studies in the literature. [Buat et al. \(2015\)](#) used CIGALE to study galaxies selected at $8\ \mu\text{m}$ rest-frame and lying at $z \approx 0.2 - 2$, with some of these objects including PACS measurements. They found that at $\langle z \rangle = 0.9$, the average young attenuation under a Calzetti-like curve is $\langle A_{V,\text{you}} \rangle \approx 1.4$ mag. We have to mention that the average $\langle \log L_{\text{TIR}}/L_{\odot} \rangle$ for these sources is 11.46, which is smaller than the average $\langle \log L_{\text{TIR}}^{\text{ref}}/L_{\odot} \rangle = 12.04$ of the objects in our sample. We also note that in our study, we probed shorter young population age values than [Buat et al.](#) From the CIGALE results for our sample, there are 93 galaxies (83 per cent of all sources) with $t_{\text{you}}^{\text{CIG,FIR}}$ older than 50 Myr (the [Buat et al.](#) lowest young age value), from these 93, 64 objects present $A_{V,\text{you}}^{\text{CIG,FIR}} > 2$ mag.

We have also compared our results with sub-mm-selected samples analysed with energy-balance techniques. [da Cunha et al. \(2015\)](#) examined the ALESS sample of $z > 1$ SMGs in the ECDF-S field, which contains multi-wavelength data, including FIR detections. They used a modified version of the MAGPHYS code ([da Cunha et al. 2008](#)) to derive physical properties of these objects. They found an overall attenuation $A_V = 1.9 \pm 0.2$ mag, similar to our calculations. [Danielson et al. \(2017\)](#) presented a spectroscopic catalogue of the aforementioned ALESS sample identifying redshifts in the range $z_{\text{spec}} = 0.7 - 5.0$. They also used MAGPHYS to fit the SEDs for these objects, finding A_V values spanning from 0.5 to 7 mag. [Dudzevičiūtė et al. \(2020\)](#) analysed an $870\text{-}\mu\text{m}$ selected sample in SXDS/UDS field, including *Herschel* detections, with median redshift $z \approx 2.6$. They find a median attenuation of $A_V = 2.89 \pm 0.04$ mag using MAGPHYS too, similar to our results. [Casey et al. \(2017\)](#) presented NIR and optical spectra of a sub-mm-selected sample at $0.2 < z < 4$ in the COSMOS field. They determined a median attenuation $A_V = 5.0 \pm 0.4$ mag by measuring Balmer decrements. If those sources are similar to ours, the ionized gas attenuation would be roughly twice the stellar attenuation, as found by [Calzetti et al. \(2000\)](#).

Considering all these findings in the literature, we conclude that the attenuation values derived for the young population in our galaxy sample are within the standard range of values for dSFGs at intermediate and high redshift, typically $A_V = 2.5$ mag.

7.1.2 Discussion about the age of the young stellar population

The recent star-forming events harboured by the dusty starburst galaxies in our sample present ages of several tens and up to a hundred Myr. There is a systematic difference in the derived ages for the 2 codes, with the SYNTHESIZER code favouring shorter ages than CIGALE (by around a factor of 2). To quantify the level of correlation between the young-population age values obtained from both codes, we estimated the Spearman correlation coefficient resulting in $r_s = 0.71$, with a probability $p_s = 1.6 \times 10^{-18}$ of getting this result as a mere coincidence. We interpret this difference in terms of the moderately higher *SFRs* and slightly smaller stellar masses derived by SYNTHESIZER (see Sections 6.1 and 6.2).

The SFH assumed for the young population is practically constant. Considering that, on average, we should be observing galaxies with ages similar to half of the lifetime that an object stays in the starburst phase, and that our median starburst ages are $\sim 50 - 120$ Myr, we can infer a duration of the starburst phase of $\sim 100 - 250$ Myr. This value is in agreement with the results deduced for the lifetime of the starburst phase of SMGs

Table 6. Median, and 16 and 84-percentile values of the FIR-prior fitted parameters for the full-sample of dusty starbursts. From top to bottom, attenuation, age and burst intensity for the young population, attenuation, age and e -folding time for the old population, stellar mass, mass-weighted age and SED-derived 10-Myr-averaged *SFR*.

Parameter	CIGALE	SYNTHESIZER
$A_{V,\text{you}}^{\text{FIR}}$ [mag]	$2.3^{+0.7}_{-0.6}$	$2.4^{+0.7}_{-0.7}$
$t_{\text{you}}^{\text{FIR}}$ [Myr]	116^{+135}_{-71}	51^{+34}_{-42}
$b_{\text{you}}^{\text{FIR}}$ [%]	50^{+10}_{-21}	34^{+25}_{-18}
$A_{V,\text{old}}^{\text{FIR}}$ [mag]	$0.9^{+0.3}_{-0.8}$	$0.1^{+0.7}_{-0.1}$
$t_{\text{old}}^{\text{FIR}}$ [Gyr]	$3.3^{+0.8}_{-0.5}$	$1.4^{+1.1}_{-0.4}$
$\tau_{\text{old}}^{\text{FIR}}$ [Myr]	952^{+457}_{-833}	158^{+63}_{-42}
$\log(M_{\star}^{\text{FIR}}/M_{\odot})$	$10.71^{+0.30}_{-0.41}$	$10.58^{+0.28}_{-0.37}$
t_M^{FIR} [Gyr]	$0.9^{+0.9}_{-0.3}$	$0.8^{+0.7}_{-0.3}$
SFR_{FIR}^{10} [$M_{\odot}\text{ yr}^{-1}$]	196^{+105}_{-65}	241^{+155}_{-74}

($\sim 100 - 300$ Myr; [Swinbank et al. 2006](#); [Tacconi et al. 2008](#); [Hickox et al. 2012](#); [Donevski et al. 2020](#)). If we combine these star formation time-scales with the median *SFRs* presented in Section 6.2 and Table 6, we obtain that massive dusty galaxies at intermediate redshift typically increase their mass by 30–50 per cent in a starburst phase.

7.1.3 Discussion about the intensity of the most recent burst

Further discussion about how much mass the starburst phase adds can be presented based on the burst strengths fitted by our modelling procedure. The typical recent burst intensities ($b_{\text{you}}^{\text{FIR}}$) are $0.34^{+0.26}_{-0.18}$ and $0.50^{+0.10}_{-0.21}$ (similar to the stellar-mass increase derived in Section 7.1.2), with median uncertainties of ~ 23 and ~ 54 per cent for the SYNTHESIZER code and CIGALE, respectively. We do not find an obvious correlation between the two estimations.

[Giovannoli et al. \(2011\)](#) used CIGALE to study a $24\text{-}\mu\text{m}$ selected sample at $z \sim 0.7$, with some galaxies including MIPS-70 detections. They explored burst intensities (their f_{ySP}) from 0 to 0.99 finding a broad distribution with a long tail towards high values for this parameter. In the work of [Buat et al. \(2014\)](#), also carried out with CIGALE, they explored f_{ySP} until 0.5, which is compatible with most of our objects (73 and 51 per cent of all galaxies from the analysis with the SYNTHESIZER code and the CIGALE). We should take in mind that we are selecting sources in the ULIRG regime, and these objects should be suffering vigorous starburst events (see, e.g., [Rowlands et al. 2014](#); [Lemaux et al. 2014](#)). Therefore, we consider that our $b_{\text{you}}^{\text{FIR}}$ results are within the typical values (0.2–0.6) of dSFGs.

7.2 Discussion about the properties of the old stellar population

In this Subsection, we present the main properties of the old stellar population in our sample of dusty massive starburst galaxies at $z \sim 1$ according to SYNTHESIZER and CIGALE. In particular, we discuss the attenuation ($A_{V,\text{old}}^{\text{FIR}}$), the age ($t_{\text{old}}^{\text{FIR}}$), and the exponential decay factor ($\tau_{\text{old}}^{\text{FIR}}$). The distributions of values for these parameters are shown in Fig. 9, and their median solutions are presented in Table 6, both for the whole sample of massive dusty starburst galaxies.

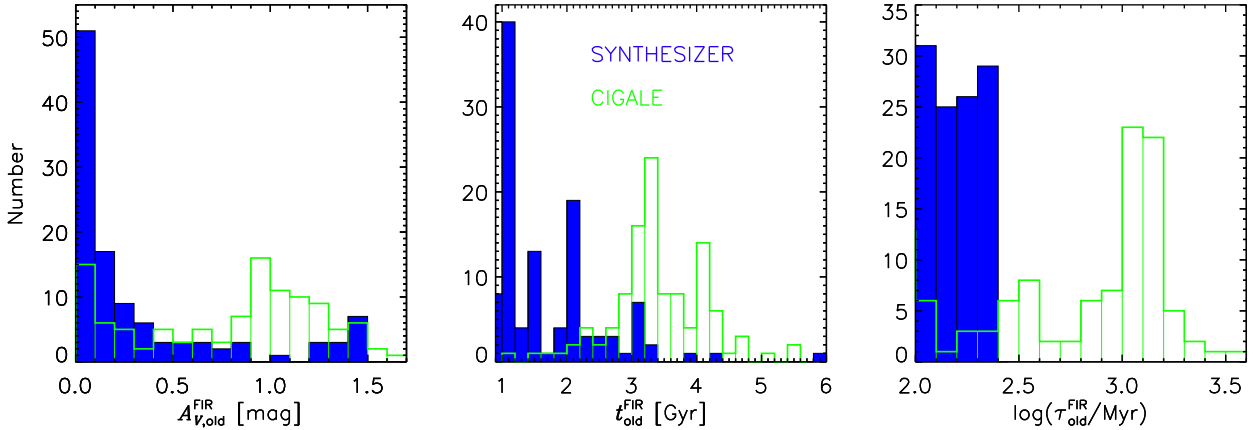


Figure 9. Properties of the old stellar population of the whole sample of dusty starbursts derived using the FIR prior. From left to right, attenuation, age, and e -folding time. The fill blue histograms stand for the results determined with the SYNTHESIZER code. The open green histograms show the results obtained with the CIGALE.

7.2.1 Discussion about the attenuation of the old stellar population

The median old-population attenuations in our sample of massive dusty starburst are $0.1^{+0.7}_{-0.1}$ and $0.9^{+0.3}_{-0.8}$ mag, with median errors of 0.1 and 0.6 mag for SYNTHESIZER and CIGALE. We do not find a perceptible correlation between the two estimates. The SYNTHESIZER median is compatible with the SED-derived median attenuation of quiescent galaxies at $0.1 \leq z \leq 1.1$, $A_V \sim 0.15 - 0.3$ mag (Díaz-García et al. 2019). Although the results of both codes range in comparable intervals (see Section 6.4), the CIGALE yields $A_{V,old}^{CIG,FIR} > 1.0$ mag for 40 per cent of all galaxies. Such values seem to be too large for old populations with ages $\sim 3 - 4$ Gyr. However, Małek et al. (2017) found average $A_{V,old}^{CIG,FIR} \sim 0.7$ mag for a sample of (U)LIRGs at $0.1 < z < 1.2$ examined with CIGALE, which is compatible with our findings. The SYNTHESIZER code only yields $A_{V,old}^{SYN,FIR} > 1.0$ mag for 13 per cent of all objects. A fraction of 50 per cent of all sources presents $A_{V,old}^{SYN,FIR} < 0.1$ mag from the SYNTHESIZER code, whereas only 15 per cent fulfils this condition from the results of CIGALE. We remark that the attenuation of the old population is linked to the attenuation of the younger population for CIGALE, while it is a completely independent parameter for SYNTHESIZER. Considering all of the above, we observe that the old-population attenuation is not constrained accurately, the 68th percentile range of the difference between the values derived with CIGALE and SYNTHESIZER is 0.8 mag. Our analysis indicates that the old population attenuation is around 0.1 – 0.9 mag, most probably in the lowest half of that interval.

7.2.2 Discussion about the age of the old stellar population

The median old stellar ages of our dusty starburst galaxies are $1.4^{+1.1}_{-0.4}$ and $3.3^{+0.8}_{-0.5}$ Gyr, with median uncertainties of ~ 20 and ~ 47 per cent for SYNTHESIZER and CIGALE. There is a mild correlation between each set of computed values with Spearman correlation coefficient of $r_s = 0.45$ and an associated probability of no correlation of $p_s = 7.0 \times 10^{-7}$. The SYNTHESIZER code tends to obtain shorter old-population ages for a significant part of the sample. We note that these younger ages are accompanied with shorter e -folding times (cf. Fig 9), which are described in the Subsection 7.2.3. Ages and e -folding times are, indeed, quite degenerate. If

we combine both properties in a single parameter, a mass-weighted age, SYNTHESIZER and CIGALE provide much more similar results: the medians are $0.8^{+0.7}_{-0.3}$ and $0.9^{+0.9}_{-0.3}$ Gyr, respectively.

7.2.3 Discussion about the e -folding time of the old stellar population

The old stellar population e -folding times of our dusty starbursts range in $101 < \tau_{old}^{SYN,FIR} < 249$ and $100 \leq \tau_{old}^{CIG,FIR} < 3398$ Myr, with medians of 158^{+63}_{-42} and 952^{+457}_{-833} Myr, and median errors of ~ 25 and ~ 150 per cent for the SYNTHESIZER and CIGALE codes. We do not find an obvious correlation between the two estimations. Although the values of τ_{old}^{FIR} derived with each code are similar for ~ 40 per cent of all galaxies (with differences within a factor of 2), the CIGALE systematically finds higher values of τ_{old}^{FIR} for most objects, compared to the results provided by SYNTHESIZER. Such differences are compensated in CIGALE with less intense initial bursts. This effect, at least in part, could be caused by the few discrete values examined in the CIGALE case (0.1, 1, 3, and 10 Gyr). We have used in this study a similar set of $\tau_{old}^{CIG,FIR}$ values to the ones explored in several works using the CIGALE (see, e.g., Noll et al. 2009; Giovannoli et al. 2011; Buat et al. 2014). In such studies, those authors found that the $\tau_{old}^{CIG,FIR}$ values are unsatisfactory estimated, and almost unconstrained.

7.3 Comparison of stellar masses and SFRs from 2P-FIR models

Now we compare stellar masses and SFRs derived using the FIR prior with the SYNTHESIZER and CIGALE codes for our sample of massive dusty starburst galaxies. Such parameters are contrasted with results from the literature. To do so, we account for different IMF and SPS models assumptions when possible⁶.

⁶ We transform from a Chabrier (2003) IMF to a Salpeter (1955) one multiplying by a factor of 1.6 (Salimbeni et al. 2009; Marchesini et al. 2009; Barro et al. 2011b). Stellar masses derived with the Bruzual & Charlot (2003) models have been shown to be a factor ~ 1.5 larger than those determined with the Maraston (2005) ones (Muzzin et al. 2009; Hainline et al. 2011; Casey et al. 2014). Thus, $M_{\star}^{M05,SAL} \approx M_{\star}^{BC03,CHA}$ and, consequently, SFRs.

As mentioned in Section 6.1, the typical stellar masses of our sample are 3.8×10^{10} and $5.2 \times 10^{10} M_{\odot}$, for SYNTHESIZER and CIGALE, respectively. On median, stellar masses calculated with CIGALE are 37 per cent larger than those obtained with SYNTHESIZER. We find that this mass ratio increases as the old-population age ratio, $t_{\text{old}}^{\text{CIG,FIR}}/t_{\text{old}}^{\text{SYN,FIR}}$, rises ($r_s = 0.59$, $p_s = 1.04 \times 10^{-11}$). Then, this ~ 0.1 dex difference can be attributed to the larger old populations ages derived with CIGALE (see Section 7.2.2). The larger the old-population ages, the more stellar mass that may be enshrouded in low-mass stars (Hainline et al. 2011; Michałowski et al. 2014; da Cunha et al. 2015).

We compared our estimates with stellar masses derived for MIR/FIR-selected (U)LIRGs at similar redshifts. Melbourne et al. (2008) studied 15 LIRGs at $z \sim 0.8$ selected at $24 \mu\text{m}$ in the GOODS-S HST treasury field. They estimated a median stellar mass of $5.9 \times 10^{10} M_{\odot}$ for such LIRGs. Giovannoli et al. (2011) examined 172 LIRGs selected at $24 \mu\text{m}$ in ECDF-S at $z \sim 0.7$. They found that the distribution of their stellar mass estimates peaks at $6.3 \times 10^{10} M_{\odot}$. Lemaux et al. (2014) analysed a *Herschel*/SPIRE-selected sample of ~ 2000 galaxies from $0 < z < 4$ in the CFHTLS-D1 field. Cutting their sample to ULIRGs at $0.7 < z < 1.2$, we found 109 sources with a median stellar mass of $4.2 \times 10^{10} M_{\odot}$.

We have also contrasted our stellar mass values with those of SMGs. Rowlands et al. (2014) found 26 (U)LIRGs in their $250\text{-}\mu\text{m}$ selected sample with a median redshift $z \approx 2$. They estimated for these sources a median stellar mass of $5.1 \times 10^{10} M_{\odot}$. da Cunha et al. (2015) reported 86 (U)LIRGs in the analysis of the ALESS sample with a median redshift of 2.7. They derived a median stellar mass of $5.7 \times 10^{10} M_{\odot}$. Miettinen et al. (2017) found 102 (U)LIRGs in their 1.3-mm selected sample in the COSMOS field with a median redshift of $z \approx 2.1$. They derived a median stellar mass of $1.3 \times 10^{11} M_{\odot}$. When considering only the 18 (U)LIRGs with 68th percentile range of z compatible with lying in $0.7 < z < 1.2$, the median stellar mass is $6.4 \times 10^{10} M_{\odot}$. Dudzevičiūtė et al. (2020) reported 689 (U)LIRGs in their $870\text{-}\mu\text{m}$ selected sample with a median redshift of $z \approx 2.6$. They estimated a median stellar mass of $1.2 \times 10^{11} M_{\odot}$. When comparing only the 20 (U)LIRGs with 1σ range of z consistent with lying in $0.7 < z < 1.2$, the median stellar mass is $7.1 \times 10^{10} M_{\odot}$.

Martis et al. (2016) built a stellar-mass complete sample using the UltraVISTA DR1 and 3D-HST photometric catalogues. They used optical colours to study the fraction of dSFGs as a function of stellar mass at $0.2 < z < 3.0$. They found that at $z < 1.5$, dSFGs dominate the galaxy population in the stellar mass range $1 \times 10^{10} < M_{\star}/M_{\odot} < 3.9 \times 10^{10}$. They stated that dSFGs are a factor $\sim 3 - 5$ more abundant at $M_{\star} > 3.9 \times 10^{10} M_{\odot}$ than unobscured star-forming galaxies.

Considering the stellar-mass values determined in the aforementioned studies, we conclude that the stellar masses derived for our sample using both codes are compatible with those of (U)LIRGs and optical-selected dSFGs at $0.7 < z < 1.2$, and also with those of SMGs at $z > 1$.

Concerning *SFRs*, the typical SED-based value is $200 - 250 M_{\odot}\text{yr}^{-1}$, with very similar values provided by the 2 codes.

Now we compare our sample results with *SFR* estimations from the literature. Lemaux et al. (2014) determined *SFRs* using the Kennicutt (1998) calibration. We selected ULIRGs at $0.7 < z < 1.2$ from their sample, obtaining a median of $SFR_{\text{TIR}}^{\text{Lem}} = 260^{+115}_{-67} M_{\odot} \text{yr}^{-1}$. Rowlands et al. (2014) and da Cunha et al. (2015) presented *SFRs* derived using the MAGPHYS code for their SMGs, with medians of $SFR_{\text{SED}}^{\text{Row}} = 407^{+168}_{-339}$ and

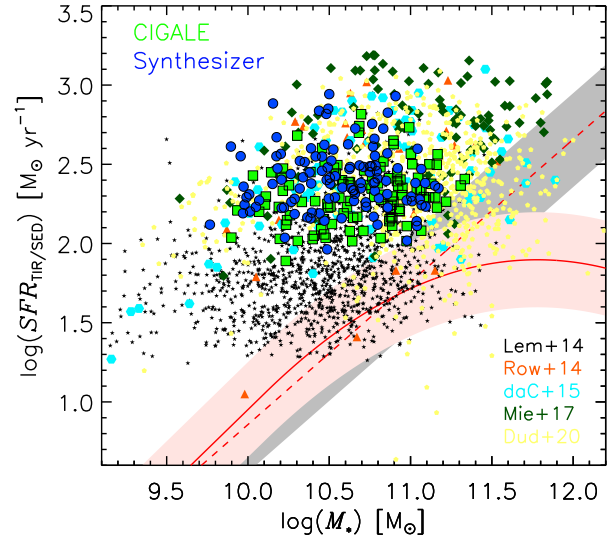


Figure 10. Stellar mass, M_{\star} , vs. *SFR* determined with the Kennicutt (1998) calibration, SFR_{TIR} , or *SFR* based on SED analysis, SFR_{SED} (see the text). The filled circles show the median values estimated with the SYNTHESIZER code. The filled squares show the expected values estimated with the CIGALE. The median values of (U)LIRGs from several FIR/sub-mm selected samples are also shown: Lemaux et al. (2014) as black stars, Rowlands et al. (2014) as orange triangles, da Cunha et al. (2015) as cyan hexagons, Miettinen et al. (2017) as dark green diamonds, and Dudzevičiūtė et al. (2020) as pale yellow pentagons. Error bars are omitted for clarity. We also depict the relationships for the main sequence at $z \sim 1$ of Elbaz et al. (2007, dashed red line) with its 68 confidence level (grey shaded area), and of Schreiber et al. (2015, solid red line) with its 0.3 dex scatter (rose shaded area).

$SFR_{\text{SED}}^{\text{daC}} = 251^{+304}_{-122} M_{\odot} \text{yr}^{-1}$ for the aforementioned (U)LIRGs, respectively. Miettinen et al. (2017) estimated *SFRs* utilising the Kennicutt (1998) factor too. They report a median of $SFR_{\text{TIR}}^{\text{Mie}} = 566^{+492}_{-302} M_{\odot} \text{yr}^{-1}$ for (U)LIRGs. When considering only the 18 (U)LIRGs with 68th percentile range of z compatible with lying in $0.7 < z < 1.2$, the median value is $270^{+186}_{-187} M_{\odot} \text{yr}^{-1}$. Dudzevičiūtė et al. (2020) derived *SFRs* using MAGPHYS too, finding a median of $SFR_{\text{SED}}^{\text{Dud}} = 233^{+216}_{-120} M_{\odot} \text{yr}^{-1}$ for (U)LIRGs.

Considering the *SFRs* estimated in the aforementioned studies for our $L_{\text{TIR}}^{\text{ref}}$ range, we conclude that the *SFRs* determined for our sample are compatible with those of *Herschel*-selected ULIRGs at $0.7 < z < 1.2$, and 1σ lower-limit values of $z > 1$ sub-mm sources.

A natural extension after comparing stellar masses and *SFRs* is to place the galaxies of the aforementioned 6 samples in the $SFR - M_{\star}$ plane, that we show in Fig. 10. Given that our massive dusty starburst are at $0.7 \leq z \lesssim 1.2$, we have also plotted in this Figure, the $SFR - M_{\star}$ relation of Elbaz et al. (2007) and the one of Schreiber et al. (2015), both at $z \sim 1$. Considering our selection criteria FIR-detected dSFGs galaxies, 1σ away from the $z \sim 1$ MS, what we should recognize are sources above or to the left of such MS. In general, samples selected by means of the dust emission (MIR/FIR or sub-mm selected) are expected to be found above or to the left of the MS (taking into account their median redshift), or lying on the MS. This is what is observed in Fig. 10, also for the Lemaux et al. (2014) sample, and it is also found in other works devoted to MIR/FIR selected samples (see, e.g., Giovannoli et al. 2011; Lee et al. 2013).

Our dusty starbursts occupy a space in the $SFR - M_{\star}$ plane

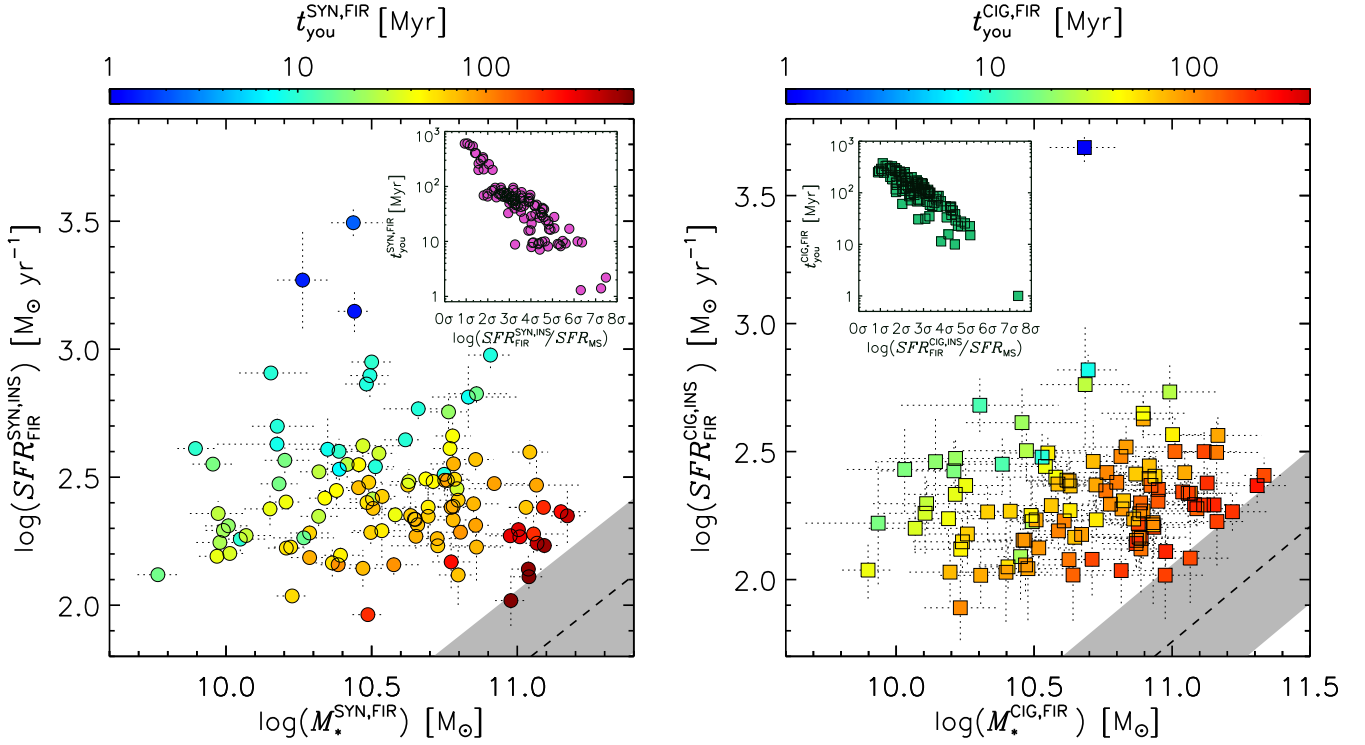


Figure 11. M_* vs. SFR^{INS} estimated with the FIR prior, computed with the SYNTHESIZER (left panel) and the CIGALE (right panel) codes. The filled circles with error bars depict the median values and 1σ uncertainties determined with the SYNTHESIZER code. The filled squares with error bars stand for the expected values and standard deviations derived with the CIGALE. The young-population age, $t_{\text{you}}^{\text{FIR}}$, is differentiated by colour for each code. The dashed black line represents the relationship for the main sequence at $z \sim 1$ of Elbaz et al. (2007) with its 68% confidence level marked with the grey shaded area. The insets show that as the objects separate from the MS they present shorter young-population ages.

which is also traversed by some galaxies of the sub-mm selected samples (see Fig. 10); although these sets typically present larger stellar masses and SFR s, reflecting their high redshift nature. We should also mention that experiencing short (100–250 Myr) bursts is more common for a massive galaxy at $z \sim 2$ (Rowlands et al. 2014; Lemaux et al. 2014; Dudzevičiūtė et al. 2020).

7.4 Interpreting the position of our dusty starbursts in the $SFR - M_*$ plane

Taking into account the way we selected massive dusty starbursts (see Section 4.2), we should consider the merger scenario of galaxy formation. Local ULIRGs are mostly late-stage mergers, which trigger noteworthy star formation (Sanders & Mirabel 1996; Tacconi et al. 2002). At $L_{\text{TIR}} \geq 10^{11.5-12} L_{\odot}$ and $z \sim 1-2$, a fraction of $\sim 50-70$ per cent of sources selected with *Herschel* shows signatures of mergers/interactions (Kartaltepe et al. 2012; Hung et al. 2013). Half of the $z \sim 2$ *Herschel*-selected (U)LIRGs defined as starbursts ($SFR/SFR_{\text{MS}} > 3$) presents clear merger features (Kartaltepe et al. 2012), with the fraction of such interacting systems increasing with the deviation above the MS (Hung et al. 2013). A careful (varying the cuts) visual inspection of the *Subaru* Suprime-Cam images of our whole sample shows sources in close pairs at similar redshift (see Section 4.2) or tidal (tails, shells, debris) features, asymmetry and multiple nuclei for $\sim 80-90$ per cent of our dusty starbursts. These characteristics are typically originated by interactions.

Off-main sequence galaxies are found at all redshifts, and their

position in the $SFR - M_*$ plane is used to define starburst galaxies. The definition of starburst galaxies –based on SFR offsets from the MS– varies in the literature. Rodighiero et al. (2011) fitted Gaussians to the logarithmic distributions of SFR s at fixed stellar mass of a sample of galaxies with optical-to-FIR observations in the GOODS-S and COSMOS fields. Using these curves, they chose to define starburst galaxies as those sources with SFR more than 4-times that on the MS. According to this definition and using the $z = 1$ Elbaz et al. (2007) MS, 86 and 73 per cent of the sources in our full sample are starbursts from the solutions of the SYNTHESIZER code and the CIGALE. Schreiber et al. (2015) analysed *Herschel* images in several extragalactic fields using individual detections and stacking. With this analysis they defined the MS from $z = 4$ to 0. Such $M_* - SFR$ relation at $z = 1$ is shown in Fig. 10. In their study, starburst galaxies are defined as objects having 5-times larger SFR than the SFR of the MS at the redshift of each galaxy. According to such definition 84 and 60 per cent of the galaxies in our whole sample are starbursts from the results of SYNTHESIZER and CIGALE. Then, more than a half of the dSFGs in our sample satisfies both of the aforementioned starburst definitions.

Cibinel et al. (2019) analysed close pairs and morphological mergers on and above the MS at $0.2 \leq z \leq 2.0$ presenting UV-to-FIR data in the GOODS-N field. They found a merger fraction $\gtrsim 70$ per cent for starburst galaxies identified with the Rodighiero et al. definition. When excluding objects in our full sample with SFR less than 4-times that on the MS, we observe fractions of ~ 60 and ~ 70 per cent of merger-like sources from the CIGALE and the

SYNTHESIZER code solutions. Then, our results are consistent with those on the literature (Kartaltepe et al. 2012; Cibinel et al. 2019).

The merger scenario as the origin of the starburst event is debated. Mancuso et al. (2016) furnished an alternative physical interpretation on the shape and scatter of the MS of star-forming galaxies at $z \gtrsim 1$. In such explanation, young galaxies are located to the left of the MS at a given SFR . As time passes, they will advance at almost constant SFR to their MS position spending most of their life there. Thus, off-main sequence galaxies are depicted as young sources that have to accumulate a large fraction of their stellar mass. An average mass-selected source lies on the MS, while FIR-selected objects are caught on it or above. Thus, the youngest galaxies should be located at the largest distances from the MS.

The Mancuso et al. interpretation is consistent with results from cosmological simulations, which have shown that the bulk of the star formation in galaxies is *in situ*. Martin et al. (2017) found a star-formation fraction of ~ 65 and ~ 80 per cent at $z \sim 3$ and $z \sim 1$ attributable to smooth gas accretion. For galaxies with $M_\star \lesssim 10^{11} M_\odot$, a fraction of ~ 60 – 90 per cent of the star formation occurs *in situ* (Lackner et al. 2012; Pillepich et al. 2018).

In Figure 11, we show the loci of our dusty starbursts in the $SFR - M_\star$ plane, which agrees with the Mancuso et al. scenario due to the SFH we assumed. In the aforementioned Figure (see insets), we notice that the distance to the MS is very well correlated with $t_{\text{you}}^{\text{FIR}}$ ($r_s = -0.88$ and -0.86 with $p_s = 6.1 \times 10^{-38}$ and 1.7×10^{-34} , for SYNTHESIZER and CIGALE, respectively). We corroborate that as galaxies are located far above the MS, they present younger $t_{\text{you}}^{\text{FIR}}$ values, as expected due to our SFH formulation. We distinguish objects with similar SFR differing more than an order of magnitude in stellar mass in Fig. 11, as these objects move to the right approaching the MS, their young-population ages become larger. Thus by definition, a larger SFR value can only be reached with a shorter $t_{\text{you}}^{\text{FIR}}$ value for the same stellar mass. On the other hand, a larger stellar mass value can only be achieved with a larger $t_{\text{you}}^{\text{FIR}}$ value for a constant SFR . Mancuso et al. used a SFH defined by a slow power-law increase of the SFR (which can be approximated by a constant SFR) over a time-scale $\tau_B < 0.5 - 1$ Gyr, followed by an exponential decline due to AGN feedback. Thus, our SFH is similar to theirs in the almost constant part, which can explain the similarity between both results.

Therefore, our findings and our assumed SFH show that the merger and the *in situ* star-formation scenarios are not mutually exclusive. The elevated SFR s of our dusty starbursts are likely triggered by merger events. Then, these starburst galaxies probably continue assembling stellar mass at a roughly constant SFR depending on the available gas supply provided by smooth accretion.

8 SUMMARY AND CONCLUSIONS

We have studied in detail the stellar-population properties of massive ($\log(M_\star/M_\odot) \geq 10$) dusty (FIR-selected) starburst ($SFR/SFR_{\text{MS}} > 2$) galaxies at $0.7 < z < 1.2$ by analysing their UV-to-FIR observed SEDs. The sample is based in at least 2 FIR flux measurements (above the 4σ threshold) from *Spitzer*/MIPS-70 and/or *Herschel*/PACS and SPIRE, and a MIPS-24 detection in the SXDS/UDS field. The multi-wavelength data has been combined by building catalogues in *Subaru*/Suprime-Cam (B , V , R_c , i' and z'), *UKIRT*/WFCAM (J , H and K), *Spitzer*/IRAC (3.6, 4.5, 5.8 and $8.0 \mu\text{m}$) and MIPS (24 and $70 \mu\text{m}$), and *Herschel*/PACS (100 and $160 \mu\text{m}$) and SPIRE (250, 350 and $500 \mu\text{m}$) bands. The full UV-to-FIR SEDs are fitted to stellar population and dust emission

models using codes (SYNTHESIZER and CIGALE) which manage the attenuation of stellar light and dust re-emission with energy balance techniques. We have assumed as fiducial a SFH depicted by a young stellar population forming stars in a roughly constant manner on top on an evolved population each parametrized with and exponentially decaying- τ form. We have compared the best-fitting results obtained with and without FIR information. When using FIR data, their associated L_{TIR} value is used to constrain the amount of stellar-light attenuation (what we call “the FIR prior”). A summary of the main results and conclusions of our work follows:

- Excluding the FIR data in two population models results mainly in an overestimation of the attenuation of the young population, $A_{V,\text{you}}$, with a median value of 0.4 mag. This overestimation translates in underestimating the young-population ages by a factor ~ 6 in median. Both misestimations cause overestimating the SFR s by 0.38 dex (a factor of ~ 2.4) in median. This evidences the efficacy of the “FIR prior” in breaking the age-attenuation degeneracy, in providing reliable attenuation and age values for the young population, and in improving the determinations of the SFHs of massive dusty starburst galaxies.

- The attenuation values of the young population, $A_{V,\text{you}}^{\text{FIR}}$, determined with both codes are compatible and fall in the range $\sim 1.5 - 3.5$ mag, with most of the galaxies (70 per cent) presenting $A_{V,\text{you}}^{\text{FIR}} > 2$ mag. The median difference between codes is < 0.1 mag. The median value is 2.4 mag, which is similar with median values determined for $z > 1$ SMGs. This shows that the energy-balance technique of the 2 different codes produces consistent results.

- The ages of the young population, $t_{\text{you}}^{\text{FIR}}$, are shorter than ~ 400 Myr, with median values of ~ 50 and ~ 120 Myr for SYNTHESIZER and CIGALE. Considering these median values, our fiducial SFH, and that, on average, we are observing our galaxies at half their lifetimes in the starburst phase, we infer a duration of this phase of $\sim 100 - 250$ Myr.

- The determination for the old-population properties are affected by large uncertainties, linked to degenerations and the fact that new stars outshine the old population through most of the SED. The median old-population ages are $\sim 1.5 - 3$ Gyr. The median e -folding times values are ~ 200 and ~ 900 Myr for SYNTHESIZER and CIGALE. These e -folding time differences are compensated with less intense initial burst in CIGALE. The old populations are nearly unattenuated (median $A_{V,\text{old}}^{\text{SYN,FIR}} = 0.1$ mag) as derived from SYNTHESIZER, and present median $A_{V,\text{old}}^{\text{CIG,FIR}} = 0.8$ mag for CIGALE.

- Regarding the stellar masses, both codes yield similar results, with median values of 3.8×10^{10} and $5.2 \times 10^{10} M_\odot$ as derived from SYNTHESIZER and CIGALE. This is expected considering that the codes use the same SFH, IMF and SPS models. These stellar mass values are compatible with those of (U)LIRGs and optical-selected dSFGs at intermediate redshift, and with those of SMGs at $z > 1$.

- Concerning SFR s, the typical SED-derived value is $\sim 200 - 250 M_\odot \text{yr}^{-1}$, which is compatible with those of *Herschel* selected ULIRGs at $0.7 < z < 1.2$ and 1σ lower-limit values of $z > 1$ SMGs. Assuming this typical SFR and the inferred duration of the starburst phase, the stellar mass added during this phase should reach $\sim 2 - 3 \times 10^{10} M_\odot$. This value corresponds to a fraction of $\sim 30 - 50$ per cent of the median stellar mass derived for our sample.

- The position of our dusty starburst galaxies in the $SFR - M_\star$ plane is mainly determined by the young population age. The galaxies located at the largest distances of the MS present younger $t_{\text{you}}^{\text{FIR}}$

values. This is in agreement with previous physical interpretations of the outliers of the $SFR - M_\star$ relation.

ACKNOWLEDGEMENTS

We are grateful with the anonymous referee for improving the manuscript contents. N.E.-B. and J.Z. acknowledge funding support from the Spanish Programa Nacional de Astronomía y Astrofísica under grant AYA2006-02358. N.E.-B. acknowledges support from Fac. CC. Físicas, Universidad Complutense de Madrid (UCM), and from Coordinación de Astrofísica, Instituto Nacional de Astrofísica Óptica y Electrónica (INAOE). P.G.P.-G. acknowledges funding support from the Spanish Government under grant PGC2018-093499-B-I00. L.R.-M. acknowledges support from grant PRIN MIUR 2017-20173ML3WW_001 and funding from the Università degli studi di Padova - Dipartimento di Fisica e Astronomia “G. Galilei”. This work has made use of the RAINBOW Cosmological Surveys Database, which is operated by the Centro de Astrobiología (CAB/CSIC-INTA).

DATA AVAILABILITY

The data underlying this article are available in the article and in its online supplementary material.

REFERENCES

- Akiyama M., et al., 2015, *PASJ*, **67**, 82
 Balog Z., et al., 2014, *Experimental Astronomy*, **37**, 129
 Barro G., et al., 2011a, *ApJS*, **193**, 13
 Barro G., et al., 2011b, *ApJS*, **193**, 30
 Barro G., et al., 2019, *ApJS*, **243**, 22
 Bell E. F., et al., 2005, *ApJ*, **625**, 23
 Bergvall N., Marquart T., Way M. J., Blomqvist A., Holst E., Östlin G., Zackrisson E., 2016, *A&A*, **587**, A72
 Berta S., et al., 2011, *A&A*, **532**, A49
 Bertin E., Arnouts S., 1996, *A&AS*, **117**, 393
 Béthermin M., et al., 2012, *A&A*, **542**, A58
 Bisigello L., Caputi K. I., Grogin N., Koekemoer A., 2018, *A&A*, **609**, A82
 Boogaard L. A., et al., 2019, *ApJ*, **882**, 140
 Borys C., Smail I., Chapman S. C., Blain A. W., Alexander D. M., Ivison R. J., 2005, *ApJ*, **635**, 853
 Bradshaw E. J., et al., 2013, *MNRAS*, **433**, 194
 Brammer G. B., van Dokkum P. G., Coppi P., 2008, *ApJ*, **686**, 1503
 Brisbin D., et al., 2017, *A&A*, **608**, A15
 Bruzual G., Charlot S., 2003, *MNRAS*, **344**, 1000
 Buat V., et al., 2014, *A&A*, **561**, A39
 Buat V., et al., 2015, *A&A*, **577**, A141
 Burgarella D., Buat V., Iglesias-Páramo J., 2005, *MNRAS*, **360**, 1413
 Calzetti D., Armus L., Bohlin R. C., Kinney A. L., Koornneef J., Storchi-Bergmann T., 2000, *ApJ*, **533**, 682
 Casali M., et al., 2007, *A&A*, **467**, 777
 Casey C. M., et al., 2012, *ApJ*, **761**, 140
 Casey C. M., Narayanan D., Cooray A., 2014, *Phys. Rep.*, **541**, 45
 Casey C. M., et al., 2017, *ApJ*, **840**, 101
 Ceverino D., Dekel A., Bouchard F., 2010, *MNRAS*, **404**, 2151
 Chabrier G., 2003, *ApJ*, **586**, L133
 Charlot S., Fall S. M., 2000, *ApJ*, **539**, 718
 Chary R., Elbaz D., 2001, *ApJ*, **556**, 562
 Cibinel A., et al., 2019, *MNRAS*, **485**, 5631
 Ciesla L., Elbaz D., Fensch J., 2017, *A&A*, **608**, A41
 Conroy C., 2013, *ARA&A*, **51**, 393
 Dale D. A., Helou G., 2002, *ApJ*, **576**, 159
 Danielson A. L. R., et al., 2017, *ApJ*, **840**, 78
 De Geyter G., et al., 2015, *MNRAS*, **451**, 1728
 Di Matteo P., Bournaud F., Martig M., Combes F., Melchior A. L., Semelin B., 2008, *A&A*, **492**, 31
 Díaz-García L. A., et al., 2019, *A&A*, **631**, A157
 Donevski D., et al., 2020, *A&A*, **644**, A144
 Donley J. L., et al., 2012, *ApJ*, **748**, 142
 Dowell C. D., et al., 2010, in *Proc. SPIE* Vol. 7731. p. 136, doi:10.1117/12.858035
 Drory N., Alvarez M., 2008, *ApJ*, **680**, 41
 Dudzevičiūtė U., et al., 2020, *MNRAS*, **494**, 3828
 Dunlop J. S., 2011, in Wang W., Lu J., Luo Z., Yang Z., Hua H., Chen Z., eds, *Astronomical Society of the Pacific Conference Series* Vol. 446, *Galaxy Evolution: Infrared to Millimeter Wavelength Perspective*. p. 209
 Dunlop J., et al., 2007, *A Spitzer Public Legacy survey of the UKIDSS Ultra Deep Survey*, *Spitzer Proposal*
 Dye S., et al., 2008, *MNRAS*, **386**, 1107
 Elbaz D., et al., 2007, *A&A*, **468**, 33
 Elbaz D., et al., 2011, *A&A*, **533**, A119
 Frayer D. T., et al., 2006, *ApJ*, **647**, L9
 Frayer D. T., et al., 2009, *AJ*, **138**, 1261
 Furusawa H., et al., 2008, *ApJS*, **176**, 1
 Gawiser E., et al., 2007, *ApJ*, **671**, 278
 Geach J. E., Simpson C., Rawlings S., Read A. M., Watson M., 2007, *MNRAS*, **381**, 1369
 Genzel R., et al., 2010, *MNRAS*, **407**, 2091
 Giovannoli E., Buat V., Noll S., Burgarella D., Magnelli B., 2011, *A&A*, **525**, A150
 Gómez-Guijarro C., et al., 2018, *ApJ*, **856**, 121
 Griffin M. J., et al., 2010, *A&A*, **518**, L3
 Gruppioni C., et al., 2013, *MNRAS*, **432**, 23
 Hainline L. J., Blain A. W., Smail I., Alexander D. M., Armus L., Chapman S. C., Ivison R. J., 2011, *ApJ*, **740**, 96
 Hickox R. C., et al., 2012, *MNRAS*, **421**, 284
 Huang J. S., et al., 2004, *ApJS*, **154**, 44
 Hung C.-L., et al., 2013, *ApJ*, **778**, 129
 Hunt L. K., et al., 2019, *A&A*, **621**, A51
 Ilbert O., et al., 2006, *A&A*, **457**, 841
 Kartaltepe J. S., et al., 2012, *ApJ*, **757**, 23
 Kennicutt Robert C. J., 1998, *ARA&A*, **36**, 189
 Kurczynski P., et al., 2016, *ApJ*, **820**, L1
 Lacey C. G., et al., 2016, *MNRAS*, **462**, 3854
 Lackner C. N., Cen R., Ostriker J. P., Joung M. R., 2012, *MNRAS*, **425**, 641
 Lawrence A., et al., 2007, *MNRAS*, **379**, 1599
 Le Floch E., et al., 2005, *ApJ*, **632**, 169
 Lee S.-K., Idzi R., Ferguson H. C., Somerville R. S., Wiklind T., Giavalisco M., 2009, *ApJS*, **184**, 100
 Lee N., et al., 2013, *ApJ*, **778**, 131
 Lemaux B. C., et al., 2014, *A&A*, **572**, A90
 Magnelli B., et al., 2013, *A&A*, **553**, A132
 Makovoz D., Khan I., 2005, in Shopbell P., Britton M., Ebert R., eds, *Astron. Soc. Pac. Conference Series* Vol. 347, *Astronomical Data Analysis Software and Systems XIV*. p. 81
 Malek K., et al., 2017, *A&A*, **598**, A1
 Mancuso C., Lapi A., Shi J., Cai Z. Y., Gonzalez-Nuevo J., Béthermin M., Danese L., 2016, *ApJ*, **833**, 152
 Maraston C., 2005, *MNRAS*, **362**, 799
 Maraston C., Pforr J., Renzini A., Daddi E., Dickinson M., Cimatti A., Tonini C., 2010, *MNRAS*, **407**, 830
 Marchesini D., van Dokkum P. G., Förster Schreiber N. M., Franx M., Labbé I., Wuyts S., 2009, *ApJ*, **701**, 1765
 Martin D. C., et al., 2005, *ApJ*, **619**, L1
 Martin G., Kaviraj S., Devriendt J. E. G., Dubois Y., Laigle C., Pichon C., 2017, *MNRAS*, **472**, L50
 Martis N. S., et al., 2016, *ApJ*, **827**, L25
 McLure R. J., et al., 2013, *MNRAS*, **428**, 1088
 Melbourne J., et al., 2008, *AJ*, **135**, 1207

- Michałowski M. J., Hayward C. C., Dunlop J. S., Bruce V. A., Cirasuolo M., Cullen F., Hernquist L., 2014, *A&A*, **571**, A75
- Miettinen O., et al., 2017, *A&A*, **606**, A17
- Miyazaki S., et al., 2002, *PASJ*, **54**, 833
- Muzzin A., Marchesini D., van Dokkum P. G., Labbé I., Kriek M., Franx M., 2009, *ApJ*, **701**, 1839
- Nguyen H. T., et al., 2010, *A&A*, **518**, L5
- Noeske K. G., et al., 2007, *ApJ*, **660**, L43
- Noll S., Burgarella D., Giovannoli E., Buat V., Marcellac D., Muñoz-Mateos J. C., 2009, *A&A*, **507**, 1793
- O’Connell R. W., 1986, in Norman C. A., Renzini A., Tosi M., eds, *Stellar Populations*. p. 167
- Oliver S. J., et al., 2010, *A&A*, **518**, L21
- Oliver S. J., et al., 2012, *MNRAS*, **424**, 1614
- Papovich C., et al., 2004, *ApJS*, **154**, 70
- Pérez-González P. G., Gil de Paz A., Zamorano J., Gallego J., Alonso-Herrero A., Aragón-Salamanca A., 2003, *MNRAS*, **338**, 525
- Pérez-González P. G., et al., 2005, *ApJ*, **630**, 82
- Pérez-González P. G., et al., 2008, *ApJ*, **675**, 234
- Pérez-González P. G., et al., 2010, *A&A*, **518**, L15
- Pérez-González P. G., et al., 2013, *ApJ*, **762**, 46
- Pforr J., Maraston C., Tonini C., 2012, *MNRAS*, **422**, 3285
- Pilbratt G. L., et al., 2010, *A&A*, **518**, L1
- Pillepich A., et al., 2018, *MNRAS*, **475**, 648
- Poglitsch A., et al., 2010, *A&A*, **518**, L2
- Popesso P., et al., 2012, arXiv e-prints, p. arXiv:1211.4257
- Rawle T. D., et al., 2016, *MNRAS*, **459**, 1626
- Renzini A., 2009, *MNRAS*, **398**, L58
- Rieke G. H., Alonso-Herrero A., Weiner B. J., Pérez-González P. G., Blaylock M., Donley J. L., Marcellac D., 2009, *ApJ*, **692**, 556
- Rodighiero G., et al., 2011, *ApJ*, **739**, L40
- Rodríguez-Muñoz L., et al., 2019, *MNRAS*, **485**, 586
- Romeo A. B., Fathi K., 2016, *MNRAS*, **460**, 2360
- Roseboom I. G., et al., 2010, *MNRAS*, **409**, 48
- Rowlands K., et al., 2014, *MNRAS*, **441**, 1017
- Rujopakarn W., Rieke G. H., Weiner B. J., Pérez-González P., Rex M., Walth G. L., Kartaltepe J. S., 2013, *ApJ*, **767**, 73
- Salim S., et al., 2007, *ApJS*, **173**, 267
- Salimbeni S., Fontana A., Giallongo E., Grazian A., Menci N., Pentericci L., Santini P., 2009, in Giobbi G., Tornambe A., Raimondo G., Limongi M., Antonelli L. A., Menci N., Brocato E., eds, *American Institute of Physics Conference Series Vol. 1111, Probing Stellar Populations Out to the Distant Universe: Cefalu 2008, Proceedings of the International Conference*. pp 207–211 (arXiv:0901.3540), doi:10.1063/1.3141545
- Salmon B., et al., 2016, *ApJ*, **827**, 20
- Salpeter E. E., 1955, *ApJ*, **121**, 161
- Sanders D. B., Mirabel I. F., 1996, *ARA&A*, **34**, 749
- Schreiber C., et al., 2015, *A&A*, **575**, A74
- Smail I., Sharp R., Swinbank A. M., Akiyama M., Ueda Y., Foucaud S., Almaini O., Croom S., 2008, *MNRAS*, **389**, 407
- Smith A. J., et al., 2012, *MNRAS*, **419**, 377
- Swinbank A. M., Smail I., Chapman S. C., Blain A. W., Ivison R. J., Keel W. C., 2004, *ApJ*, **617**, 64
- Swinbank A. M., Chapman S. C., Smail I., Lindner C., Borys C., Blain A. W., Ivison R. J., Lewis G. F., 2006, *MNRAS*, **371**, 465
- Swinbank A. M., et al., 2014, *MNRAS*, **438**, 1267
- Tacconi L. J., Genzel R., Lutz D., Rigopoulou D., Baker A. J., Iserlohe C., Tecza M., 2002, *ApJ*, **580**, 73
- Tacconi L. J., et al., 2008, *ApJ*, **680**, 246
- Takagi T., Arimoto N., Vansevičius V., 1999, *ApJ*, **523**, 107
- Tonini C., Maraston C., Devriendt J., Thomas D., Silk J., 2009, *MNRAS*, **396**, L36
- Wardlow J. L., et al., 2017, *ApJ*, **837**, 12
- Whitaker K. E., Pope A., Cybulski R., Casey C. M., Popping G., Yun M. S., 2017, *ApJ*, **850**, 208
- Wieprecht E., et al., 2009, in Bohlender D. A., Durand D., Dowler P., eds, *Astron. Soc. Pac. Conference Series Vol. 411, Astronomical Data Analysis Software and Systems XVIII*. p. 531
- Zibetti S., Gallazzi A., Charlot S., Pierini D., Pasquali A., 2013, *MNRAS*, **428**, 1479
- da Cunha E., Charlot S., Elbaz D., 2008, *MNRAS*, **388**, 1595
- da Cunha E., et al., 2015, *ApJ*, **806**, 110
- van Breukelen C., et al., 2007, *MNRAS*, **382**, 971

This paper has been typeset from a \LaTeX file prepared by the author.

Table 2: Dusty-starburst main-sample multi-band photometry. (1) Name of the galaxy. (2,3) Right ascension and declination (J2000) in degrees. (4) Photometric or spectroscopic redshift (z_{spec} indicated by a \dagger). (33-39) Flux densities in MIPS 24, 70; PACS 100, 160; SPIRE 250, 350, 500 in mJy. (5-11,19-25) Observed magnitude in FUV, NUV; B , V , R_c , i' , z' ; J , H , K ; IRAC 3.6-8.0 in the AB photometric system. (40-46) Associated uncertainties to MIPS 24, 70; PACS 100, 160; SPIRE 250, 350, 500 in mJy determined as described in Sections 2.1 and 2.2. (12-18,26-32) Associated uncertainties to FUV, NUV; B , V , R_c , i' , z' ; J , H , K ; IRAC 3.6-8.0 as obtained from the aperture matched cataloguing (see Section 3.2). “...” indicate bands without detections or without reliable photometric measurements.

Galaxy	α	δ	z^\dagger	FUV ΔFUV J ΔJ S_{24} ΔS_{24} (5) (12) (19) (26) (33) (40)	NUV ΔNUV H ΔH S_{70} ΔS_{70} (6) (13) (20) (27) (34) (41)	B ΔB K ΔK S_{100} ΔS_{100} (7) (14) (21) (28) (35) (42)	V ΔV [3.6] Δ [3.6] S_{160} ΔS_{160} (8) (15) (22) (29) (36) (43)	R_c ΔR_c [4.5] Δ [4.5] S_{250} ΔS_{250} (9) (16) (23) (30) (37) (44)	i' $\Delta i'$ [5.8] Δ [5.8] S_{350} ΔS_{350} (10) (17) (24) (31) (38) (45)	z' $\Delta z'$ [8.0] Δ [8.0] S_{500} ΔS_{500} (11) (18) (25) (32) (39) (46)
(1)	(2)	(3)	(4)							
MIPS0000517A	34.519727	−5.057373	1.0500	24.09	23.68	23.41	22.95	22.47
				0.01	0.01	0.01	0.01	0.01
				21.85	21.73	21.16	20.50	20.55	20.67	20.51
				0.02	0.03	0.01	0.05	0.05	0.07	0.08
				0.23	...	11.03	14.86
				0.02	...	0.96	1.89
MIPS0000648A	34.586462	−5.201155	1.1900	24.48	24.19	23.70	23.13	22.33
				0.02	0.02	0.01	0.01	0.01
				21.80	21.35	20.71	20.08	20.05	20.26	20.21
				0.02	0.02	0.01	0.04	0.04	0.05	0.06
				0.20	...	8.67	23.02	26.21	16.33	...
				0.02	...	0.69	1.84	2.41	3.33	...
MIPS0000816_1	34.313226	−5.554958	0.9300	...	22.68	22.47	22.21	22.09	21.74	21.56
				...	0.08	0.01	0.01	0.01	0.01	0.01
				21.02	21.22	20.97	20.57	20.83	20.81	20.62
				0.03	0.08	0.04	0.04	0.04	0.05	0.07
				0.45	23.13	23.10	13.28	...
				0.01	2.61	3.00	3.19	...
MIPS0000826	34.894621	−5.300254	0.7200	24.21	23.29	22.33	21.62	21.28
				0.02	0.01	0.01	0.01	0.01
				20.71	20.24	19.70	19.30	19.62	19.38	18.86
				0.01	0.02	0.01	0.04	0.04	0.04	0.05
				2.09	66.27	90.70	105.05	65.59
				0.04	2.92	7.08	8.40	4.39
MIPS0001713	34.375389	−4.760178	1.1100	24.34	23.99	23.61	22.98	22.27
				0.01	0.01	0.01	0.01	0.01
				21.61	21.25	20.73	20.16	20.30	20.84	20.91
				0.01	0.02	0.01	0.04	0.04	0.07	0.09
				0.15	13.49	11.90
				0.01	1.84	3.04
MIPS0002196_1	34.474978	−5.038923	1.0980 †	26.05	25.37	24.65	23.66	22.84
				0.05	0.04	0.03	0.02	0.01
				21.95	21.35	20.58	19.85	19.87	20.12	19.64
				0.02	0.02	0.01	0.03	0.03	0.04	0.06
				0.67	...	15.20	26.28	28.00	18.68	...
				0.02	...	1.25	2.26	2.60	3.53	...

Continued in the next page

Table2 – continued from previous page

Galaxy	α	δ	z^\dagger	FUV ΔFUV J ΔJ S_{24} ΔS_{24} (5) (12) (19) (26) (33) (40)	NUV ΔNUV H ΔH S_{70} ΔS_{70} (6) (13) (20) (27) (34) (41)	B ΔB K ΔK S_{100} ΔS_{100} (7) (14) (21) (28) (35) (42)	V ΔV $[3.6]$ $\Delta[3.6]$ S_{160} ΔS_{160} (8) (15) (22) (29) (36) (43)	R_c ΔR_c $[4.5]$ $\Delta[4.5]$ S_{250} ΔS_{250} (9) (16) (23) (30) (37) (44)	i' $\Delta i'$ $[5.8]$ $\Delta[5.8]$ S_{350} ΔS_{350} (10) (17) (24) (31) (38) (45)	z' $\Delta z'$ $[8.0]$ $\Delta[8.0]$ S_{500} ΔS_{500} (11) (18) (25) (32) (39) (46)
MIPS0002371A	34.492554	-5.141918	1.1800	23.77	23.53	23.04	...
				0.02	0.02	0.01	...
				21.80	21.38	20.84	20.24	20.29	20.42	20.19
				0.02	0.02	0.01	0.05	0.04	0.07	0.06
				0.11	...	4.34	11.08	13.87
				0.01	...	0.38	1.01	1.89
MIPS0002397A	34.188614	-5.300839	0.8020 [†]	23.12	22.46	21.80	21.16	20.70
				0.01	0.01	0.01	0.01	0.01
				20.02	19.70	19.21	18.99	19.29	19.28	19.24
				0.01	0.01	0.01	0.04	0.04	0.04	0.04
				0.75	13.47	29.55	42.66	40.22	19.85	...
				0.02	1.60	2.31	3.41	3.06	4.27	...
MIPS0002670A	34.534498	-5.340577	0.9300	...	22.74	22.23	21.95	21.87	21.38	21.19
				...	0.06	0.01	0.01	0.01	0.01	0.01
				20.73	20.65	20.18	19.80	20.01	19.85	19.04
				0.01	0.02	0.01	0.24	0.33	0.43	0.09
				0.61	13.38	26.68	...	16.91
				0.02	1.73	2.11	...	2.64
MIPS0004202_1	34.547213	-4.866452	1.1000	24.13	23.65	23.44	22.89	22.42
				0.01	0.01	0.01	0.01	0.01
				21.73	21.20	20.61	19.86	19.80	20.49	20.17
				0.02	0.01	0.01	0.03	0.03	0.04	0.06
				0.30	23.09	39.74	25.50	...
				0.01	2.63	3.34	3.90	...
MIPS0004442A	34.484616	-5.106900	1.0700	23.95	23.54	23.23	22.66	22.09
				0.01	0.01	0.01	0.01	0.01
				21.51	21.18	20.63	20.23	20.35	20.85	20.50
				0.02	0.02	0.01	0.05	0.04	0.08	0.07
				0.20	...	8.79	...	18.30
				0.02	...	0.73	...	2.84
MIPS0004467	34.122342	-5.296071	1.1100	24.25	23.79	23.55	23.07	22.62
				0.02	0.02	0.02	0.01	0.01
				22.11	21.76	21.17	20.47	20.43	20.72	20.34
				0.02	0.03	0.01	0.05	0.04	0.07	0.06
				0.28	...	9.79	...	17.65
				0.02	...	1.29	...	1.77
MIPS0004558A	34.831818	-5.041486	0.8800	22.73	22.09	21.66	20.87	20.45
				0.01	0.01	0.01	0.01	0.01
				19.82	19.55	19.11	18.83	19.06	19.30	19.26
				0.01	0.01	0.01	0.04	0.04	0.04	0.04
				0.96	...	17.57	35.40	40.14	22.75	...
				0.02	...	1.63	3.79	3.49	3.50	...

Continued in the next page

Table2 – continued from previous page

Galaxy	α	δ	z^\dagger	FUV ΔFUV J ΔJ S_{24} ΔS_{24} (5) (12) (19) (26) (33) (40)	NUV ΔNUV H ΔH S_{70} ΔS_{70} (6) (13) (20) (27) (34) (41)	B ΔB K ΔK S_{100} ΔS_{100} (7) (14) (21) (28) (35) (42)	V ΔV $[3.6]$ $\Delta[3.6]$ S_{160} ΔS_{160} (8) (15) (22) (29) (36) (43)	R_c ΔR_c $[4.5]$ $\Delta[4.5]$ S_{250} ΔS_{250} (9) (16) (23) (30) (37) (44)	i' $\Delta i'$ $[5.8]$ $\Delta[5.8]$ S_{350} ΔS_{350} (10) (17) (24) (31) (38) (45)	z' $\Delta z'$ $[8.0]$ $\Delta[8.0]$ S_{500} ΔS_{500} (11) (18) (25) (32) (39) (46)
MIPS0007062A	34.292232	-4.743812	1.1100	24.05	23.60	23.29	22.64	22.04
				0.01	0.01	0.01	0.01	0.01
				21.64	21.38	20.89	20.35	20.49	20.83	20.31
				0.02	0.02	0.01	0.05	0.04	0.10	0.06
				0.22	...	10.79	25.50	...	15.17	...
				0.01	...	1.32	2.65	...	3.60	...
MIPS0007112_1	34.008277	-4.883635	1.0200	25.00	24.47	24.11	23.41	22.92
				0.01	0.01	0.01	0.01	0.01
				22.16	21.79	21.16	20.40	20.59	21.01	20.69
				0.02	0.03	0.02	0.04	0.03	0.05	0.06
				0.25	...	7.61	18.27	19.97
				0.02	...	0.91	3.38	2.48
MIPS0007300_1	34.611832	-4.643831	1.1500	23.88	23.57	23.35	22.93	22.28
				0.01	0.01	0.01	0.01	0.01
				22.12	21.43	21.21	20.49	20.57	20.82	20.40
				0.11	0.08	0.06	0.04	0.03	0.05	0.06
				0.22	...	14.41	34.50	20.97
				0.01	...	1.36	3.17	3.82
MIPS0007352_1	34.413533	-4.745065	1.1200	24.91	24.54	24.14	23.45	22.81
				0.02	0.02	0.02	0.01	0.01
				22.38	21.93	21.46	20.66	20.70	20.74	20.26
				0.02	0.03	0.02	0.04	0.03	0.04	0.06
				0.32	8.37	17.65	14.62
				0.02	2.03	1.54	2.34
MIPS0007356A	34.191957	-4.848087	1.1300	25.52	24.19	23.38	22.38
				0.10	0.03	0.02	0.02
				21.47	21.05	20.48	20.07	20.20	20.49	20.42
				0.02	0.02	0.01	0.12	0.14	0.11	0.08
				0.12	17.79	21.52
				0.01	2.15	2.09
MIPS0007593_1	34.553306	-4.725986	1.1000	24.59	24.02	23.67	23.05	22.57
				0.05	0.03	0.03	0.02	0.02
				21.81	21.31	20.58	19.81	19.99	20.41	19.87
				0.02	0.02	0.01	0.03	0.03	0.04	0.06
				0.36	19.20	18.08
				0.01	2.36	3.16
MIPS0007658_1	34.393268	-4.810692	1.0800	23.74	23.30	22.97	22.52	22.01
				0.01	0.01	0.01	0.01	0.01
				21.53	21.14	20.64	20.21	20.29	20.61	20.38
				0.02	0.02	0.01	0.04	0.03	0.04	0.06
				0.33	16.66	18.52
				0.02	2.47	2.46

Continued in the next page

Table2 – continued from previous page

Galaxy	α	δ	z^\dagger	FUV ΔFUV J ΔJ S_{24} ΔS_{24} (5) (12) (19) (26) (33) (40)	NUV ΔNUV H ΔH S_{70} ΔS_{70} (6) (13) (20) (27) (34) (41)	B ΔB K ΔK S_{100} ΔS_{100} (7) (14) (21) (28) (35) (42)	V ΔV $[3.6]$ $\Delta[3.6]$ S_{160} ΔS_{160} (8) (15) (22) (29) (36) (43)	R_c ΔR_c $[4.5]$ $\Delta[4.5]$ S_{250} ΔS_{250} (9) (16) (23) (30) (37) (44)	i' $\Delta i'$ $[5.8]$ $\Delta[5.8]$ S_{350} ΔS_{350} (10) (17) (24) (31) (38) (45)	z' $\Delta z'$ $[8.0]$ $\Delta[8.0]$ S_{500} ΔS_{500} (11) (18) (25) (32) (39) (46)
MIPS0008171	34.216338	−4.985269	1.1000	25.13	24.20	23.47	22.68	21.88
				0.02	0.02	0.01	0.01	0.01
				21.03	20.51	19.91	19.35	19.48	19.70	19.60
				0.01	0.01	0.01	0.04	0.04	0.04	0.05
				0.56	...	8.28	25.16	28.63	19.01	...
				0.02	...	0.89	2.16	2.38	2.87	...
MIPS0008331	34.466319	−4.897633	1.1300	23.55	23.06	22.78	22.30	21.73
				0.01	0.01	0.01	0.01	0.01
				21.17	20.80	20.28	19.76	19.83	20.04	19.70
				0.01	0.01	0.01	0.04	0.04	0.04	0.05
				0.41	17.64	20.12
				0.01	2.01	3.00
MIPS0008368A	34.315691	−4.973181	0.8600	24.81	23.89	23.16	22.27	21.80
				0.02	0.01	0.01	0.01	0.01
				20.86	20.44	19.86	19.54	19.81	19.73	19.79
				0.01	0.01	0.01	0.04	0.04	0.04	0.06
				0.68	11.54	20.50	33.76	31.83	14.47	...
				0.02	2.30	1.64	2.77	2.64	3.08	...
MIPS0008471A	34.341859	−4.981434	1.0960 [†]	24.73	24.00	23.28	22.35	21.49
				0.02	0.01	0.01	0.01	0.01
				20.71	20.29	19.78	19.30	19.38	19.62	19.59
				0.01	0.01	0.01	0.04	0.04	0.04	0.05
				0.27	...	29.18	54.10	52.97	33.52	...
				0.01	...	2.28	4.27	3.55	3.55	...
MIPS0008576_1	34.099917	−5.111324	1.1000	25.47	24.66	23.96	23.12	22.39
				0.02	0.01	0.01	0.01	0.01
				21.69	21.21	20.57	19.75	19.85	20.38	20.56
				0.01	0.01	0.01	0.03	0.03	0.04	0.06
				0.25	...	16.26	31.32	29.05
				0.02	...	1.45	2.98	2.96
MIPS0008647	34.153409	−5.098265	0.8052 [†]	22.08	21.64	21.23	20.69	20.48
				0.01	0.01	0.01	0.01	0.01
				19.96	19.75	19.38	19.14	19.45	19.29	19.25
				0.01	0.01	0.01	0.04	0.04	0.04	0.04
				1.05	19.15	39.83	56.86	50.49	29.30	...
				0.02	1.72	3.23	4.55	3.79	3.87	...
MIPS0008710A	34.604599	−4.905550	1.0500	23.10	22.53	22.08	21.54	20.91
				0.01	0.01	0.01	0.01	0.01
				20.32	19.92	19.45	19.16	19.14	19.58	19.40
				0.01	0.01	0.01	0.02	0.02	0.03	0.03
				0.67	...	12.14	23.31	39.09	29.06	...
				0.02	...	1.14	2.33	3.28	4.10	...

Continued in the next page

Table2 – continued from previous page

Galaxy	α	δ	z^\dagger	FUV ΔFUV J ΔJ S_{24} ΔS_{24} (5) (12) (19) (26) (33) (40)	NUV ΔNUV H ΔH S_{70} ΔS_{70} (6) (13) (20) (27) (34) (41)	B ΔB K ΔK S_{100} ΔS_{100} (7) (14) (21) (28) (35) (42)	V ΔV $[3.6]$ $\Delta[3.6]$ S_{160} ΔS_{160} (8) (15) (22) (29) (36) (43)	R_c ΔR_c $[4.5]$ $\Delta[4.5]$ S_{250} ΔS_{250} (9) (16) (23) (30) (37) (44)	i' $\Delta i'$ $[5.8]$ $\Delta[5.8]$ S_{350} ΔS_{350} (10) (17) (24) (31) (38) (45)	z' $\Delta z'$ $[8.0]$ $\Delta[8.0]$ S_{500} ΔS_{500} (11) (18) (25) (32) (39) (46)
MIPS0008752A	34.114364	−5.138740	0.9500	24.97	24.20	23.66	22.69	22.14
				0.02	0.02	0.01	0.01	0.01
				21.29	20.95	20.31	19.84	19.97	20.16	19.85
				0.01	0.02	0.01	0.04	0.04	0.06	0.06
				0.56	...	27.77	30.58
				0.02	...	2.36	2.78
MIPS0008856	34.484628	−4.986507	0.8770 [†]	25.35	24.38	23.65	22.72	22.26
				0.03	0.02	0.01	0.01	0.01
				21.40	21.03	20.41	19.84	20.01	20.22	20.02
				0.01	0.01	0.01	0.04	0.04	0.05	0.05
				0.37	...	9.71	24.91	22.99
				0.02	...	1.01	2.24	3.10
MIPS0008916	34.739449	−4.881160	1.0400	25.91	25.26	24.87	23.91	23.27
				0.06	0.05	0.04	0.02	0.02
				22.53	22.12	21.54	20.87	21.05	21.40	21.20
				0.02	0.03	0.01	0.05	0.05	0.11	0.13
				0.09	...	7.05	...	12.51
				0.01	...	0.88	...	2.04
MIPS0008918_1	34.825240	−4.841727	0.9500	24.86	24.06	23.52	22.65	22.06
				0.02	0.01	0.01	0.01	0.01
				21.08	20.71	20.03	19.45	19.57	19.83	19.69
				0.01	0.01	0.01	0.03	0.03	0.04	0.06
				0.64	...	12.97	28.56	25.92
				0.02	...	1.57	3.31	2.95
MIPS0009017	34.112593	−5.190671	1.1000	24.64	24.27	23.85	23.13	22.55
				0.13	0.04	0.03	0.02	0.02
				21.49	20.98	20.36	19.73	19.95	20.00	19.97
				0.01	0.02	0.01	0.04	0.04	0.06	0.06
				0.35	7.74	...	19.03
				0.01	1.74	...	3.37
MIPS0009335A	34.270485	−5.174521	1.1100	25.19	24.44	24.09	23.31	22.53
				0.03	0.02	0.02	0.01	0.01
				22.08	21.63	21.05	20.39	20.47	20.59	20.60
				0.02	0.03	0.01	0.05	0.04	0.06	0.10
				0.15	...	6.29	16.39	19.21
				0.02	...	0.53	1.38	2.31
MIPS0009527_1	34.194651	−5.242778	1.1900	26.94	25.59	24.96	23.92	23.05
				0.07	0.04	0.03	0.01	0.01
				22.10	21.45	20.67	19.87	20.08	20.56	20.37
				0.02	0.02	0.01	0.03	0.03	0.05	0.07
				0.26	...	10.02	17.48
				0.01	...	0.82	1.66

Continued in the next page

Table2 – continued from previous page

Galaxy	α	δ	z^{\dagger}	FUV ΔFUV J ΔJ S_{24} ΔS_{24} (5) (12) (19) (26) (33) (40)	NUV ΔNUV H ΔH S_{70} ΔS_{70} (6) (13) (20) (27) (34) (41)	B ΔB K ΔK S_{100} ΔS_{100} (7) (14) (21) (28) (35) (42)	V ΔV $[3.6]$ $\Delta[3.6]$ S_{160} ΔS_{160} (8) (15) (22) (29) (36) (43)	R_c ΔR_c $[4.5]$ $\Delta[4.5]$ S_{250} ΔS_{250} (9) (16) (23) (30) (37) (44)	i' $\Delta i'$ $[5.8]$ $\Delta[5.8]$ S_{350} ΔS_{350} (10) (17) (24) (31) (38) (45)	z' $\Delta z'$ $[8.0]$ $\Delta[8.0]$ S_{500} ΔS_{500} (11) (18) (25) (32) (39) (46)
MIPS0009550_1	34.636966	−5.045595	1.1100	25.87	24.79	24.00	23.13	22.30
				0.02	0.01	0.01	0.01	0.01
				21.37	20.78	20.12	19.46	19.60	20.10	19.85
				0.01	0.01	0.01	0.03	0.03	0.04	0.06
				0.43	...	13.26	27.67	33.30	19.74	...
				0.02	...	1.25	2.52	3.16	3.34	...
MIPS0010952A	34.854405	−5.209882	0.8850 [†]	23.54	22.75	22.23	21.42	20.96
				0.01	0.01	0.01	0.01	0.01
				20.24	19.89	19.33	18.84	19.06	19.17	19.09
				0.01	0.01	0.01	0.04	0.04	0.04	0.04
				1.24	16.19	51.29	97.85	96.47	57.62	22.91
				0.03	1.96	4.00	7.73	6.17	5.24	3.62
MIPS0011090A	34.652685	−5.328335	0.9000	22.46	21.99	21.72	21.12	20.70
				0.01	0.01	0.01	0.01	0.01
				19.98	19.75	19.25	18.91	19.16	19.22	19.06
				0.01	0.01	0.01	0.04	0.04	0.04	0.04
				1.17	10.46	22.01	42.50	42.50	26.63	...
				0.03	1.52	1.80	3.53	3.36	3.54	...
MIPS0011318_1	34.432285	−5.469208	1.0900	24.17	23.57	23.21	22.44	21.94
				0.01	0.01	0.01	0.01	0.01
				21.31	20.94	20.28	19.52	19.58	19.76	19.53
				0.01	0.02	0.01	0.03	0.03	0.04	0.06
				0.59	9.34	13.28
				0.02	1.99	1.38
MIPS0011415A	34.589783	−5.409661	0.9700	24.28	23.68	23.32	22.59	22.14
				0.01	0.01	0.01	0.01	0.01
				21.48	21.20	20.66	19.98	20.12	20.37	20.22
				0.02	0.02	0.01	0.04	0.04	0.05	0.07
				0.29	...	18.29	37.63	27.47
				0.01	...	1.52	3.12	2.80
MIPS0011497	34.666872	−5.390655	1.1000	25.57	24.63	23.88	22.85	22.26
				0.04	0.03	0.02	0.01	0.01
				21.31	20.77	19.99	19.21	19.39	19.36	19.57
				0.01	0.02	0.01	0.04	0.04	0.04	0.05
				0.48	16.70	20.14
				0.01	1.87	2.46
MIPS0015031A	34.580987	−4.803202	1.1400	24.87	24.14	23.28	22.35	21.40
				0.02	0.01	0.01	0.01	0.01
				20.58	20.11	19.52	18.85	18.91	19.35	19.10
				0.01	0.01	0.01	0.04	0.04	0.04	0.04
				0.49	...	14.86	33.77	39.59	30.69	...
				0.01	...	1.34	3.24	3.29	4.14	...

Continued in the next page

Table2 – continued from previous page

Galaxy	α	δ	z^\dagger	FUV ΔFUV J ΔJ S_{24} ΔS_{24} (5) (12) (19) (26) (33) (40)	NUV ΔNUV H ΔH S_{70} ΔS_{70} (6) (13) (20) (27) (34) (41)	B ΔB K ΔK S_{100} ΔS_{100} (7) (14) (21) (28) (35) (42)	V ΔV $[3.6]$ $\Delta[3.6]$ S_{160} ΔS_{160} (8) (15) (22) (29) (36) (43)	R_c ΔR_c $[4.5]$ $\Delta[4.5]$ S_{250} ΔS_{250} (9) (16) (23) (30) (37) (44)	i' $\Delta i'$ $[5.8]$ $\Delta[5.8]$ S_{350} ΔS_{350} (10) (17) (24) (31) (38) (45)	z' $\Delta z'$ $[8.0]$ $\Delta[8.0]$ S_{500} ΔS_{500} (11) (18) (25) (32) (39) (46)
MIPS0015211A	34.786156	-4.779074	0.8700	23.17	22.53	21.98	21.24	20.69
				0.01	0.01	0.01	0.01	0.01
				19.91	19.52	19.14	18.76	18.93	18.92	19.11
				0.01	0.01	0.01	0.04	0.04	0.03	0.04
				0.93	...	14.13	31.46	46.65	35.39	...
				0.02	...	1.30	3.27	4.15	3.82	...
MIPS0015678_1	34.626990	-5.037358	1.1100	25.08	24.47	24.14	23.52	23.00
				0.02	0.01	0.02	0.01	0.01
				22.41	22.02	21.39	20.61	20.79	21.11	20.89
				0.02	0.03	0.01	0.04	0.03	0.05	0.06
				0.22	12.58	19.36	17.77
				0.01	1.87	1.57	2.17
MIPS0015694A	34.410749	-5.141795	1.1900	23.28	23.07	22.94	22.70	22.20
				0.01	0.01	0.01	0.01	0.01
				21.95	21.49	21.21	20.59	20.48	20.90	19.62
				0.02	0.03	0.02	0.05	0.04	0.10	0.05
				0.15	21.54	37.62	41.97	30.09
				0.01	1.66	2.90	3.27	2.77
MIPS0015703	34.342917	-5.177274	1.0900	25.84	24.82	23.79	22.69	21.70
				0.06	0.02	0.02	0.01	0.01
				20.77	20.25	19.62	19.09	19.17	19.32	18.89
				0.01	0.01	0.01	0.04	0.04	0.04	0.04
				0.46	...	12.95	28.56	30.90
				0.02	...	1.01	2.26	2.72
MIPS0015828_1	34.705186	-5.061754	0.9617 [†]	24.76	23.89	23.28	22.35	21.73
				0.01	0.01	0.01	0.01	0.01
				20.72	20.39	19.74	19.13	19.35	19.55	19.74
				0.01	0.01	0.01	0.03	0.03	0.04	0.06
				0.83	8.59	17.85	31.96	40.89	24.11	...
				0.02	1.53	1.54	3.13	3.15	3.62	...
MIPS0016374	34.583684	-5.365429	0.8200	24.87	23.71	22.83	21.80	21.31
				0.02	0.01	0.01	0.01	0.01
				20.46	19.91	19.32	18.82	19.15	19.13	19.31
				0.01	0.01	0.01	0.04	0.04	0.04	0.04
				0.92	21.05	51.03	92.98	79.66	45.14	...
				0.02	1.62	3.93	7.25	5.34	3.93	...
MIPS0016401A	34.885406	-5.237181	0.9200	25.69	24.70	24.11	23.16	22.53
				0.03	0.02	0.01	0.01	0.01
				21.92	21.61	20.97	20.04	19.86	20.05	18.91
				0.02	0.03	0.01	0.04	0.04	0.05	0.04
				0.32	...	18.91	37.86	32.87	17.79	...
				0.02	...	1.72	3.75	2.96	3.75	...

Continued in the next page

Table2 – continued from previous page

Galaxy	α	δ	z^\dagger	FUV ΔFUV J ΔJ S_{24} ΔS_{24} (5) (12) (19) (26) (33) (40)	NUV ΔNUV H ΔH S_{70} ΔS_{70} (6) (13) (20) (27) (34) (41)	B ΔB K ΔK S_{100} ΔS_{100} (7) (14) (21) (28) (35) (42)	V ΔV $[3.6]$ $\Delta[3.6]$ S_{160} ΔS_{160} (8) (15) (22) (29) (36) (43)	R_c ΔR_c $[4.5]$ $\Delta[4.5]$ S_{250} ΔS_{250} (9) (16) (23) (30) (37) (44)	i' $\Delta i'$ $[5.8]$ $\Delta[5.8]$ S_{350} ΔS_{350} (10) (17) (24) (31) (38) (45)	z' $\Delta z'$ $[8.0]$ $\Delta[8.0]$ S_{500} ΔS_{500} (11) (18) (25) (32) (39) (46)
MIPS0016731	34.752794	−5.445827	0.8701 [†]	23.59	23.03	22.57	21.71	21.33
				0.01	0.01	0.01	0.01	0.01
				20.81	20.47	20.06	19.51	19.68	19.84	19.52
				0.01	0.02	0.01	0.04	0.04	0.04	0.13
				0.52	25.22	43.85	73.21	59.16
				0.02	1.66	3.46	5.86	4.38
MIPS0016798A	34.665386	−5.513587	0.7612 [†]	22.00	21.62	21.24	20.90	20.68
				0.01	0.01	0.01	0.01	0.01
				20.32	20.03	19.63	19.30	19.60	19.20	18.97
				0.01	0.01	0.01	0.04	0.04	0.04	0.08
				1.09	30.23	64.39	77.51	68.42	33.49	...
				0.02	2.57	5.15	6.12	4.52	4.19	...
MIPS0018398	34.235528	−4.848921	0.9600	26.93	25.62	24.76	23.61	22.87
				0.05	0.03	0.03	0.01	0.01
				21.93	21.50	20.90	20.44	20.68	20.77	21.06
				0.02	0.02	0.01	0.05	0.05	0.07	0.11
				0.16	...	14.01	30.43	23.84
				0.01	...	1.29	2.98	2.24
MIPS0018604	34.050621	−5.018885	0.8000	25.08	23.86	23.03	22.11	21.61
				0.02	0.01	0.01	0.01	0.01
				20.78	20.33	19.82	19.43	19.64	19.76	19.13
				0.01	0.01	0.01	0.04	0.04	0.04	0.04
				0.63	...	17.72	37.72	25.40
				0.02	...	1.54	3.58	2.51
MIPS0018747	34.568767	−4.858588	1.1000	25.39	24.24	23.50	22.57	21.79
				0.04	0.02	0.02	0.01	0.01
				20.88	20.35	19.65	19.07	19.20	19.44	19.31
				0.01	0.01	0.01	0.04	0.04	0.04	0.05
				0.61	22.52	39.27	18.97	...
				0.02	3.04	3.18	3.15	...
MIPS0019123	34.480225	−5.076031	0.8800	26.39	25.06	24.10	22.89	22.22
				0.07	0.02	0.02	0.01	0.01
				21.42	21.03	20.57	20.09	20.29	20.60	20.60
				0.02	0.02	0.01	0.04	0.04	0.08	0.07
				0.19	9.99	26.66	51.35	40.70	21.58	...
				0.02	1.74	2.08	4.01	3.09	4.58	...
MIPS0019351_1	34.656740	−5.108930	1.0800	24.63	24.12	23.71	23.10	22.48
				0.01	0.01	0.01	0.01	0.01
				21.72	21.22	20.61	19.97	20.21	20.64	20.67
				0.02	0.02	0.01	0.04	0.04	0.06	0.08
				0.23	21.16	15.21
				0.01	2.07	1.98

Continued in the next page

Table2 – continued from previous page

Galaxy	α	δ	z^\dagger	FUV ΔFUV J ΔJ S_{24} ΔS_{24} (5) (12) (19) (26) (33) (40)	NUV ΔNUV H ΔH S_{70} ΔS_{70} (6) (13) (20) (27) (34) (41)	B ΔB K ΔK S_{100} ΔS_{100} (7) (14) (21) (28) (35) (42)	V ΔV $[3.6]$ $\Delta[3.6]$ S_{160} ΔS_{160} (8) (15) (22) (29) (36) (43)	R_c ΔR_c $[4.5]$ $\Delta[4.5]$ S_{250} ΔS_{250} (9) (16) (23) (30) (37) (44)	i' $\Delta i'$ $[5.8]$ $\Delta[5.8]$ S_{350} ΔS_{350} (10) (17) (24) (31) (38) (45)	z' $\Delta z'$ $[8.0]$ $\Delta[8.0]$ S_{500} ΔS_{500} (11) (18) (25) (32) (39) (46)
MIPS0019961A	34.708831	-5.402780	1.1600	26.04	25.16	24.64	23.75	22.93
				0.03	0.02	0.02	0.01	0.02
				22.08	21.45	20.70	19.95	20.08	20.29	20.47
				0.02	0.02	0.01	0.04	0.04	0.05	0.07
				0.24	17.43	9.75
				0.01	2.20	2.31
MIPS0021138	34.007638	-4.729699	0.9300	25.07	24.21	23.48	22.46	21.84
				0.02	0.02	0.01	0.01	0.01
				21.25	20.86	20.40	19.69	19.88	19.60	19.75
				0.02	0.02	0.01	0.04	0.04	0.11	0.11
				0.23	...	11.67	29.69	23.81
				0.02	...	1.31	2.88	2.95
MIPS0021384A	34.078679	-4.816429	0.9200	24.93	23.88	23.12	22.13	21.51
				0.04	0.02	0.02	0.01	0.01
				20.58	20.11	19.50	18.96	19.15	18.69	19.48
				0.01	0.01	0.01	0.08	0.11	0.17	0.17
				0.57	22.09	18.16	14.61	...
				0.02	2.96	3.29	3.23	...
MIPS0021666_2	34.414448	-4.796615	1.1100	25.25	24.42	24.14	23.60	23.12
				0.02	0.01	0.01	0.01	0.01
				22.41	21.89	21.41	20.69	20.58	20.81	21.06
				0.02	0.03	0.01	0.04	0.03	0.05	0.06
				0.09	...	7.11	11.14
				0.01	...	1.24	2.21
MIPS0021759	34.767992	-4.678929	1.1200	25.59	24.78	24.17	23.30	22.57
				0.02	0.02	0.01	0.01	0.01
				21.71	21.14	20.37	19.60	19.71	20.10	19.88
				0.02	0.02	0.01	0.04	0.04	0.06	0.06
				0.39	...	16.34	33.65	29.14
				0.02	...	1.44	3.30	3.26
MIPS0022002	34.763766	-4.794346	1.1200	...	24.31	23.16	22.66	22.38	21.93	21.47
				...	0.20	0.01	0.01	0.01	0.01	0.01
				20.90	20.51	19.95	19.42	19.57	19.84	19.61
				0.01	0.01	0.01	0.04	0.04	0.04	0.05
				0.48	...	12.47	18.53
				0.02	...	1.30	2.09
MIPS0022211_1	34.332061	-5.093650	0.9100	24.60	23.77	23.22	22.34	21.85
				0.02	0.01	0.01	0.01	0.01
				20.81	20.59	20.03	19.61	19.81	19.72	19.54
				0.01	0.02	0.01	0.03	0.03	0.04	0.06
				0.94	12.15	22.11	29.31	20.16
				0.03	1.82	1.72	2.34	2.46

Continued in the next page

Table2 – continued from previous page

Galaxy	α	δ	z^\dagger	FUV ΔFUV J ΔJ S_{24} ΔS_{24} (5) (12) (19) (26) (33) (40)	NUV ΔNUV H ΔH S_{70} ΔS_{70} (6) (13) (20) (27) (34) (41)	B ΔB K ΔK S_{100} ΔS_{100} (7) (14) (21) (28) (35) (42)	V ΔV $[3.6]$ $\Delta[3.6]$ S_{160} ΔS_{160} (8) (15) (22) (29) (36) (43)	R_c ΔR_c $[4.5]$ $\Delta[4.5]$ S_{250} ΔS_{250} (9) (16) (23) (30) (37) (44)	i' $\Delta i'$ $[5.8]$ $\Delta[5.8]$ S_{350} ΔS_{350} (10) (17) (24) (31) (38) (45)	z' $\Delta z'$ $[8.0]$ $\Delta[8.0]$ S_{500} ΔS_{500} (11) (18) (25) (32) (39) (46)
MIPS0022445A	34.534316	-5.105007	1.1600	23.83	23.24	22.77	22.20	21.47
				0.01	0.01	0.01	0.01	0.01
				20.74	20.31	19.75	19.22	19.31	19.65	19.62
				0.01	0.01	0.01	0.04	0.04	0.04	0.06
				0.38	24.90	34.93
				0.01	2.02	3.21
MIPS0022836	34.874495	-5.150121	0.7100	23.15	22.47	21.79	21.24	20.93
				0.01	0.01	0.01	0.01	0.01
				20.22	19.62	18.94	18.35	18.64	18.47	18.59
				0.01	0.01	0.01	0.03	0.06	0.05	0.17
				1.44	16.34	32.63	59.45	51.86
				0.03	2.04	2.64	4.82	3.73
MIPS0023305_1	34.615443	-5.485555	0.9300	25.09	24.28	23.91	23.10	22.69
				0.01	0.02	0.01	0.01	0.01
				21.86	21.72	21.09	20.35	20.64	20.73	20.55
				0.02	0.02	0.01	0.04	0.03	0.05	0.06
				0.27	...	9.44	18.67
				0.01	...	1.26	3.16
MIPS0024518	34.320287	-4.687332	1.1100	24.21	23.93	23.72	23.04	22.65
				0.01	0.01	0.01	0.01	0.01
				22.18	21.63	20.92	19.99	20.05	20.36	19.92
				0.02	0.02	0.01	0.04	0.04	0.07	0.05
				0.31	...	9.83	25.67	...	23.09	...
				0.01	...	1.09	2.85	...	3.32	...
MIPS0024714A	34.704317	-4.647177	1.1200	24.12	23.48	23.10	22.46	21.85
				0.01	0.01	0.01	0.01	0.01
				21.26	20.77	20.11	19.44	19.50	19.82	19.98
				0.04	0.03	0.02	0.15	0.17	0.29	0.35
				0.41	16.42	24.28
				0.01	2.10	3.16
MIPS0024996A	34.393203	-4.982584	1.1807 [†]	24.07	23.56	23.22	22.56	21.85
				0.02	0.02	0.01	0.01	0.01
				21.22	20.75	20.19	19.61	19.58	19.80	19.91
				0.02	0.02	0.01	0.19	0.17	0.28	0.29
				0.22	...	7.03	18.65	29.68	25.06	...
				0.02	...	0.68	1.73	2.40	5.86	...
MIPS0025409A	34.248883	-5.330265	1.2400	24.92	24.68	24.33	23.74	22.95
				0.02	0.02	0.01	0.01	0.02
				22.32	21.76	21.32	20.65	20.55	20.48	20.10
				0.02	0.03	0.01	0.05	0.04	0.06	0.06
				0.09	...	5.26	...	12.29
				0.02	...	0.53	...	1.91

Continued in the next page

Table2 – continued from previous page

Galaxy	α	δ	z^\dagger	FUV ΔFUV J ΔJ S_{24} ΔS_{24} (5) (12) (19) (26) (33) (40)	NUV ΔNUV H ΔH S_{70} ΔS_{70} (6) (13) (20) (27) (34) (41)	B ΔB K ΔK S_{100} ΔS_{100} (7) (14) (21) (28) (35) (42)	V ΔV $[3.6]$ $\Delta[3.6]$ S_{160} ΔS_{160} (8) (15) (22) (29) (36) (43)	R_c ΔR_c $[4.5]$ $\Delta[4.5]$ S_{250} ΔS_{250} (9) (16) (23) (30) (37) (44)	i' $\Delta i'$ $[5.8]$ $\Delta[5.8]$ S_{350} ΔS_{350} (10) (17) (24) (31) (38) (45)	z' $\Delta z'$ $[8.0]$ $\Delta[8.0]$ S_{500} ΔS_{500} (11) (18) (25) (32) (39) (46)
MIPS0025572A	34.211377	−5.452126	1.1000	25.33	24.51	23.66	22.73	21.97
				0.03	0.02	0.02	0.01	0.01
				21.09	20.57	19.98	19.31	19.45	19.78	19.47
				0.01	0.01	0.01	0.04	0.04	0.04	0.05
				0.43	...	21.26	47.01	59.43	30.40	...
				0.02	...	1.87	3.90	4.28	3.44	...
MIPS0025717A	34.611315	−5.357076	0.8500	24.26	23.29	22.59	21.81	21.37
				0.01	0.01	0.01	0.01	0.01
				20.36	19.92	19.33	18.87	19.15	18.90	19.09
				0.01	0.01	0.01	0.04	0.04	0.03	0.04
				1.29	17.40	36.70	68.55	...	34.81	...
				0.03	1.74	2.86	5.35	...	3.73	...
MIPS0025946	34.674810	−5.486638	1.1800	24.24	23.76	23.40	22.88	22.21
				0.01	0.01	0.01	0.01	0.01
				21.62	21.16	20.61	20.04	20.01	20.32	20.13
				0.01	0.02	0.01	0.04	0.04	0.06	0.23
				0.23	...	9.63	21.15	23.42
				0.01	...	1.07	3.17	2.39
MIPS0027542A	34.493761	−5.182032	0.9800	25.65	24.90	24.25	23.25	22.63
				0.04	0.02	0.02	0.01	0.01
				21.78	21.30	20.82	20.26	20.27	20.17	20.45
				0.02	0.02	0.01	0.05	0.04	0.05	0.08
				0.24	8.96	16.42	23.56
				0.01	1.59	1.28	1.88
MIPS0027595A	34.687484	−5.134991	0.7000	23.29	22.34	21.33	20.68	20.25
				0.01	0.01	0.01	0.01	0.01
				19.48	18.86	18.33	18.10	18.44	18.15	18.24
				0.01	0.01	0.01	0.09	0.09	0.14	0.11
				0.92	22.21	...	78.81	82.11	47.00	...
				0.02	1.91	...	6.30	5.17	4.18	...
MIPS0029054	34.506005	−5.025563	1.0910 ^{dagger}	23.64	22.93	22.57	21.99	21.36
				0.01	0.01	0.01	0.01	0.01
				20.65	20.26	19.75	19.25	19.42	19.72	19.85
				0.01	0.01	0.01	0.04	0.04	0.04	0.06
				0.40	...	8.94	21.74	27.67
				0.02	...	0.86	1.96	3.27
MIPS0029170A	34.787744	−4.989188	1.2100	25.36	24.80	24.15	23.48	22.73
				0.03	0.02	0.02	0.01	0.02
				21.70	21.19	20.44	19.72	19.82	20.17	20.11
				0.02	0.02	0.01	0.04	0.04	0.05	0.06
				0.22	15.44	31.65
				0.01	2.30	2.91

Continued in the next page

Table2 – continued from previous page

Galaxy	α	δ	z^\dagger	FUV ΔFUV J ΔJ S_{24} ΔS_{24} (5) (12) (19) (26) (33) (40)	NUV ΔNUV H ΔH S_{70} ΔS_{70} (6) (13) (20) (27) (34) (41)	B ΔB K ΔK S_{100} ΔS_{100} (7) (14) (21) (28) (35) (42)	V ΔV $[3.6]$ $\Delta[3.6]$ S_{160} ΔS_{160} (8) (15) (22) (29) (36) (43)	R_c ΔR_c $[4.5]$ $\Delta[4.5]$ S_{250} ΔS_{250} (9) (16) (23) (30) (37) (44)	i' $\Delta i'$ $[5.8]$ $\Delta[5.8]$ S_{350} ΔS_{350} (10) (17) (24) (31) (38) (45)	z' $\Delta z'$ $[8.0]$ $\Delta[8.0]$ S_{500} ΔS_{500} (11) (18) (25) (32) (39) (46)
MIPS0030478_1	34.529652	−5.052284	1.1100	24.95	24.40	24.04	23.38	22.83
				0.02	0.01	0.01	0.01	0.01
				22.27	21.90	21.36	20.59	20.68	20.89	20.88
				0.02	0.03	0.01	0.05	0.04	0.06	0.07
				0.22	...	3.96	15.86
				0.02	...	0.52	1.57
MIPS0031380A	34.373847	−4.993434	1.1200	25.44	24.60	23.81	22.90	22.04
				0.04	0.02	0.01	0.01	0.01
				21.18	20.68	20.02	19.37	19.45	19.83	19.57
				0.01	0.02	0.01	0.15	0.17	0.26	0.33
				0.46	...	11.25	...	30.40	24.87	...
				0.02	...	1.00	...	2.67	4.23	...
MIPS0031422A	34.433523	−5.048367	1.1200	25.82	25.00	24.23	23.29	22.53
				0.10	0.06	0.04	0.02	0.02
				21.64	21.10	20.44	19.73	19.81	19.88	20.34
				0.02	0.02	0.01	0.04	0.04	0.05	0.07
				0.22	...	7.85	14.02
				0.01	...	0.82	1.47
MIPS0032241A	34.525408	−5.213786	1.1100	24.88	24.33	23.81	22.94	22.22
				0.02	0.02	0.01	0.01	0.01
				21.55	21.00	20.30	19.61	19.73	20.10	19.86
				0.02	0.02	0.01	0.04	0.04	0.05	0.05
				0.26	52.65	49.75
				0.01	4.11	3.28
MIPS0032586A	34.265339	−4.808439	1.0500	22.64	22.38	22.25	21.89	21.49
				0.01	0.01	0.01	0.01	0.01
				21.20	20.98	20.64	20.38	20.55	20.78	19.66
				0.01	0.02	0.01	0.05	0.05	0.08	0.05
				0.19	...	9.25	21.45	16.22
				0.02	...	1.18	2.27	2.19
MIPS0032738	34.568342	−5.133726	1.1500	27.09	25.85	24.85	24.06	22.96
				0.10	0.05	0.03	0.02	0.01
				21.96	21.37	20.79	20.08	20.04	20.49	20.22
				0.02	0.02	0.01	0.04	0.04	0.07	0.06
				0.11	...	7.37	...	21.26
				0.02	...	0.65	...	2.06
MIPS0033398A	34.282420	−4.956628	1.0700	23.30	22.76	22.34	21.72	21.09
				0.01	0.01	0.01	0.01	0.01
				20.47	20.10	19.58	19.13	19.30	19.47	19.47
				0.01	0.01	0.01	0.04	0.04	0.04	0.05
				0.49	...	1...	21.72	24.12
				0.02	...	0.98	1.93	2.32

Continued in the next page

Table2 – continued from previous page

Galaxy	α	δ	z^\dagger	FUV ΔFUV J ΔJ S_{24} ΔS_{24} (5) (12) (19) (26) (33) (40)	NUV ΔNUV H ΔH S_{70} ΔS_{70} (6) (13) (20) (27) (34) (41)	B ΔB K ΔK S_{100} ΔS_{100} (7) (14) (21) (28) (35) (42)	V ΔV $[3.6]$ $\Delta[3.6]$ S_{160} ΔS_{160} (8) (15) (22) (29) (36) (43)	R_c ΔR_c $[4.5]$ $\Delta[4.5]$ S_{250} ΔS_{250} (9) (16) (23) (30) (37) (44)	i' $\Delta i'$ $[5.8]$ $\Delta[5.8]$ S_{350} ΔS_{350} (10) (17) (24) (31) (38) (45)	z' $\Delta z'$ $[8.0]$ $\Delta[8.0]$ S_{500} ΔS_{500} (11) (18) (25) (32) (39) (46)
MIPS0033408	34.755542	−4.768890	0.8800	25.48	24.61	24.00	23.05	22.48
				0.02	0.01	0.01	0.01	0.01
				21.77	21.41	20.85	20.29	20.60	20.62	20.56
				0.02	0.02	0.01	0.05	0.05	0.07	0.07
				0.25	...	10.36	23.50	26.62	18.27	...
				0.02	...	1.11	2.44	3.59	3.43	...
MIPS0033690_1	34.534649	−5.007750	1.1500	26.17	25.53	24.67	23.73	22.89
				0.04	0.04	0.02	0.01	0.01
				22.04	21.50	20.81	19.84	19.82	19.91	19.39
				0.02	0.02	0.01	0.03	0.03	0.04	0.06
				0.18	...	6.70	21.34	20.36
				0.01	...	0.86	1.96	3.40
MIPS0033897	34.597075	−4.967596	1.0900	24.30	23.72	23.38	22.80	22.24
				0.02	0.01	0.01	0.01	0.01
				21.70	21.33	20.81	20.25	20.41	20.80	20.37
				0.02	0.02	0.01	0.05	0.04	0.09	0.06
				0.21	...	6.40	...	22.68
				0.02	...	0.74	...	2.83
MIPS0034055A	34.317467	−5.000109	0.8400	22.05	21.66	21.33	20.84	20.59
				0.01	0.01	0.01	0.01	0.01
				20.07	19.95	19.63	19.16	19.50	19.34	19.81
				0.01	0.01	0.01	0.17	0.24	0.38	0.24
				0.41	...	14.91	25.77	25.38	16.93	...
				0.01	...	1.25	2.35	2.61	3.61	...
MIPS0034350A	34.722438	−5.275812	0.9400	23.96	23.30	23.02	22.04	21.71
				0.02	0.01	0.01	0.01	0.01
				20.98	20.68	20.15	19.86	20.07	20.14	20.27
				0.01	0.02	0.01	0.04	0.04	0.05	0.07
				0.35	25.91	31.02	16.66	...
				0.01	2.62	2.64	3.10	...
MIPS0034419	34.783759	−4.854334	0.9700	25.76	25.02	24.26	23.24	22.68
				0.03	0.03	0.02	0.01	0.02
				21.79	21.26	20.72	20.03	20.19	20.31	20.25
				0.02	0.02	0.01	0.04	0.04	0.05	0.06
				0.19	...	13.09	22.48	17.59
				0.01	...	1.23	2.32	2.39
MIPS0034471	34.758220	−5.521120	1.0200	24.15	23.66	22.98	22.30	21.61
				0.01	0.01	0.01	0.01	0.01
				20.98	20.57	20.07	19.50	19.68	20.00	20.66
				0.02	0.02	0.01	0.04	0.04	0.05	0.37
				0.18	...	13.26	39.21	...	44.77	...
				0.02	...	1.23	3.72	...	5.15	...

Continued in the next page

Table2 – continued from previous page

Galaxy	α	δ	z^\dagger	FUV ΔFUV J ΔJ S_{24} ΔS_{24}	NUV ΔNUV H ΔH S_{70} ΔS_{70}	B ΔB K ΔK S_{100} ΔS_{100}	V ΔV $[3.6]$ $\Delta[3.6]$ S_{160} ΔS_{160}	R_c ΔR_c $[4.5]$ $\Delta[4.5]$ S_{250} ΔS_{250}	i' $\Delta i'$ $[5.8]$ $\Delta[5.8]$ S_{350} ΔS_{350}	z' $\Delta z'$ $[8.0]$ $\Delta[8.0]$ S_{500} ΔS_{500}
(1)	(2)	(3)	(4)	(5)	(6)	(7)	(8)	(9)	(10)	(11)
				(12)	(13)	(14)	(15)	(16)	(17)	(18)
				(19)	(20)	(21)	(22)	(23)	(24)	(25)
				(26)	(27)	(28)	(29)	(30)	(31)	(32)
				(33)	(34)	(35)	(36)	(37)	(38)	(39)
				(40)	(41)	(42)	(43)	(44)	(45)	(46)
MIPS0034593	34.845053	−4.830812	1.0200	23.82	23.38	23.09	22.48	22.00
				0.01	0.01	0.01	0.01	0.01
				21.34	20.94	20.39	19.78	19.87	20.21	20.01
				0.01	0.02	0.01	0.04	0.04	0.06	0.08
				0.20	...	9.30	22.03	24.48	17.54	...
				0.01	...	1.10	2.25	3.08	4.02	...
MIPS0034710_1	34.833298	−4.896593	0.9620 [†]	26.53	25.08	23.94	22.84	22.25
				0.06	0.02	0.01	0.01	0.01
				21.21	20.66	20.03	19.54	19.77	19.99	19.94
				0.01	0.01	0.01	0.03	0.03	0.04	0.06
				0.32	15.69	25.26	36.59
				0.02	2.13	2.07	3.44
MIPS0035194A	34.668258	−5.334233	0.9300 [†]	...	23.95	22.54	21.97	21.67	21.09	20.72
				...	0.16	0.01	0.01	0.01	0.01	0.01
				20.01	19.87	19.46	19.10	19.37	19.33	19.31
				0.01	0.01	0.01	0.04	0.04	0.04	0.05
				1.04	...	30.12	45.98	29.19
				0.03	...	2.41	3.82	3.24

Table 2: Dusty-starburst complementary-sample multi-band photometry. (1) Name of the galaxy. (2,3) Right ascension and declination (J2000) in degrees. (4) Photometric or spectroscopic redshift (z_{spec} indicated by a \dagger). (33-39) Flux densities in MIPS 24, 70; PACS 100, 160; SPIRE 250, 350, 500 in mJy (synthetic fluxes indicated by s). (5-11,19-25) Observed magnitude in FUV, NUV; B , V , R_c , i' , z' ; J , H , K ; IRAC 3.6-8.0 in the AB photometric system. (40-46) Associated uncertainties to MIPS 24, 70; PACS 100, 160; SPIRE 250, 350, 500 in mJy determined as described in Sections 2.1 and 2.2. (12-18,26-32) Associated uncertainties to FUV, NUV; B , V , R_c , i' , z' ; J , H , K ; IRAC 3.6-8.0 as obtained from the aperture matched cataloguing (see Section 3.2). “...” indicate bands without detections or without reliable photometric measurements.

Galaxy	α	δ	z^\dagger	FUV ΔFUV	NUV ΔNUV	B ΔB	V ΔV	R_c ΔR_c	i' $\Delta i'$	z' $\Delta z'$
				J	H	K	[3.6]	[4.5]	[5.8]	[8.0]
				ΔJ	ΔH	ΔK	$\Delta[3.6]$	$\Delta[4.5]$	$\Delta[5.8]$	$\Delta[8.0]$
				S_{24}	S_{70}	S_{100}	S_{160}	S_{250}	S_{350}	S_{500}
				ΔS_{24}	ΔS_{70}	ΔS_{100}	ΔS_{160}	ΔS_{250}	ΔS_{350}	ΔS_{500}
(1)	(2)	(3)	(4)	(5)	(6)	(7)	(8)	(9)	(10)	(11)
				(12)	(13)	(14)	(15)	(16)	(17)	(18)
				(19)	(20)	(21)	(22)	(23)	(24)	(25)
				(26)	(27)	(28)	(29)	(30)	(31)	(32)
				(33)	(34)	(35)	(36)	(37)	(38)	(39)
				(40)	(41)	(42)	(43)	(44)	(45)	(46)
MIPS0000373_1	34.706626	-4.782122	1.1100	24.42	23.79	23.41	22.80	22.16
				0.02	0.01	0.01	0.01	0.01
				21.50	21.05	20.46	19.82	20.06	20.32	20.46
				0.01	0.02	0.01	0.03	0.03	0.04	0.06
				0.37	...	3.40 ^s	8.29 ^s	17.44	18.21 ^s	...
				0.01	...	1.57 ^s	3.82 ^s	2.39	8.39 ^s	...
MIPS0000814_1	34.434914	-5.497713	1.1200	23.73	23.12	22.70	22.21	21.62
				0.01	0.01	0.01	0.01	0.01
				21.05	20.65	20.15	19.51	19.58	19.92	19.78
				0.01	0.01	0.01	0.03	0.03	0.04	0.06
				0.42	...	3.59 ^s	9.07 ^s	21.07	22.88 ^s	...
				0.02	...	1.65 ^s	4.18 ^s	2.68	10.54 ^s	...
MIPS0002259_1	34.535619	-5.056534	0.9500	26.03	24.90	24.23	23.12	22.55
				0.03	0.01	0.01	0.01	0.01
				21.76	21.44	21.04	20.47	20.63	20.68	20.29
				0.02	0.02	0.01	0.04	0.04	0.05	0.06
				0.28	8.59 ^s	12.11	9.44 ^s
				0.02	3.96 ^s	1.04	4.35 ^s
MIPS0002824_1	34.836209	-5.293364	1.1000	27.17	26.08	25.47	24.59	23.93
				0.12	0.07	0.04	0.02	0.02
				23.38	22.87	22.10	21.19	21.14	21.50	21.20
				0.05	0.08	0.02	0.05	0.04	0.06	0.07
				0.17	...	7.31 ^s	11.29	9.97 ^s
				0.02	...	3.37 ^s	1.79	4.59 ^s
MIPS0009184	34.331835	-5.119921	0.9000	...	22.78	22.32	21.90	21.77	21.11	20.86
				...	0.08	0.01	0.01	0.01	0.01	0.01
				20.56	20.46	20.17	19.95	20.23	20.12	20.16
				0.01	0.01	0.01	0.04	0.04	0.05	0.06
				0.33	7.87 ^s	11.83	11.44 ^s	7.38 ^s
				0.01	3.62 ^s	0.93	5.27 ^s	3.40 ^s
MIPS0009498	34.125411	-5.269119	1.1000	24.34	23.67	23.34	22.74	22.13
				0.02	0.02	0.01	0.01	0.01
				21.48	21.11	20.55	20.10	20.21	20.41	20.44
				0.02	0.02	0.01	0.04	0.04	0.06	0.07
				0.24	...	4.72 ^s	9.72 ^s	8.05 ^s
				0.02	...	2.17 ^s	4.48 ^s	3.71 ^s

Continued in the next page

Table2 – continued from previous page

Galaxy	α	δ	z^{\dagger}	FUV ΔFUV J ΔJ S_{24} ΔS_{24}	NUV ΔNUV H ΔH S_{70} ΔS_{70}	B ΔB K ΔK S_{100} ΔS_{100}	V ΔV $[3.6]$ $\Delta[3.6]$ S_{160} ΔS_{160}	R_c ΔR_c $[4.5]$ $\Delta[4.5]$ S_{250} ΔS_{250}	i' $\Delta i'$ $[5.8]$ $\Delta[5.8]$ S_{350} ΔS_{350}	z' $\Delta z'$ $[8.0]$ $\Delta[8.0]$ S_{500} ΔS_{500}
(1)	(2)	(3)	(4)	(5)	(6)	(7)	(8)	(9)	(10)	(11)
				(12)	(13)	(14)	(15)	(16)	(17)	(18)
				(19)	(20)	(21)	(22)	(23)	(24)	(25)
				(26)	(27)	(28)	(29)	(30)	(31)	(32)
				(33)	(34)	(35)	(36)	(37)	(38)	(39)
				(40)	(41)	(42)	(43)	(44)	(45)	(46)
MIPS0010330	34.677957	−5.173804	1.1700	25.35	24.55	23.96	23.32	22.52
				0.02	0.01	0.01	0.01	0.01
				21.72	21.18	20.50	19.90	19.92	20.26	20.00
				0.02	0.02	0.01	0.04	0.04	0.05	0.05
				0.29	...	2.49 ^s	6.31 ^s	17.72	19.61 ^s	...
				0.02	...	1.15 ^s	2.91 ^s	2.30	9.03 ^s	...
MIPS0014675_1	34.272441	−4.780641	1.0200	23.65	23.24	22.86	22.36	21.87
				0.01	0.01	0.01	0.01	0.01
				21.45	21.19	20.69	20.20	20.47	20.84	20.66
				0.01	0.02	0.01	0.04	0.03	0.05	0.06
				0.26	...	7.98 ^s	10.44 ^s	8.93 ^s
				0.02	...	3.68 ^s	4.81 ^s	4.11 ^s
MIPS0014844_1	34.078836	−4.949095	1.1300	25.84	25.08	24.72	23.97	23.41
				0.03	0.02	0.02	0.02	0.02
				22.60	22.10	21.36	20.42	20.56	20.79	20.45
				0.03	0.03	0.01	0.04	0.03	0.05	0.06
				0.26	...	11.49 ^s	18.70	16.44 ^s
				0.02	...	5.29 ^s	2.09	7.57 ^s
MIPS0019428	34.525713	−5.212479	0.9600	22.86	22.48	22.21	21.67	21.09
				0.01	0.01	0.01	0.01	0.01
				20.51	20.07	19.56	19.15	19.27	19.32	18.90
				0.01	0.01	0.01	0.04	0.04	0.04	0.04
				0.52	10.41 ^s	17.55 ^s	19.76 ^s	14.77 ^s
				0.02	4.79 ^s	8.08 ^s	9.10 ^s	6.80 ^s
MIPS0019443	34.836930	−5.075284	1.0800	25.86	25.15	24.63	23.76	23.27
				0.04	0.03	0.02	0.01	0.02
				22.51	22.03	21.31	20.50	20.69	20.93	20.88
				0.03	0.03	0.01	0.05	0.05	0.12	0.09
				0.18	...	12.25 ^s	16.79	12.72 ^s
				0.01	...	5.64 ^s	2.28	5.86 ^s
MIPS0021613_1	33.998241	−4.969659	1.1400	25.42	24.60	23.93	23.24	22.45
				0.02	0.01	0.01	0.01	0.01
				21.61	20.99	20.47	19.82	19.91	20.40	20.17
				0.05	0.03	0.02	0.03	0.03	0.04	0.06
				0.37	...	3.12 ^s	8.00 ^s	21.86	23.69 ^s	...
				0.02	...	1.44 ^s	3.69 ^s	2.47	10.91 ^s	...
MIPS0022473	34.747713	−5.017365	1.1500	...	23.57	22.37	21.99	21.80	21.39	20.95
				...	0.13	0.01	0.01	0.01	0.01	0.01
				20.58	20.33	19.99	19.70	19.85	20.29	20.13
				0.01	0.01	0.01	0.04	0.04	0.05	0.06
				0.30	...	2.74 ^s	6.59 ^s	14.15	15.37 ^s	...
				0.01	...	1.26 ^s	3.04 ^s	2.09	7.08 ^s	...

Continued in the next page

Table2 – continued from previous page

Galaxy	α	δ	z^\dagger	FUV ΔFUV J ΔJ S_{24} ΔS_{24}	NUV ΔNUV H ΔH S_{70} ΔS_{70}	B ΔB K ΔK S_{100} ΔS_{100}	V ΔV $[3.6]$ $\Delta[3.6]$ S_{160} ΔS_{160}	R_c ΔR_c $[4.5]$ $\Delta[4.5]$ S_{250} ΔS_{250}	i' $\Delta i'$ $[5.8]$ $\Delta[5.8]$ S_{350} ΔS_{350}	z' $\Delta z'$ $[8.0]$ $\Delta[8.0]$ S_{500} ΔS_{500}
(1)	(2)	(3)	(4)	(5)	(6)	(7)	(8)	(9)	(10)	(11)
				(12)	(13)	(14)	(15)	(16)	(17)	(18)
				(19)	(20)	(21)	(22)	(23)	(24)	(25)
				(26)	(27)	(28)	(29)	(30)	(31)	(32)
				(33)	(34)	(35)	(36)	(37)	(38)	(39)
				(40)	(41)	(42)	(43)	(44)	(45)	(46)
MIPS0022520_2	34.874160	−4.980549	1.1800	23.31	22.91	22.54	22.30	22.08
				0.01	0.01	0.01	0.01	0.01
				21.41	21.08	20.83	20.25	20.20	20.54	20.41
				0.01	0.02	0.01	0.04	0.03	0.05	0.07
				0.22	...	4.62 ^s	10.11 ^s	8.71 ^s
				0.02	...	2.13 ^s	4.65 ^s	4.01 ^s
MIPS0024399_1	34.064497	−4.724107	1.1900	26.53	25.69	24.67	23.67	22.73
				0.05	0.03	0.02	0.01	0.01
				21.66	21.06	20.38	19.70	19.87	19.76	20.43
				0.01	0.02	0.01	0.03	0.03	0.04	0.06
				0.18	5.22 ^s	14.70	14.54 ^s	...
				0.01	2.41 ^s	2.41	6.69 ^s	...
MIPS0027217_1	34.126908	−5.076468	1.0200	24.07	23.54	23.11	22.49	21.84
				0.02	0.02	0.02	0.02	0.02
				21.08	20.64	20.07	19.35	19.55	19.88	20.05
				0.01	0.01	0.01	0.03	0.03	0.04	0.06
				0.29	...	5.44 ^s	10.30 ^s	8.12 ^s
				0.02	...	2.51 ^s	4.74 ^s	3.74 ^s
MIPS0027657_3	34.686706	−5.196298	1.1900	24.68	24.17	23.88	23.35	22.61
				0.02	0.01	0.01	0.01	0.02
				21.77	21.11	20.58	19.90	19.89	20.44	20.26
				0.01	0.02	0.01	0.03	0.03	0.04	0.06
				0.22	6.07 ^s	16.92	16.88 ^s	...
				0.01	2.79 ^s	2.00	7.78 ^s	...
MIPS0033008	34.443483	−4.706114	1.1900	...	22.77	22.02	21.77	21.65	21.36	20.89
				...	0.10	0.01	0.01	0.01	0.01	0.01
				20.53	20.30	19.89	19.61	19.72	20.04	20.08
				0.01	0.01	0.01	0.04	0.04	0.05	0.05
				0.26	...	5.59 ^s	12.34 ^s	10.72 ^s
				0.02	...	2.57 ^s	5.68 ^s	4.94 ^s

Table 5: Stellar population synthesis results for main-sample dusty starbursts. Median and 1σ error values are shown for each parameter derived with the SYNTHESIZER code. The expected and standard deviation (or upper and lower limits when changing from logarithmic space to linear space) values are quoted for each parameter estimated with the CIGALE. (1) Name of the galaxy. (2) Photometric or spectroscopic redshift (z_{spec} indicated by a †). (3) Code used to derive the parameters. (4) Stellar mass (in solar units) and its uncertainty derived from the logarithmic space. (5) Parameter values for the old or the young population. (6) e -folding time and its uncertainty (old population in Myr and young population in Gyr). (7) Age and its uncertainty (old population in Gyr and young population in Myr). (8) Attenuation in the V -band and its uncertainty in mag. (9) Metallicity value (fixed to the solar value) in solar units. (10) Most recent burst intensity fraction and its uncertainty in percentage.

Galaxy	z^\dagger	Code	$\log M_\star$ [M_\odot]	Pop.	τ old [Myr] you [Gyr]	Age old [Gyr] you [Myr]	A_V [mag]	Z [Z_\odot]	b [%]
(1)	(2)	(3)	(4)	(5)	(6)	(7)	(8)	(9)	(10)
MIPS0000517A	1.0500	Synthesizer	$10.0^{+0.1}_{-0.1}$	old	230^{+43}_{-125}	$1.0^{+0.2}_{-0.1}$	$0.0^{+0.1}_{-0.0}$	1.0	
				you	$18.5^{+3.1}_{-3.2}$	39^{+6}_{-7}	$1.9^{+0.1}_{-0.1}$	1.0	69^{+2}_{-23}
		CIGALE	10.1 ± 0.2	old	1280^{+5762}_{-1047}	3.2 ± 1.6	$1.0^{+0.7}_{-0.7}$	1.0	
				you	20.0	46^{+34}_{-20}	1.9 ± 0.2	1.0	61 ± 26
MIPS0000648A	1.1900	Synthesizer	$10.4^{+0.1}_{-0.1}$	old	162^{+46}_{-45}	$1.0^{+0.1}_{-0.1}$	$0.0^{+0.1}_{-0.0}$	1.0	
				you	$17.7^{+3.4}_{-2.7}$	45^{+21}_{-19}	$2.3^{+0.1}_{-0.1}$	1.0	51^{+13}_{-16}
		CIGALE	10.6 ± 0.1	old	1189^{+5363}_{-973}	3.2 ± 1.6	$1.2^{+0.7}_{-0.7}$	1.0	
				you	20.0	100^{+90}_{-47}	2.2 ± 0.2	1.0	57 ± 27
MIPS0000816_1	0.9300	Synthesizer	$10.2^{+0.2}_{-0.2}$	old	141^{+113}_{-45}	$2.4^{+1.0}_{-0.5}$	$0.0^{+0.3}_{-0.0}$	1.0	
				you	$18.9^{+2.9}_{-3.2}$	8^{+1}_{-1}	$1.5^{+0.1}_{-0.1}$	1.0	21^{+18}_{-10}
		CIGALE	9.9 ± 0.3	old	1285^{+5815}_{-1053}	4.1 ± 1.6	$0.5^{+0.4}_{-0.4}$	1.0	
				you	20.0	22^{+29}_{-13}	1.1 ± 0.2	1.0	49 ± 30
MIPS0000826	0.7200	Synthesizer	$10.5^{+0.1}_{-0.1}$	old	247^{+32}_{-37}	$3.0^{+0.4}_{-0.3}$	$0.0^{+0.1}_{-0.0}$	1.0	
				you	$19.8^{+2.5}_{-2.4}$	9^{+1}_{-1}	$3.2^{+0.1}_{-0.1}$	1.0	25^{+3}_{-5}
		CIGALE	10.7 ± 0.1	old	314^{+686}_{-215}	5.5 ± 1.4	$0.0^{+0.1}_{-0.0}$	1.0	
				you	20.0	10^{+1}_{-1}	3.2 ± 0.2	1.0	11 ± 4
MIPS0001713	1.1100	Synthesizer	$10.4^{+0.1}_{-0.1}$	old	177^{+35}_{-38}	$1.0^{+0.1}_{-0.1}$	$0.2^{+0.1}_{-0.1}$	1.0	
				you	$17.6^{+3.3}_{-2.8}$	55^{+20}_{-17}	$2.1^{+0.1}_{-0.1}$	1.0	36^{+11}_{-11}
		CIGALE	10.6 ± 0.1	old	1264^{+5495}_{-1027}	3.4 ± 1.5	$1.0^{+0.6}_{-0.6}$	1.0	
				you	20.0	204^{+365}_{-131}	1.9 ± 0.4	1.0	51 ± 30
MIPS0002196_1	1.0980	Synthesizer	$10.5^{+0.1}_{-0.1}$	old	123^{+50}_{-25}	$1.1^{+0.4}_{-0.2}$	$0.1^{+0.1}_{-0.1}$	1.0	
				you	$17.6^{+3.4}_{-2.7}$	62^{+17}_{-15}	$3.3^{+0.1}_{-0.1}$	1.0	61^{+6}_{-7}
		CIGALE	10.8 ± 0.1	old	398^{+1650}_{-320}	3.4 ± 1.6	$1.2^{+1.1}_{-1.1}$	1.0	
				you	20.0	151^{+150}_{-75}	3.1 ± 0.2	1.0	64 ± 25
MIPS0002371A	1.1800	Synthesizer	$10.7^{+0.2}_{-0.2}$	old	159^{+86}_{-56}	$2.1^{+2.3}_{-0.7}$	$1.4^{+0.1}_{-0.1}$	1.0	
				you	$18.3^{+3.2}_{-3.1}$	63^{+15}_{-14}	$1.7^{+0.1}_{-0.1}$	1.0	19^{+10}_{-8}
		CIGALE	10.6 ± 0.2	old	1964^{+7552}_{-1559}	3.1 ± 1.6	$1.1^{+0.8}_{-0.8}$	1.0	
				you	20.0	95^{+143}_{-57}	2.2 ± 0.7	1.0	35 ± 27
MIPS0002397A	0.8020	Synthesizer	$10.8^{+0.1}_{-0.1}$	old	207^{+46}_{-38}	$2.0^{+0.3}_{-0.2}$	$0.0^{+0.1}_{-0.0}$	1.0	
				you	$18.1^{+3.3}_{-3.0}$	77^{+17}_{-19}	$2.1^{+0.1}_{-0.1}$	1.0	30^{+5}_{-6}
		CIGALE	10.9 ± 0.1	old	1040^{+4570}_{-847}	4.4 ± 1.5	$0.9^{+0.7}_{-0.7}$	1.0	
				you	20.0	220^{+245}_{-116}	2.0 ± 0.3	1.0	52 ± 29
MIPS0002670A	0.9300	Synthesizer	$10.2^{+0.1}_{-0.1}$	old	221^{+48}_{-91}	$2.5^{+1.4}_{-0.6}$	$1.3^{+0.2}_{-1.2}$	1.0	
				you	$16.3^{+3.1}_{-2.0}$	39^{+8}_{-12}	$1.3^{+0.1}_{-0.0}$	1.0	64^{+3}_{-10}
		CIGALE	10.2 ± 0.3	old	1421^{+6295}_{-1159}	4.1 ± 1.6	$0.6^{+0.5}_{-0.5}$	1.0	
				you	20.0	23^{+18}_{-10}	1.3 ± 0.1	1.0	45 ± 31
MIPS0004202_1	1.1000	Synthesizer	$10.3^{+0.1}_{-0.1}$	old	173^{+81}_{-59}	$1.0^{+0.1}_{-0.1}$	$1.5^{+0.1}_{-0.1}$	1.0	
				you	$17.9^{+3.4}_{-2.9}$	28^{+5}_{-4}	$2.2^{+0.1}_{-0.1}$	1.0	45^{+6}_{-14}
		CIGALE	10.5 ± 0.2	old	1519^{+6492}_{-1231}	2.8 ± 1.6	$1.5^{+0.7}_{-0.7}$	1.0	
				you	20.0	33^{+29}_{-15}	2.2 ± 0.3	1.0	42 ± 29

Continued in the next page

Table5 – continued from previous page

Galaxy	z^\dagger	Code	$\log M_\star$ [M_\odot]	Pop.	τ old [Myr] you [Gyr]	Age old [Gyr] you [Myr]	A_V [mag]	Z [Z_\odot]	b [%]
(1)	(2)	(3)	(4)	(5)	(6)	(7)	(8)	(9)	(10)
MIPS0004309A	1.1720	Synthesizer	$11.2^{+0.1}_{-0.1}$	old	209^{+54}_{-77}	$1.0^{+0.3}_{-0.1}$	$1.3^{+0.2}_{-0.2}$	1.0	
				you	$18.1^{+3.3}_{-3.0}$	81^{+21}_{-27}	$1.3^{+0.1}_{-0.1}$	1.0	12^{+4}_{-2}
		CIGALE	11.2 ± 0.1	old	1961^{+7547}_{-1556}	3.0 ± 1.7	$1.0^{+0.7}_{-0.7}$	1.0	
				you	20.0	155^{+380}_{-110}	1.6 ± 0.7	1.0	28 ± 31
MIPS0004442A	1.0700	Synthesizer	$10.4^{+0.1}_{-0.1}$	old	189^{+69}_{-63}	$3.0^{+0.8}_{-0.6}$	$0.0^{+0.1}_{-0.0}$	1.0	
				you	$16.1^{+2.3}_{-1.9}$	95^{+13}_{-13}	$1.8^{+0.1}_{-0.1}$	1.0	59^{+7}_{-8}
		CIGALE	10.5 ± 0.1	old	1218^{+5450}_{-996}	3.3 ± 1.6	$0.9^{+0.6}_{-0.6}$	1.0	
				you	20.0	137^{+167}_{-75}	1.8 ± 0.2	1.0	55 ± 28
MIPS0004467	1.1100	Synthesizer	$10.0^{+0.1}_{-0.1}$	old	119^{+87}_{-24}	$3.3^{+2.0}_{-2.3}$	$0.1^{+1.4}_{-0.1}$	1.0	
				you	$19.4^{+2.7}_{-2.7}$	28^{+9}_{-9}	$2.0^{+0.1}_{-0.1}$	1.0	70^{+1}_{-6}
		CIGALE	10.1 ± 0.2	old	1259^{+5693}_{-1031}	3.2 ± 1.6	$1.1^{+0.7}_{-0.7}$	1.0	
				you	20.0	38^{+26}_{-15}	1.9 ± 0.1	1.0	59 ± 27
MIPS0004558A	0.8800	Synthesizer	$11.0^{+0.1}_{-0.1}$	old	240^{+35}_{-41}	$2.1^{+0.5}_{-0.3}$	$0.0^{+0.1}_{-0.0}$	1.0	
				you	$18.3^{+3.2}_{-3.0}$	302^{+82}_{-81}	$1.7^{+0.1}_{-0.1}$	1.0	55^{+6}_{-14}
		CIGALE	11.1 ± 0.1	old	1136^{+4911}_{-923}	4.6 ± 1.4	$0.8^{+0.6}_{-0.6}$	1.0	
				you	20.0	300^{+354}_{-162}	1.7 ± 0.3	1.0	47 ± 29
MIPS0007062A	1.1100	Synthesizer	$10.3^{+0.1}_{-0.1}$	old	166^{+59}_{-46}	$1.0^{+0.3}_{-0.1}$	$0.1^{+0.2}_{-0.1}$	1.0	
				you	$18.8^{+3.0}_{-3.3}$	8^{+2}_{-3}	$2.1^{+0.1}_{-0.1}$	1.0	15^{+6}_{-5}
		CIGALE	10.3 ± 0.1	old	1035^{+4795}_{-851}	3.3 ± 1.6	$0.9^{+0.6}_{-0.6}$	1.0	
				you	20.0	87^{+77}_{-41}	1.8 ± 0.1	1.0	69 ± 24
MIPS0007112_1	1.0200	Synthesizer	$10.0^{+0.1}_{-0.1}$	old	150^{+76}_{-46}	$1.3^{+0.7}_{-0.3}$	$0.0^{+0.2}_{-0.0}$	1.0	
				you	$17.3^{+3.4}_{-2.5}$	24^{+7}_{-6}	$2.4^{+0.1}_{-0.1}$	1.0	44^{+12}_{-9}
		CIGALE	10.2 ± 0.2	old	1435^{+6152}_{-1164}	2.9 ± 1.6	$1.4^{+0.7}_{-0.7}$	1.0	
				you	20.0	64^{+53}_{-29}	2.3 ± 0.3	1.0	51 ± 28
MIPS0007300_1	1.1500	Synthesizer	$10.2^{+0.1}_{-0.1}$	old	221^{+46}_{-61}	$1.0^{+0.4}_{-0.1}$	$0.1^{+0.2}_{-0.1}$	1.0	
				you	$18.3^{+3.2}_{-3.1}$	9^{+1}_{-1}	$2.1^{+0.1}_{-0.1}$	1.0	31^{+8}_{-9}
		CIGALE	10.1 ± 0.2	old	1284^{+5734}_{-1049}	3.2 ± 1.6	$1.0^{+0.7}_{-0.7}$	1.0	
				you	20.0	25^{+31}_{-14}	1.9 ± 0.2	1.0	57 ± 30
MIPS0007352_1	1.1200	Synthesizer	$10.3^{+0.1}_{-0.1}$	old	175^{+62}_{-49}	$1.0^{+0.3}_{-0.1}$	$0.3^{+0.2}_{-0.2}$	1.0	
				you	$18.3^{+3.3}_{-3.1}$	1^{+0}_{-0}	$2.5^{+0.1}_{-0.1}$	1.0	15^{+4}_{-4}
		CIGALE	10.1 ± 0.2	old	1169^{+5282}_{-957}	3.2 ± 1.6	$1.1^{+0.8}_{-0.8}$	1.0	
				you	20.0	45^{+54}_{-25}	2.2 ± 0.2	1.0	65 ± 28
MIPS0007356A	1.1300	Synthesizer	$10.7^{+0.1}_{-0.1}$	old	196^{+48}_{-51}	$1.6^{+0.4}_{-0.2}$	$0.2^{+0.1}_{-0.1}$	1.0	
				you	$17.6^{+3.6}_{-2.7}$	9^{+2}_{-1}	$3.4^{+0.4}_{-0.3}$	1.0	5^{+1}_{-1}
		CIGALE	10.9 ± 0.2	old	181^{+316}_{-115}	3.1 ± 1.7	$0.0^{+0.0}_{-0.0}$	1.0	
				you	20.0	61^{+93}_{-37}	3.4 ± 0.5	1.0	15 ± 12
MIPS0007593_1	1.1000	Synthesizer	$10.5^{+0.1}_{-0.1}$	old	107^{+74}_{-16}	$1.0^{+0.1}_{-0.1}$	$1.5^{+0.1}_{-0.1}$	1.0	
				you	$18.4^{+3.1}_{-3.1}$	26^{+5}_{-4}	$2.2^{+0.1}_{-0.1}$	1.0	21^{+9}_{-5}
		CIGALE	10.6 ± 0.2	old	1409^{+6144}_{-1146}	3.0 ± 1.6	$1.6^{+0.7}_{-0.7}$	1.0	
				you	20.0	56^{+46}_{-25}	2.3 ± 0.2	1.0	42 ± 29
MIPS0007658_1	1.0800	Synthesizer	$10.3^{+0.1}_{-0.1}$	old	147^{+49}_{-32}	$1.2^{+0.5}_{-0.3}$	$0.0^{+0.1}_{-0.0}$	1.0	
				you	$16.9^{+3.3}_{-2.4}$	79^{+15}_{-15}	$1.7^{+0.1}_{-0.1}$	1.0	63^{+6}_{-9}
		CIGALE	10.4 ± 0.2	old	1209^{+5479}_{-990}	3.3 ± 1.6	$0.9^{+0.6}_{-0.6}$	1.0	
				you	20.0	85^{+80}_{-41}	1.8 ± 0.2	1.0	59 ± 27
MIPS0008171	1.1000	Synthesizer	$11.0^{+0.1}_{-0.1}$	old	121^{+44}_{-24}	$1.5^{+0.3}_{-0.4}$	$0.1^{+0.2}_{-0.1}$	1.0	
				you	$19.0^{+2.8}_{-3.2}$	317^{+91}_{-84}	$2.5^{+0.1}_{-0.1}$	1.0	61^{+5}_{-6}
		CIGALE	11.1 ± 0.2	old	102^{+22}_{-18}	2.8 ± 1.6	$0.1^{+0.3}_{-0.1}$	1.0	
				you	20.0	156^{+212}_{-90}	2.6 ± 0.3	1.0	29 ± 17

Continued in the next page

Table5 – continued from previous page

Galaxy	z^\dagger	Code	$\log M_\star$ [M_\odot]	Pop.	τ old [Myr] you [Gyr]	Age old [Gyr] you [Myr]	A_V [mag]	Z [Z_\odot]	b [%]
(1)	(2)	(3)	(4)	(5)	(6)	(7)	(8)	(9)	(10)
MIPS0008331	1.1300	Synthesizer	$10.5^{+0.1}_{-0.1}$	old	120^{+42}_{-22}	$1.0^{+0.2}_{-0.1}$	$0.0^{+0.1}_{-0.0}$	1.0	
				you	$18.5^{+3.0}_{-3.1}$	54^{+19}_{-16}	$1.8^{+0.1}_{-0.1}$	1.0	44^{+10}_{-13}
		CIGALE	10.7 ± 0.2	old	1152^{+5287}_{-946}	3.3 ± 1.6	$1.0^{+0.6}_{-0.6}$	1.0	
MIPS0008368A	0.8600	Synthesizer	$10.7^{+0.1}_{-0.1}$	old	164^{+64}_{-41}	$2.4^{+1.4}_{-0.5}$	$0.0^{+0.1}_{-0.0}$	1.0	
				you	$17.3^{+3.5}_{-2.6}$	76^{+20}_{-21}	$2.7^{+0.1}_{-0.1}$	1.0	32^{+9}_{-9}
		CIGALE	10.8 ± 0.1	old	274^{+730}_{-199}	4.3 ± 1.6	$0.5^{+0.7}_{-0.5}$	1.0	
MIPS0008471A	1.0960	Synthesizer	$10.9^{+0.1}_{-0.1}$	old	153^{+57}_{-39}	$1.4^{+0.4}_{-0.4}$	$0.1^{+0.2}_{-0.1}$	1.0	
				you	$18.0^{+3.3}_{-3.0}$	9^{+1}_{-1}	$3.1^{+0.3}_{-0.1}$	1.0	11^{+2}_{-1}
		CIGALE	11.0 ± 0.2	old	105^{+40}_{-29}	2.2 ± 1.5	$0.0^{+0.0}_{-0.0}$	1.0	
MIPS0008576_1	1.1000	Synthesizer	$10.4^{+0.1}_{-0.1}$	old	107^{+26}_{-15}	$1.0^{+0.2}_{-0.1}$	$0.0^{+0.1}_{-0.0}$	1.0	
				you	$17.6^{+3.5}_{-2.7}$	27^{+8}_{-8}	$3.0^{+0.1}_{-0.1}$	1.0	36^{+6}_{-6}
		CIGALE	10.5 ± 0.1	old	100^{+0}_{-0}	1.2 ± 0.7	$0.1^{+0.2}_{-0.1}$	1.0	
MIPS0008647	0.8052	Synthesizer	$10.8^{+0.2}_{-0.1}$	old	220^{+46}_{-88}	$2.1^{+2.0}_{-0.3}$	$0.0^{+0.1}_{-0.0}$	1.0	
				you	$17.6^{+3.5}_{-2.6}$	8^{+1}_{-3}	$1.7^{+0.1}_{-0.1}$	1.0	8^{+3}_{-3}
		CIGALE	10.5 ± 0.2	old	1356^{+6096}_{-1110}	4.1 ± 1.6	$0.8^{+0.6}_{-0.6}$	1.0	
MIPS0008710A	1.0500	Synthesizer	$11.1^{+0.1}_{-0.1}$	old	188^{+57}_{-83}	$3.3^{+1.0}_{-1.5}$	$0.0^{+0.1}_{-0.0}$	1.0	
				you	$16.7^{+3.4}_{-2.2}$	205^{+40}_{-24}	$1.7^{+0.1}_{-0.1}$	1.0	41^{+11}_{-5}
		CIGALE	11.1 ± 0.1	old	738^{+3273}_{-602}	3.9 ± 1.2	$0.8^{+0.6}_{-0.6}$	1.0	
MIPS0008752A	0.9500	Synthesizer	$10.5^{+0.1}_{-0.1}$	old	211^{+51}_{-73}	$2.0^{+0.4}_{-0.2}$	$0.1^{+0.1}_{-0.1}$	1.0	
				you	$18.7^{+3.0}_{-3.2}$	63^{+32}_{-27}	$2.9^{+0.1}_{-0.1}$	1.0	51^{+14}_{-16}
		CIGALE	10.6 ± 0.1	old	355^{+1359}_{-281}	3.2 ± 1.0	$0.7^{+0.9}_{-0.7}$	1.0	
MIPS0008856	0.8770	Synthesizer	$10.4^{+0.1}_{-0.1}$	old	212^{+50}_{-48}	$2.0^{+0.3}_{-0.2}$	$0.0^{+0.1}_{-0.0}$	1.0	
				you	$19.0^{+2.8}_{-2.9}$	48^{+25}_{-16}	$2.8^{+0.1}_{-0.1}$	1.0	31^{+12}_{-10}
		CIGALE	10.6 ± 0.1	old	282^{+821}_{-210}	4.1 ± 1.6	$0.5^{+0.7}_{-0.5}$	1.0	
MIPS0008916	1.0400	Synthesizer	$10.0^{+0.1}_{-0.1}$	old	212^{+51}_{-69}	$1.1^{+0.5}_{-0.1}$	$0.5^{+0.2}_{-0.4}$	1.0	
				you	$18.2^{+3.2}_{-3.0}$	10^{+2}_{-1}	$2.8^{+0.4}_{-0.2}$	1.0	16^{+5}_{-2}
		CIGALE	10.2 ± 0.1	old	766^{+3583}_{-631}	3.4 ± 1.6	$1.2^{+0.8}_{-0.8}$	1.0	
MIPS0008918_1	0.9500	Synthesizer	$10.9^{+0.1}_{-0.1}$	old	241^{+34}_{-58}	$2.0^{+0.2}_{-0.2}$	$1.3^{+0.2}_{-0.2}$	1.0	
				you	$18.6^{+3.0}_{-3.2}$	86^{+23}_{-24}	$2.6^{+0.1}_{-0.1}$	1.0	25^{+6}_{-5}
		CIGALE	10.9 ± 0.1	old	1074^{+4727}_{-875}	3.4 ± 0.9	$1.5^{+0.8}_{-0.8}$	1.0	
MIPS0009017	1.1000	Synthesizer	$10.8^{+0.1}_{-0.1}$	old	115^{+97}_{-21}	$2.2^{+1.1}_{-0.4}$	$0.8^{+0.2}_{-0.2}$	1.0	
				you	$18.3^{+3.1}_{-3.0}$	33^{+15}_{-9}	$2.4^{+0.1}_{-0.1}$	1.0	15^{+5}_{-5}
		CIGALE	10.9 ± 0.2	old	1358^{+5960}_{-1106}	3.8 ± 1.3	$1.4^{+0.8}_{-0.8}$	1.0	
				you	20.0	142^{+223}_{-87}	2.5 ± 0.5	1.0	39 ± 30

Continued in the next page

Table5 – continued from previous page

Galaxy	z^\dagger	Code	$\log M_\star$ [M_\odot]	Pop.	τ old [Myr] you [Gyr]	Age old [Gyr] you [Myr]	A_V [mag]	Z [Z_\odot]	b [%]
(1)	(2)	(3)	(4)	(5)	(6)	(7)	(8)	(9)	(10)
MIPS0009335A	1.1100	Synthesizer	$10.2^{+0.1}_{-0.1}$	old	124^{+48}_{-24}	$1.1^{+0.4}_{-0.2}$	$0.0^{+0.1}_{-0.0}$	1.0	56^{+9}_{-9}
				you	$15.8^{+2.1}_{-1.7}$	54^{+12}_{-12}	$2.3^{+0.1}_{-0.1}$		
		CIGALE	10.5 ± 0.1	old	695^{+3384}_{-577}	3.3 ± 1.6	$1.1^{+0.8}_{-0.8}$	1.0	
MIPS0009527_1	1.1900	Synthesizer	$10.6^{+0.1}_{-0.1}$	old	102^{+15}_{-12}	$1.0^{+0.1}_{-0.1}$	$0.6^{+0.1}_{-0.2}$	1.0	44^{+12}_{-12}
				you	$19.3^{+2.7}_{-2.7}$	61^{+25}_{-21}	$3.4^{+0.2}_{-0.1}$		
		CIGALE	10.8 ± 0.1	old	100^{+0}_{-0}	2.5 ± 1.6	$0.3^{+0.4}_{-0.3}$	1.0	
MIPS0009550_1	1.1100	Synthesizer	$10.8^{+0.1}_{-0.1}$	old	111^{+31}_{-18}	$1.1^{+0.4}_{-0.1}$	$0.4^{+0.1}_{-0.2}$	1.0	30^{+11}_{-11}
				you	$18.3^{+3.3}_{-3.0}$	55^{+27}_{-25}	$3.2^{+0.1}_{-0.1}$		
		CIGALE	10.9 ± 0.1	old	100^{+0}_{-0}	2.2 ± 1.6	$0.2^{+0.3}_{-0.2}$	1.0	
MIPS0010952A	0.8850	Synthesizer	$10.9^{+0.1}_{-0.1}$	old	229^{+39}_{-74}	$2.8^{+0.8}_{-0.8}$	$0.0^{+0.1}_{-0.0}$	1.0	16^{+5}_{-4}
				you	$18.6^{+3.1}_{-3.0}$	16^{+5}_{-2}	$2.5^{+0.1}_{-0.1}$		
		CIGALE	10.9 ± 0.1	old	868^{+3885}_{-709}	4.1 ± 1.6	$1.1^{+0.8}_{-0.8}$	1.0	
MIPS0011090A	0.9000	Synthesizer	$10.9^{+0.1}_{-0.1}$	old	164^{+65}_{-55}	$2.2^{+1.1}_{-0.3}$	$0.6^{+0.2}_{-0.2}$	1.0	60 ± 28
				you	$18.2^{+3.2}_{-3.0}$	86^{+16}_{-20}	$1.7^{+0.1}_{-0.1}$		
		CIGALE	11.0 ± 0.2	old	1550^{+6641}_{-1257}	4.2 ± 1.6	$1.0^{+0.7}_{-0.7}$	1.0	
MIPS0011318_1	1.0900	Synthesizer	$10.5^{+0.2}_{-0.1}$	old	131^{+51}_{-28}	$1.0^{+0.1}_{-0.1}$	$0.2^{+0.7}_{-0.2}$	1.0	45^{+10}_{-15}
				you	$18.8^{+3.0}_{-3.2}$	33^{+18}_{-8}	$2.3^{+0.1}_{-0.2}$		
		CIGALE	10.7 ± 0.2	old	1220^{+5596}_{-1002}	3.1 ± 1.6	$1.4^{+0.7}_{-0.7}$	1.0	
MIPS0011415A	0.9700	Synthesizer	$10.2^{+0.1}_{-0.1}$	old	243^{+35}_{-47}	$2.2^{+1.3}_{-0.4}$	$0.0^{+0.1}_{-0.0}$	1.0	69^{+2}_{-4}
				you	$16.4^{+3.0}_{-2.1}$	41^{+6}_{-6}	$2.3^{+0.0}_{-0.1}$		
		CIGALE	10.3 ± 0.1	old	1161^{+5284}_{-952}	3.1 ± 1.0	$1.2^{+0.8}_{-0.8}$	1.0	
MIPS0011497	1.1000	Synthesizer	$11.0^{+0.1}_{-0.1}$	old	165^{+64}_{-26}	$1.0^{+0.3}_{-0.1}$	$0.1^{+0.1}_{-0.1}$	1.0	70^{+1}_{-2}
				you	$19.7^{+2.6}_{-2.4}$	562^{+130}_{-92}	$3.9^{+0.2}_{-0.4}$		
		CIGALE	11.1 ± 0.1	old	119^{+98}_{-54}	3.2 ± 1.6	$0.3^{+0.4}_{-0.3}$	1.0	
MIPS0015031A	1.1400	Synthesizer	$11.0^{+0.1}_{-0.1}$	old	116^{+33}_{-21}	$1.0^{+0.2}_{-0.1}$	$0.2^{+0.1}_{-0.1}$	1.0	23^{+7}_{-8}
				you	$19.2^{+2.6}_{-3.1}$	66^{+25}_{-28}	$3.2^{+0.4}_{-0.2}$		
		CIGALE	11.2 ± 0.2	old	100^{+0}_{-0}	1.8 ± 1.4	$0.1^{+0.2}_{-0.1}$	1.0	
MIPS0015211A	0.8700	Synthesizer	$11.0^{+0.1}_{-0.1}$	old	156^{+73}_{-57}	$2.0^{+0.3}_{-0.2}$	$0.2^{+0.1}_{-0.1}$	1.0	15^{+5}_{-5}
				you	$18.7^{+2.8}_{-3.2}$	66^{+27}_{-24}	$2.0^{+0.1}_{-0.1}$		
		CIGALE	11.2 ± 0.1	old	1181^{+4942}_{-953}	4.7 ± 1.4	$1.0^{+0.7}_{-0.7}$	1.0	
MIPS0015678_1	1.1100	Synthesizer	$9.9^{+0.1}_{-0.1}$	old	157^{+56}_{-33}	$1.0^{+0.1}_{-0.1}$	$0.1^{+0.3}_{-0.1}$	1.0	54^{+6}_{-9}
				you	$17.8^{+3.3}_{-2.8}$	10^{+1}_{-1}	$2.6^{+0.1}_{-0.1}$		
		CIGALE	10.0 ± 0.2	old	1032^{+4785}_{-849}	3.3 ± 1.6	$1.3^{+0.8}_{-0.8}$	1.0	
MIPS0015694A	1.1900	Synthesizer	$10.4^{+0.1}_{-0.1}$	old	217^{+50}_{-59}	$1.1^{+0.5}_{-0.1}$	$0.9^{+0.3}_{-0.3}$	1.0	26^{+5}_{-5}
				you	$18.5^{+3.0}_{-3.0}$	2^{+1}_{-0}	$2.1^{+0.1}_{-0.1}$		
		CIGALE	10.7 ± 0.1	old	2722^{+8488}_{-2061}	2.8 ± 1.4	$1.2^{+0.5}_{-0.5}$	1.0	
				you	20.0	1^{+0}_{-0}	1.9 ± 0.1	1.0	9 ± 3

Continued in the next page

Table5 – continued from previous page

Galaxy	z^\dagger	Code	$\log M_\star$ [M_\odot]	Pop.	τ old [Myr] you [Gyr]	Age old [Gyr] you [Myr]	A_V [mag]	Z [Z_\odot]	b [%]
(1)	(2)	(3)	(4)	(5)	(6)	(7)	(8)	(9)	(10)
MIPS0015703	1.0900	Synthesizer	$11.2^{+0.1}_{-0.1}$	old	145^{+70}_{-38}	$1.8^{+1.2}_{-0.4}$	$0.2^{+0.1}_{-0.1}$	1.0	
				you	$17.7^{+3.4}_{-2.9}$	261^{+68}_{-70}	$3.3^{+0.2}_{-0.2}$	1.0	41^{+5}_{-5}
		CIGALE	11.3 ± 0.1	old	100^{+0}_{-0}	3.9 ± 1.1	$0.1^{+0.2}_{-0.1}$	1.0	
				you	20.0	246^{+287}_{-132}	3.0 ± 0.1	1.0	28 ± 14
MIPS0015828_1	0.9617	Synthesizer	$11.0^{+0.1}_{-0.1}$	old	215^{+47}_{-97}	$2.3^{+2.0}_{-0.4}$	$0.5^{+0.3}_{-0.4}$	1.0	
				you	$19.3^{+2.7}_{-2.9}$	340^{+85}_{-67}	$2.6^{+0.1}_{-0.1}$	1.0	67^{+4}_{-3}
		CIGALE	11.0 ± 0.1	old	363^{+1328}_{-285}	3.5 ± 0.9	$1.0^{+0.8}_{-0.8}$	1.0	
				you	20.0	252^{+271}_{-131}	2.6 ± 0.2	1.0	50 ± 26
MIPS0016374	0.8200	Synthesizer	$10.8^{+0.1}_{-0.1}$	old	159^{+35}_{-28}	$2.0^{+0.3}_{-0.2}$	$0.0^{+0.1}_{-0.0}$	1.0	
				you	$17.3^{+3.5}_{-2.5}$	44^{+20}_{-19}	$3.4^{+0.1}_{-0.1}$	1.0	35^{+7}_{-11}
		CIGALE	11.0 ± 0.1	old	186^{+332}_{-119}	4.1 ± 1.8	$0.1^{+0.2}_{-0.1}$	1.0	
				you	20.0	68^{+86}_{-38}	3.3 ± 0.2	1.0	26 ± 19
MIPS0016401A	0.9200	Synthesizer	$10.2^{+0.1}_{-0.1}$	old	229^{+42}_{-45}	$2.0^{+0.3}_{-0.2}$	$0.0^{+0.1}_{-0.0}$	1.0	
				you	$18.9^{+2.9}_{-3.2}$	17^{+7}_{-3}	$3.0^{+0.1}_{-0.1}$	1.0	32^{+8}_{-3}
		CIGALE	10.4 ± 0.1	old	188^{+336}_{-120}	4.0 ± 1.6	$0.0^{+0.1}_{-0.0}$	1.0	
				you	20.0	16^{+15}_{-8}	3.0 ± 0.3	1.0	20 ± 17
MIPS0016731	0.8701	Synthesizer	$10.5^{+0.1}_{-0.1}$	old	221^{+47}_{-98}	$2.0^{+0.4}_{-0.2}$	$0.0^{+0.1}_{-0.0}$	1.0	
				you	$16.5^{+3.2}_{-2.1}$	9^{+1}_{-1}	$2.5^{+0.1}_{-0.1}$	1.0	21^{+5}_{-2}
		CIGALE	10.5 ± 0.2	old	1324^{+5660}_{-1073}	4.1 ± 1.6	$0.9^{+0.8}_{-0.8}$	1.0	
				you	20.0	29^{+42}_{-17}	2.4 ± 0.4	1.0	53 ± 35
MIPS0016798A	0.7612	Synthesizer	$10.2^{+0.1}_{-0.1}$	old	112^{+130}_{-18}	$3.1^{+0.8}_{-0.4}$	$0.0^{+0.1}_{-0.0}$	1.0	
				you	$19.9^{+2.5}_{-2.2}$	10^{+1}_{-1}	$1.9^{+0.1}_{-0.1}$	1.0	52^{+16}_{-15}
		CIGALE	10.3 ± 0.3	old	1205^{+5594}_{-991}	4.1 ± 1.0	$0.9^{+0.6}_{-0.6}$	1.0	
				you	20.0	15^{+9}_{-6}	1.7 ± 0.3	1.0	43 ± 31
MIPS0018398	0.9600	Synthesizer	$10.5^{+0.1}_{-0.1}$	old	213^{+52}_{-89}	$2.6^{+0.7}_{-0.7}$	$0.3^{+0.2}_{-0.1}$	1.0	
				you	$17.8^{+3.3}_{-2.8}$	9^{+1}_{-1}	$3.8^{+0.2}_{-0.1}$	1.0	10^{+1}_{-1}
		CIGALE	10.5 ± 0.1	old	100^{+0}_{-0}	2.8 ± 1.0	$0.0^{+0.0}_{-0.0}$	1.0	
				you	20.0	31^{+49}_{-19}	3.6 ± 0.3	1.0	17 ± 12
MIPS0018604	0.8000	Synthesizer	$10.7^{+0.1}_{-0.1}$	old	233^{+40}_{-86}	$3.1^{+0.5}_{-0.4}$	$0.1^{+0.1}_{-0.1}$	1.0	
				you	$19.4^{+2.6}_{-2.7}$	73^{+18}_{-19}	$3.0^{+0.1}_{-0.1}$	1.0	25^{+5}_{-5}
		CIGALE	10.9 ± 0.1	old	272^{+580}_{-185}	4.4 ± 0.9	$0.0^{+0.1}_{-0.0}$	1.0	
				you	20.0	117^{+177}_{-70}	3.2 ± 0.5	1.0	23 ± 15
MIPS0018747	1.1000	Synthesizer	$11.1^{+0.1}_{-0.1}$	old	142^{+48}_{-41}	$1.4^{+0.2}_{-0.4}$	$0.1^{+0.1}_{-0.1}$	1.0	
				you	$19.5^{+2.7}_{-2.9}$	407^{+83}_{-73}	$2.7^{+0.2}_{-0.1}$	1.0	60^{+4}_{-5}
		CIGALE	11.2 ± 0.2	old	100^{+0}_{-0}	2.7 ± 1.6	$0.1^{+0.3}_{-0.1}$	1.0	
				you	20.0	167^{+237}_{-98}	3.0 ± 0.4	1.0	35 ± 17
MIPS0019123	0.8800	Synthesizer	$10.6^{+0.1}_{-0.1}$	old	159^{+70}_{-44}	$3.0^{+0.6}_{-0.7}$	$0.1^{+0.1}_{-0.1}$	1.0	
				you	$18.3^{+3.2}_{-3.0}$	10^{+1}_{-1}	$4.0^{+0.1}_{-0.2}$	1.0	11^{+1}_{-1}
		CIGALE	10.5 ± 0.1	old	104^{+38}_{-28}	2.4 ± 0.9	$0.0^{+0.0}_{-0.0}$	1.0	
				you	20.0	11^{+5}_{-4}	3.9 ± 0.2	1.0	9 ± 3
MIPS0019351_1	1.0800	Synthesizer	$10.3^{+0.1}_{-0.1}$	old	128^{+29}_{-22}	$1.5^{+0.2}_{-0.3}$	$0.3^{+0.2}_{-0.1}$	1.0	
				you	$17.3^{+3.4}_{-2.5}$	45^{+12}_{-10}	$2.4^{+0.1}_{-0.1}$	1.0	55^{+7}_{-10}
		CIGALE	10.6 ± 0.2	old	1261^{+5625}_{-1030}	3.2 ± 1.6	$1.3^{+0.7}_{-0.7}$	1.0	
				you	20.0	94^{+135}_{-56}	2.3 ± 0.2	1.0	53 ± 30

Continued in the next page

Table5 – continued from previous page

Galaxy	z^\dagger	Code	$\log M_\star$ [M_\odot]	Pop.	τ old [Myr] you [Gyr]	Age old [Gyr] you [Myr]	A_V [mag]	Z [Z_\odot]	b [%]
(1)	(2)	(3)	(4)	(5)	(6)	(7)	(8)	(9)	(10)
MIPS0019961A	1.1600	Synthesizer	$10.5^{+0.1}_{-0.1}$	old	105^{+30}_{-14}	$1.3^{+0.4}_{-0.3}$	$0.0^{+0.1}_{-0.0}$	1.0	
				you	$17.3^{+3.4}_{-2.6}$	47^{+13}_{-12}	$3.2^{+0.1}_{-0.1}$	1.0	60^{+6}_{-10}
		CIGALE	10.8 ± 0.1	old	319^{+1280}_{-255}	3.4 ± 1.6	$1.0^{+1.0}_{-1.0}$	1.0	
				you	20.0	174^{+192}_{-91}	2.8 ± 0.2	1.0	63 ± 26
MIPS0021138	0.9300	Synthesizer	$10.6^{+0.1}_{-0.1}$	old	240^{+36}_{-41}	$2.0^{+0.2}_{-0.2}$	$0.0^{+0.1}_{-0.0}$	1.0	
				you	$19.2^{+2.6}_{-2.9}$	40^{+19}_{-11}	$2.8^{+0.1}_{-0.1}$	1.0	24^{+7}_{-5}
		CIGALE	10.7 ± 0.1	old	145^{+194}_{-83}	3.6 ± 1.7	$0.0^{+0.0}_{-0.0}$	1.0	
				you	20.0	71^{+93}_{-40}	2.6 ± 0.1	1.0	25 ± 19
MIPS0021384A	0.9200	Synthesizer	$11.0^{+0.1}_{-0.1}$	old	229^{+43}_{-80}	$2.0^{+0.5}_{-0.2}$	$0.2^{+0.2}_{-0.1}$	1.0	
				you	$18.4^{+3.1}_{-3.2}$	607^{+112}_{-94}	$2.5^{+0.1}_{-0.1}$	1.0	66^{+4}_{-3}
		CIGALE	11.2 ± 0.1	old	215^{+420}_{-142}	4.7 ± 1.6	$0.2^{+0.3}_{-0.2}$	1.0	
				you	20.0	269^{+434}_{-166}	2.6 ± 0.2	1.0	31 ± 17
MIPS0021666_2	1.1100	Synthesizer	$10.0^{+0.1}_{-0.1}$	old	126^{+42}_{-27}	$1.4^{+0.3}_{-0.4}$	$0.0^{+0.2}_{-0.0}$	1.0	
				you	$19.1^{+2.8}_{-3.1}$	20^{+11}_{-5}	$2.3^{+0.1}_{-0.1}$	1.0	40^{+9}_{-10}
		CIGALE	10.2 ± 0.2	old	1078^{+5020}_{-888}	3.2 ± 1.6	$1.4^{+0.7}_{-0.7}$	1.0	
				you	20.0	74^{+53}_{-31}	2.2 ± 0.1	1.0	59 ± 28
MIPS0021759	1.1200	Synthesizer	$10.5^{+0.1}_{-0.1}$	old	109^{+23}_{-16}	$1.0^{+0.1}_{-0.1}$	$0.4^{+0.2}_{-0.2}$	1.0	
				you	$18.6^{+2.9}_{-3.2}$	32^{+12}_{-7}	$3.0^{+0.1}_{-0.1}$	1.0	38^{+12}_{-8}
		CIGALE	10.8 ± 0.1	old	380^{+1694}_{-310}	3.1 ± 1.7	$1.1^{+1.0}_{-1.0}$	1.0	
				you	20.0	150^{+155}_{-76}	2.8 ± 0.1	1.0	65 ± 25
MIPS0022002	1.1200	Synthesizer	$10.8^{+0.1}_{-0.1}$	old	131^{+90}_{-33}	$1.0^{+0.4}_{-0.1}$	$1.3^{+0.2}_{-0.5}$	1.0	
				you	$17.9^{+3.5}_{-2.8}$	86^{+17}_{-23}	$1.7^{+0.1}_{-0.1}$	1.0	41^{+10}_{-10}
		CIGALE	10.9 ± 0.2	old	1410^{+6209}_{-1149}	3.3 ± 1.6	$1.0^{+0.6}_{-0.6}$	1.0	
				you	20.0	110^{+140}_{-62}	1.7 ± 0.4	1.0	37 ± 29
MIPS0022211_1	0.9100	Synthesizer	$10.7^{+0.1}_{-0.1}$	old	157^{+25}_{-22}	$2.9^{+0.4}_{-0.8}$	$0.0^{+0.1}_{-0.0}$	1.0	
				you	$16.5^{+3.1}_{-2.1}$	67^{+17}_{-16}	$2.5^{+0.1}_{-0.1}$	1.0	30^{+6}_{-5}
		CIGALE	10.8 ± 0.1	old	374^{+1266}_{-289}	4.3 ± 1.5	$0.6^{+0.8}_{-0.6}$	1.0	
				you	20.0	144^{+180}_{-80}	2.5 ± 0.3	1.0	51 ± 30
MIPS0022445A	1.1600	Synthesizer	$10.9^{+0.1}_{-0.1}$	old	108^{+26}_{-16}	$1.0^{+0.2}_{-0.1}$	$0.2^{+0.1}_{-0.1}$	1.0	
				you	$18.6^{+3.1}_{-3.1}$	67^{+23}_{-24}	$2.1^{+0.1}_{-0.1}$	1.0	31^{+9}_{-8}
		CIGALE	11.1 ± 0.1	old	578^{+2610}_{-473}	3.8 ± 1.4	$0.9^{+0.7}_{-0.7}$	1.0	
				you	20.0	252^{+242}_{-123}	2.0 ± 0.1	1.0	58 ± 27
MIPS0022836	0.7100	Synthesizer	$11.1^{+0.1}_{-0.1}$	old	102^{+18}_{-11}	$6.0^{+0.8}_{-0.7}$	$1.5^{+0.1}_{-0.1}$	1.0	
				you	$19.5^{+2.6}_{-2.7}$	541^{+91}_{-75}	$2.4^{+0.1}_{-0.1}$	1.0	70^{+1}_{-4}
		CIGALE	11.1 ± 0.1	old	3397^{+9055}_{-2471}	5.2 ± 1.5	$1.4^{+1.4}_{-1.4}$	1.0	
				you	20.0	203^{+391}_{-134}	2.9 ± 0.8	1.0	38 ± 29
MIPS0023305_1	0.9300	Synthesizer	$10.1^{+0.1}_{-0.1}$	old	248^{+32}_{-31}	$2.0^{+0.2}_{-0.2}$	$0.1^{+0.2}_{-0.1}$	1.0	
				you	$19.3^{+2.7}_{-2.9}$	30^{+11}_{-6}	$2.6^{+0.1}_{-0.1}$	1.0	50^{+6}_{-6}
		CIGALE	10.2 ± 0.1	old	1060^{+4821}_{-869}	4.2 ± 1.6	$1.3^{+0.8}_{-0.8}$	1.0	
				you	20.0	101^{+83}_{-46}	2.3 ± 0.1	1.0	64 ± 25
MIPS0024518	1.1100	Synthesizer	$10.2^{+0.1}_{-0.1}$	old	103^{+22}_{-12}	$1.0^{+0.1}_{-0.1}$	$1.5^{+0.1}_{-0.1}$	1.0	
				you	$17.3^{+3.4}_{-2.6}$	17^{+7}_{-3}	$2.3^{+0.1}_{-0.1}$	1.0	42^{+18}_{-7}
		CIGALE	10.2 ± 0.2	old	1446^{+6432}_{-1181}	3.0 ± 1.6	$1.3^{+0.9}_{-0.9}$	1.0	
				you	20.0	28^{+12}_{-8}	2.3 ± 0.4	1.0	52 ± 27
MIPS0024714A	1.1200	Synthesizer	$10.8^{+0.1}_{-0.1}$	old	113^{+41}_{-20}	$1.0^{+0.1}_{-0.1}$	$0.7^{+0.1}_{-0.1}$	1.0	
				you	$18.7^{+3.0}_{-3.1}$	72^{+21}_{-25}	$2.0^{+0.1}_{-0.1}$	1.0	25^{+5}_{-6}
		CIGALE	10.9 ± 0.1	old	1072^{+5094}_{-886}	3.3 ± 1.6	$1.1^{+0.7}_{-0.7}$	1.0	
				you	20.0	195^{+299}_{-118}	2.0 ± 0.2	1.0	53 ± 31

Continued in the next page

Table5 – continued from previous page

Galaxy	z^\dagger	Code	$\log M_\star$ [M_\odot]	Pop.	τ old [Myr] you [Gyr]	Age old [Gyr] you [Myr]	A_V [mag]	Z [Z_\odot]	b [%]
(1)	(2)	(3)	(4)	(5)	(6)	(7)	(8)	(9)	(10)
MIPS0024996A	1.1807	Synthesizer	$10.7^{+0.1}_{-0.1}$	old	133^{+41}_{-30}	$1.0^{+0.1}_{-0.1}$	$0.3^{+0.1}_{-0.1}$	1.0	
				you	$18.1^{+3.2}_{-3.0}$	45^{+25}_{-17}	$2.1^{+0.1}_{-0.1}$	1.0	26^{+10}_{-7}
		CIGALE	10.9 ± 0.1	old	952^{+4542}_{-787}	3.4 ± 1.5	$1.0^{+0.7}_{-0.7}$	1.0	
				you	20.0	195^{+266}_{-113}	2.0 ± 0.2	1.0	55 ± 30
MIPS0025409A	1.2400	Synthesizer	$10.3^{+0.1}_{-0.1}$	old	235^{+38}_{-43}	$1.0^{+0.1}_{-0.1}$	$0.3^{+0.4}_{-0.2}$	1.0	
				you	$18.2^{+3.3}_{-3.1}$	60^{+25}_{-21}	$2.3^{+0.2}_{-0.1}$	1.0	51^{+10}_{-11}
		CIGALE	10.5 ± 0.1	old	1423^{+5962}_{-1149}	2.2 ± 1.0	$1.2^{+0.7}_{-0.7}$	1.0	
				you	20.0	123^{+210}_{-77}	2.1 ± 0.4	1.0	48 ± 31
MIPS0025572A	1.1000	Synthesizer	$10.8^{+0.1}_{-0.1}$	old	151^{+50}_{-45}	$1.5^{+0.4}_{-0.2}$	$0.0^{+0.1}_{-0.0}$	1.0	
				you	$17.4^{+3.5}_{-2.7}$	21^{+15}_{-6}	$3.1^{+0.1}_{-0.1}$	1.0	21^{+9}_{-5}
		CIGALE	10.9 ± 0.2	old	100^{+0}_{-0}	1.9 ± 1.4	$0.0^{+0.1}_{-0.0}$	1.0	
				you	20.0	58^{+57}_{-29}	3.3 ± 0.4	1.0	33 ± 18
MIPS0025717A	0.8500	Synthesizer	$10.8^{+0.1}_{-0.1}$	old	151^{+59}_{-32}	$2.0^{+0.3}_{-0.2}$	$0.1^{+0.1}_{-0.1}$	1.0	
				you	$17.6^{+3.4}_{-2.7}$	43^{+19}_{-17}	$2.8^{+0.1}_{-0.1}$	1.0	31^{+10}_{-11}
		CIGALE	11.0 ± 0.1	old	690^{+2995}_{-561}	4.3 ± 1.5	$1.3^{+0.9}_{-0.9}$	1.0	
				you	20.0	200^{+176}_{-94}	2.7 ± 0.2	1.0	60 ± 27
MIPS0025946	1.1800	Synthesizer	$10.5^{+0.1}_{-0.1}$	old	113^{+62}_{-19}	$1.1^{+0.5}_{-0.2}$	$0.3^{+0.2}_{-0.2}$	1.0	
				you	$17.2^{+3.4}_{-2.5}$	70^{+15}_{-14}	$2.1^{+0.0}_{-0.1}$	1.0	67^{+4}_{-6}
		CIGALE	10.6 ± 0.1	old	1075^{+4981}_{-884}	3.2 ± 1.6	$1.1^{+0.7}_{-0.7}$	1.0	
				you	20.0	108^{+95}_{-50}	2.0 ± 0.1	1.0	59 ± 27
MIPS0027542A	0.9800	Synthesizer	$10.4^{+0.1}_{-0.1}$	old	238^{+37}_{-72}	$2.0^{+0.3}_{-0.2}$	$0.1^{+0.2}_{-0.1}$	1.0	
				you	$18.0^{+3.3}_{-3.0}$	10^{+2}_{-1}	$3.1^{+0.1}_{-0.1}$	1.0	16^{+4}_{-4}
		CIGALE	10.5 ± 0.1	old	300^{+1063}_{-234}	3.2 ± 1.0	$0.7^{+0.9}_{-0.7}$	1.0	
				you	20.0	114^{+112}_{-56}	2.8 ± 0.2	1.0	59 ± 28
MIPS0027595A	0.7000	Synthesizer	$11.2^{+0.1}_{-0.1}$	old	202^{+38}_{-33}	$3.1^{+1.2}_{-0.4}$	$0.2^{+0.1}_{-0.1}$	1.0	
				you	$17.9^{+3.4}_{-2.9}$	402^{+91}_{-81}	$2.5^{+0.1}_{-0.1}$	1.0	57^{+4}_{-5}
		CIGALE	11.3 ± 0.1	old	810^{+3020}_{-639}	5.5 ± 1.5	$1.0^{+0.8}_{-0.8}$	1.0	
				you	20.0	372^{+443}_{-202}	2.5 ± 0.4	1.0	44 ± 27
MIPS0029054	1.0910	Synthesizer	$10.8^{+0.1}_{-0.1}$	old	116^{+42}_{-21}	$1.0^{+0.3}_{-0.1}$	$0.2^{+0.1}_{-0.1}$	1.0	
				you	$18.5^{+3.1}_{-3.0}$	64^{+23}_{-25}	$1.9^{+0.1}_{-0.1}$	1.0	25^{+6}_{-9}
		CIGALE	11.1 ± 0.1	old	734^{+3337}_{-601}	3.9 ± 1.2	$0.9^{+0.6}_{-0.6}$	1.0	
				you	20.0	324^{+322}_{-162}	1.7 ± 0.1	1.0	52 ± 28
MIPS0029170A	1.2100	Synthesizer	$10.7^{+0.1}_{-0.1}$	old	117^{+49}_{-22}	$1.0^{+0.2}_{-0.1}$	$0.8^{+0.1}_{-0.1}$	1.0	
				you	$18.9^{+2.8}_{-3.2}$	46^{+28}_{-18}	$2.6^{+0.1}_{-0.1}$	1.0	26^{+10}_{-8}
		CIGALE	11.0 ± 0.1	old	604^{+2769}_{-496}	3.7 ± 1.4	$1.2^{+0.8}_{-0.8}$	1.0	
				you	20.0	232^{+301}_{-131}	2.5 ± 0.2	1.0	58 ± 28
MIPS0030478_1	1.1100	Synthesizer	$10.0^{+0.1}_{-0.1}$	old	121^{+21}_{-20}	$1.0^{+0.1}_{-0.1}$	$0.0^{+0.1}_{-0.0}$	1.0	
				you	$18.6^{+3.1}_{-3.2}$	34^{+7}_{-7}	$2.2^{+0.0}_{-0.0}$	1.0	52^{+8}_{-8}
		CIGALE	10.3 ± 0.1	old	1170^{+5411}_{-962}	3.1 ± 1.6	$1.2^{+0.7}_{-0.7}$	1.0	
				you	20.0	118^{+113}_{-58}	2.0 ± 0.2	1.0	58 ± 27
MIPS0031380A	1.1200	Synthesizer	$10.8^{+0.1}_{-0.1}$	old	109^{+23}_{-16}	$1.0^{+0.1}_{-0.1}$	$0.4^{+0.1}_{-0.1}$	1.0	
				you	$19.0^{+2.9}_{-3.2}$	57^{+25}_{-23}	$3.0^{+0.1}_{-0.1}$	1.0	30^{+8}_{-10}
		CIGALE	10.9 ± 0.2	old	100^{+0}_{-0}	2.1 ± 1.5	$0.1^{+0.3}_{-0.1}$	1.0	
				you	20.0	86^{+126}_{-51}	3.0 ± 0.5	1.0	26 ± 17

Continued in the next page

Table5 – continued from previous page

Galaxy	z^\dagger	Code	$\log M_\star$ [M_\odot]	Pop.	τ old [Myr] you [Gyr]	Age old [Gyr] you [Myr]	A_V [mag]	Z [Z_\odot]	b [%]
(1)	(2)	(3)	(4)	(5)	(6)	(7)	(8)	(9)	(10)
MIPS0031422A	1.1200	Synthesizer	$10.7^{+0.1}_{-0.1}$	old	116^{+33}_{-21}	$1.0^{+0.1}_{-0.1}$	$0.7^{+0.1}_{-0.2}$	1.0	
				you	$19.6^{+2.7}_{-2.5}$	60^{+24}_{-22}	$2.8^{+0.1}_{-0.1}$	1.0	29^{+7}_{-9}
		CIGALE	11.0 ± 0.1	old	206^{+394}_{-135}	3.8 ± 1.5	$0.4^{+0.5}_{-0.4}$	1.0	
				you	20.0	331^{+424}_{-186}	2.7 ± 0.4	1.0	42 ± 18
MIPS0032241A	1.1100	Synthesizer	$10.5^{+0.1}_{-0.1}$	old	155^{+36}_{-34}	$1.0^{+0.2}_{-0.1}$	$0.2^{+0.2}_{-0.2}$	1.0	
				you	$17.2^{+3.5}_{-2.5}$	10^{+2}_{-1}	$3.1^{+0.2}_{-0.1}$	1.0	29^{+5}_{-5}
		CIGALE	10.7 ± 0.2	old	415^{+1799}_{-337}	3.0 ± 1.7	$0.8^{+0.9}_{-0.8}$	1.0	
				you	20.0	37^{+84}_{-26}	2.8 ± 0.2	1.0	51 ± 32
MIPS0032586A	1.0500	Synthesizer	$10.4^{+0.2}_{-0.1}$	old	199^{+59}_{-76}	$1.1^{+0.5}_{-0.2}$	$0.1^{+0.1}_{-0.1}$	1.0	
				you	$17.0^{+3.5}_{-2.4}$	7^{+1}_{-2}	$1.3^{+0.1}_{-0.1}$	1.0	10^{+2}_{-4}
		CIGALE	10.2 ± 0.1	old	1320^{+5812}_{-1076}	3.2 ± 1.6	$0.6^{+0.5}_{-0.5}$	1.0	
				you	20.0	55^{+58}_{-28}	1.2 ± 0.2	1.0	62 ± 28
MIPS0032738	1.1500	Synthesizer	$10.6^{+0.1}_{-0.1}$	old	157^{+36}_{-33}	$1.6^{+0.3}_{-0.2}$	$0.2^{+0.1}_{-0.1}$	1.0	
				you	$18.4^{+3.2}_{-3.1}$	75^{+19}_{-22}	$3.6^{+0.1}_{-0.1}$	1.0	36^{+5}_{-6}
		CIGALE	10.9 ± 0.1	old	100^{+0}_{-0}	3.3 ± 1.4	$0.1^{+0.3}_{-0.1}$	1.0	
				you	20.0	108^{+205}_{-71}	3.2 ± 0.2	1.0	27 ± 18
MIPS0033398A	1.0700	Synthesizer	$10.8^{+0.1}_{-0.1}$	old	140^{+68}_{-42}	$1.1^{+0.4}_{-0.2}$	$0.1^{+0.1}_{-0.1}$	1.0	
				you	$18.6^{+3.0}_{-3.2}$	74^{+21}_{-24}	$1.8^{+0.1}_{-0.1}$	1.0	25^{+6}_{-7}
		CIGALE	11.2 ± 0.1	old	729^{+3210}_{-594}	4.0 ± 1.2	$0.8^{+0.5}_{-0.5}$	1.0	
				you	20.0	334^{+308}_{-160}	1.6 ± 0.1	1.0	46 ± 27
MIPS0033408	0.8800	Synthesizer	$10.3^{+0.1}_{-0.1}$	old	229^{+42}_{-66}	$2.7^{+0.7}_{-0.7}$	$0.0^{+0.2}_{-0.0}$	1.0	
				you	$18.5^{+3.0}_{-3.1}$	16^{+4}_{-4}	$2.7^{+0.1}_{-0.1}$	1.0	16^{+5}_{-4}
		CIGALE	10.4 ± 0.1	old	302^{+789}_{-219}	4.1 ± 1.5	$0.2^{+0.6}_{-0.2}$	1.0	
				you	20.0	74^{+100}_{-43}	2.8 ± 0.4	1.0	36 ± 27
MIPS0033690_1	1.1500	Synthesizer	$10.6^{+0.1}_{-0.1}$	old	186^{+32}_{-39}	$1.0^{+0.1}_{-0.1}$	$0.8^{+0.2}_{-0.1}$	1.0	
				you	$20.0^{+2.3}_{-2.3}$	35^{+27}_{-9}	$3.7^{+0.4}_{-0.6}$	1.0	24^{+10}_{-5}
		CIGALE	10.6 ± 0.1	old	103^{+32}_{-24}	1.5 ± 1.2	$0.2^{+0.4}_{-0.2}$	1.0	
				you	20.0	95^{+106}_{-50}	3.3 ± 0.4	1.0	49 ± 19
MIPS0033897	1.0900	Synthesizer	$10.2^{+0.1}_{-0.1}$	old	164^{+41}_{-25}	$1.0^{+0.2}_{-0.1}$	$0.0^{+0.1}_{-0.0}$	1.0	
				you	$18.3^{+3.2}_{-3.1}$	52^{+12}_{-10}	$2.0^{+0.1}_{-0.1}$	1.0	55^{+7}_{-9}
		CIGALE	10.5 ± 0.1	old	1001^{+4704}_{-825}	3.2 ± 1.6	$1.0^{+0.6}_{-0.6}$	1.0	
				you	20.0	138^{+123}_{-65}	1.9 ± 0.1	1.0	63 ± 25
MIPS0034055A	0.8400	Synthesizer	$10.8^{+0.1}_{-0.1}$	old	190^{+69}_{-79}	$2.0^{+0.3}_{-0.2}$	$1.5^{+0.1}_{-0.1}$	1.0	
				you	$16.5^{+3.1}_{-2.1}$	95^{+14}_{-14}	$1.3^{+0.1}_{-0.1}$	1.0	29^{+3}_{-5}
		CIGALE	10.7 ± 0.2	old	1633^{+7013}_{-1325}	4.0 ± 1.6	$0.6^{+0.5}_{-0.5}$	1.0	
				you	20.0	127^{+188}_{-76}	1.3 ± 0.5	1.0	45 ± 30
MIPS0034350A	0.9400	Synthesizer	$10.6^{+0.1}_{-0.1}$	old	181^{+32}_{-44}	$2.1^{+1.6}_{-0.3}$	$0.0^{+0.1}_{-0.0}$	1.0	
				you	$16.2^{+2.5}_{-2.0}$	95^{+14}_{-13}	$2.0^{+0.1}_{-0.1}$	1.0	36^{+5}_{-5}
		CIGALE	10.6 ± 0.1	old	926^{+4165}_{-757}	4.3 ± 1.6	$1.0^{+0.7}_{-0.7}$	1.0	
				you	20.0	158^{+170}_{-82}	2.0 ± 0.2	1.0	63 ± 27
MIPS0034419	0.9700	Synthesizer	$10.5^{+0.1}_{-0.1}$	old	243^{+36}_{-40}	$2.0^{+0.3}_{-0.2}$	$0.5^{+0.2}_{-0.3}$	1.0	
				you	$19.7^{+2.6}_{-2.3}$	60^{+25}_{-24}	$3.0^{+0.1}_{-0.1}$	1.0	36^{+15}_{-11}
		CIGALE	10.6 ± 0.1	old	349^{+1417}_{-280}	3.2 ± 1.0	$1.0^{+1.0}_{-1.0}$	1.0	
				you	20.0	158^{+165}_{-81}	2.8 ± 0.1	1.0	61 ± 27
MIPS0034471	1.0200	Synthesizer	$10.7^{+0.1}_{-0.1}$	old	149^{+54}_{-40}	$1.2^{+0.5}_{-0.2}$	$0.1^{+0.3}_{-0.1}$	1.0	
				you	$18.2^{+3.3}_{-3.0}$	9^{+2}_{-1}	$2.5^{+0.1}_{-0.1}$	1.0	11^{+5}_{-2}
		CIGALE	10.8 ± 0.1	old	501^{+2283}_{-411}	3.3 ± 1.6	$0.8^{+0.8}_{-0.8}$	1.0	
				you	20.0	166^{+187}_{-88}	2.2 ± 0.1	1.0	61 ± 27

Continued in the next page

Table5 – continued from previous page

Galaxy	z^\dagger	Code	$\log M_\star$ [M_\odot]	Pop.	τ old [Myr] you [Gyr]	Age old [Gyr] you [Myr]	A_V [mag]	Z [Z_\odot]	b [%]
(1)	(2)	(3)	(4)	(5)	(6)	(7)	(8)	(9)	(10)
MIPS0034593	1.0200	Synthesizer	$10.3^{+0.1}_{-0.1}$	old	175^{+63}_{-48}	$1.0^{+0.1}_{-0.1}$	$0.3^{+0.1}_{-0.1}$	1.0	
				you	$18.2^{+3.2}_{-3.1}$	29^{+11}_{-9}	$2.0^{+0.1}_{-0.1}$	1.0	31^{+10}_{-10}
		CIGALE	10.6 ± 0.2	old	1729^{+6874}_{-1382}	2.9 ± 1.7	$1.3^{+0.7}_{-0.7}$	1.0	
				you	20.0	72^{+74}_{-36}	2.1 ± 0.5	1.0	34 ± 26
MIPS0034710_1	0.9620	Synthesizer	$10.8^{+0.1}_{-0.1}$	old	165^{+83}_{-55}	$2.6^{+0.6}_{-0.7}$	$0.0^{+0.1}_{-0.0}$	1.0	
				you	$16.7^{+3.3}_{-2.2}$	78^{+25}_{-29}	$3.6^{+0.1}_{-0.1}$	1.0	34^{+6}_{-9}
		CIGALE	10.9 ± 0.1	old	100^{+0}_{-0}	2.7 ± 0.9	$0.0^{+0.0}_{-0.0}$	1.0	
				you	20.0	91^{+113}_{-50}	3.8 ± 0.2	1.0	30 ± 15
MIPS0035194A	0.9300	Synthesizer	$10.8^{+0.1}_{-0.1}$	old	196^{+52}_{-65}	$2.0^{+0.3}_{-0.2}$	$0.1^{+0.3}_{-0.1}$	1.0	
				you	$18.8^{+3.1}_{-3.2}$	77^{+17}_{-19}	$1.7^{+0.1}_{-0.1}$	1.0	44^{+16}_{-13}
		CIGALE	10.8 ± 0.2	old	968^{+4454}_{-795}	4.3 ± 1.6	$0.9^{+0.6}_{-0.6}$	1.0	
				you	20.0	128^{+96}_{-55}	1.7 ± 0.1	1.0	59 ± 27

Table 5: Stellar population synthesis results for complementary-sample dusty starbursts. Median and 1σ error values are shown for each parameter derived with the SYNTHESIZER code. The expected and standard deviation (or upper and lower limits when changing from logarithmic space to linear space) values are quoted for each parameter estimated with the CIGALE. (1) Name of the galaxy. (2) Photometric or spectroscopic redshift (z_{spec} indicated by a †). (3) Code used to derive the parameters. (4) Stellar mass (in solar units) and its uncertainty derived from the logarithmic space. (5) Parameter values for the old or the young population. (6) e -folding time and its uncertainty (old population in Myr and young population in Gyr). (7) Age and its uncertainty (old population in Gyr and young population in Myr). (8) Attenuation in the V -band and its uncertainty in mag. (9) Metallicity value (fixed to the solar value) in solar units. (10) Most recent burst intensity fraction and its uncertainty in percentage.

Galaxy	z^\dagger	Code	$\log M_\star$ [M_\odot]	Pop.	τ old [Myr] you [Gyr]	Age old [Gyr] you [Myr]	A_V [mag]	Z [Z_\odot]	b [%]
(1)	(2)	(3)	(4)	(5)	(6)	(7)	(8)	(9)	(10)
MIPS0000373_1	1.1100	Synthesizer	$10.5^{+0.1}_{-0.1}$	old	121^{+52}_{-25}	$1.0^{+0.1}_{-0.1}$	$0.6^{+0.2}_{-0.3}$	1.0	
				you	$18.5^{+2.9}_{-3.1}$	50^{+30}_{-17}	$2.1^{+0.1}_{-0.1}$	1.0	30^{+12}_{-10}
		CIGALE	10.8 ± 0.1	old	1255^{+5646}_{-1027}	3.7 ± 1.5	$1.1^{+0.6}_{-0.6}$	1.0	
				you	20.0	285^{+402}_{-167}	1.9 ± 0.3	1.0	49 ± 31
MIPS0000814_1	1.1200	Synthesizer	$10.7^{+0.1}_{-0.1}$	old	115^{+42}_{-20}	$1.0^{+0.1}_{-0.1}$	$0.4^{+0.2}_{-0.2}$	1.0	
				you	$18.6^{+2.9}_{-3.1}$	50^{+26}_{-18}	$1.8^{+0.1}_{-0.1}$	1.0	25^{+11}_{-9}
		CIGALE	10.9 ± 0.1	old	1309^{+5897}_{-1071}	3.5 ± 1.5	$1.1^{+0.6}_{-0.6}$	1.0	
				you	20.0	263^{+356}_{-151}	1.7 ± 0.3	1.0	50 ± 31
MIPS0002259_1	0.9500	Synthesizer	$10.4^{+0.1}_{-0.1}$	old	235^{+40}_{-43}	$2.0^{+0.2}_{-0.2}$	$0.1^{+0.1}_{-0.1}$	1.0	
				you	$19.0^{+2.9}_{-3.3}$	1^{+0}_{-0}	$3.0^{+0.3}_{-0.2}$	1.0	6^{+4}_{-1}
		CIGALE	10.5 ± 0.1	old	100^{+0}_{-0}	2.4 ± 0.8	$0.0^{+0.0}_{-0.0}$	1.0	
				you	20.0	31^{+41}_{-17}	2.8 ± 0.2	1.0	13 ± 10
MIPS0002824_1	1.1000	Synthesizer	$9.8^{+0.1}_{-0.1}$	old	128^{+59}_{-27}	$1.0^{+0.1}_{-0.1}$	$0.0^{+0.1}_{-0.0}$	1.0	
				you	$19.4^{+2.6}_{-3.1}$	16^{+7}_{-3}	$3.0^{+0.5}_{-0.1}$	1.0	40^{+6}_{-5}
		CIGALE	9.9 ± 0.1	old	356^{+1599}_{-291}	2.6 ± 1.7	$0.9^{+1.1}_{-0.9}$	1.0	
				you	20.0	54^{+41}_{-23}	2.9 ± 0.2	1.0	69 ± 24
MIPS0009184	0.9000	Synthesizer	$10.5^{+0.1}_{-0.1}$	old	185^{+37}_{-84}	$3.0^{+0.4}_{-0.3}$	$0.0^{+0.1}_{-0.0}$	1.0	
				you	$15.9^{+2.0}_{-1.7}$	200^{+24}_{-22}	$1.0^{+0.1}_{-0.0}$	1.0	60^{+2}_{-4}
		CIGALE	10.5 ± 0.2	old	1384^{+6195}_{-1131}	4.2 ± 1.6	$0.5^{+0.4}_{-0.4}$	1.0	
				you	20.0	132^{+123}_{-63}	1.0 ± 0.1	1.0	52 ± 29
MIPS0009498	1.1000	Synthesizer	$10.5^{+0.1}_{-0.1}$	old	145^{+49}_{-46}	$1.3^{+0.3}_{-0.4}$	$0.1^{+0.1}_{-0.1}$	1.0	
				you	$18.0^{+3.3}_{-3.0}$	72^{+22}_{-23}	$1.9^{+0.1}_{-0.1}$	1.0	34^{+8}_{-14}
		CIGALE	10.7 ± 0.1	old	806^{+3738}_{-663}	3.8 ± 1.4	$0.9^{+0.6}_{-0.6}$	1.0	
				you	20.0	251^{+245}_{-124}	1.8 ± 0.2	1.0	57 ± 28
MIPS0010330	1.1700	Synthesizer	$10.6^{+0.1}_{-0.1}$	old	107^{+31}_{-15}	$1.0^{+0.2}_{-0.1}$	$0.5^{+0.1}_{-0.2}$	1.0	
				you	$18.8^{+2.9}_{-3.1}$	64^{+26}_{-27}	$2.5^{+0.1}_{-0.1}$	1.0	30^{+15}_{-10}
		CIGALE	10.9 ± 0.1	old	231^{+660}_{-171}	3.5 ± 1.6	$0.7^{+0.7}_{-0.7}$	1.0	
				you	20.0	266^{+354}_{-152}	2.3 ± 0.1	1.0	49 ± 25
MIPS0014675_1	1.0200	Synthesizer	$10.2^{+0.0}_{-0.1}$	old	160^{+30}_{-24}	$1.0^{+0.1}_{-0.1}$	$0.0^{+0.1}_{-0.0}$	1.0	
				you	$17.5^{+3.5}_{-2.7}$	57^{+16}_{-13}	$1.6^{+0.1}_{-0.1}$	1.0	39^{+7}_{-9}
		CIGALE	10.4 ± 0.2	old	1464^{+6368}_{-1191}	3.2 ± 1.6	$0.9^{+0.6}_{-0.6}$	1.0	
				you	20.0	122^{+174}_{-72}	1.6 ± 0.4	1.0	53 ± 29
MIPS0014844_1	1.1300	Synthesizer	$10.0^{+0.1}_{-0.1}$	old	163^{+50}_{-39}	$1.0^{+0.1}_{-0.1}$	$0.1^{+0.4}_{-0.1}$	1.0	
				you	$16.7^{+3.2}_{-2.2}$	17^{+8}_{-3}	$2.9^{+0.1}_{-0.1}$	1.0	67^{+4}_{-7}
		CIGALE	10.2 ± 0.2	old	1050^{+4900}_{-864}	3.2 ± 1.6	$1.6^{+0.9}_{-0.9}$	1.0	
				you	20.0	51^{+39}_{-22}	2.7 ± 0.1	1.0	65 ± 26
MIPS0019428	0.9600	Synthesizer	$11.1^{+0.1}_{-0.2}$	old	134^{+107}_{-38}	$4.4^{+0.9}_{-0.9}$	$1.2^{+0.2}_{-0.6}$	1.0	
				you	$18.0^{+3.3}_{-2.8}$	83^{+19}_{-32}	$1.8^{+0.1}_{-0.1}$	1.0	20^{+6}_{-5}
		CIGALE	10.9 ± 0.2	old	2297^{+8467}_{-1807}	3.0 ± 1.0	$1.1^{+0.7}_{-0.7}$	1.0	
				you	20.0	103^{+203}_{-68}	1.9 ± 0.7	1.0	25 ± 26

Continued in the next page

Table5 – continued from previous page

Galaxy	z^{\dagger}	Code	$\log M_{\star}$ [M_{\odot}]	Pop.	τ old [Myr] you [Gyr]	Age old [Gyr] you [Myr]	A_V [mag]	Z [Z_{\odot}]	b [%]
(1)	(2)	(3)	(4)	(5)	(6)	(7)	(8)	(9)	(10)
MIPS0019443	1.0800	Synthesizer	$10.0^{+0.1}_{-0.1}$	old	106^{+53}_{-14}	$1.0^{+0.4}_{-0.1}$	$0.0^{+0.1}_{-0.0}$	1.0	
				you	$17.1^{+3.4}_{-2.4}$	24^{+8}_{-8}	$2.8^{+0.1}_{-0.1}$	1.0	46^{+10}_{-7}
		CIGALE	10.3 ± 0.1	old	876^{+4214}_{-725}	3.2 ± 1.6	$1.5^{+0.9}_{-0.9}$	1.0	
MIPS0021613_1	1.1400	Synthesizer	$10.7^{+0.1}_{-0.1}$	old	118^{+29}_{-21}	$1.5^{+0.2}_{-0.3}$	$0.3^{+0.2}_{-0.1}$	1.0	
				you	$18.6^{+3.1}_{-2.9}$	63^{+22}_{-18}	$2.6^{+0.1}_{-0.1}$	1.0	27^{+13}_{-8}
		CIGALE	10.9 ± 0.2	old	120^{+103}_{-56}	2.9 ± 1.7	$0.2^{+0.3}_{-0.2}$	1.0	
MIPS0022473	1.1500	Synthesizer	$10.8^{+0.1}_{-0.1}$	old	125^{+82}_{-30}	$1.6^{+0.9}_{-0.3}$	$0.0^{+0.1}_{-0.0}$	1.0	
				you	$17.9^{+3.3}_{-2.9}$	255^{+89}_{-64}	$1.0^{+0.1}_{-0.1}$	1.0	65^{+5}_{-10}
		CIGALE	10.9 ± 0.1	old	1239^{+5581}_{-1014}	3.7 ± 1.4	$0.5^{+0.3}_{-0.3}$	1.0	
MIPS0022520_2	1.1800	Synthesizer	$10.5^{+0.1}_{-0.2}$	old	131^{+80}_{-33}	$1.5^{+0.3}_{-0.3}$	$1.1^{+0.4}_{-0.9}$	1.0	
				you	$18.5^{+3.2}_{-3.2}$	68^{+26}_{-29}	$1.4^{+0.1}_{-0.1}$	1.0	35^{+11}_{-8}
		CIGALE	10.5 ± 0.2	old	1265^{+5732}_{-1036}	3.2 ± 1.6	$0.8^{+0.5}_{-0.5}$	1.0	
MIPS0024399_1	1.1900	Synthesizer	$11.0^{+0.1}_{-0.1}$	old	141^{+53}_{-38}	$1.5^{+0.4}_{-0.2}$	$0.1^{+0.1}_{-0.1}$	1.0	
				you	$19.6^{+2.8}_{-2.6}$	602^{+189}_{-147}	$3.1^{+0.3}_{-0.2}$	1.0	61^{+5}_{-5}
		CIGALE	11.1 ± 0.1	old	100^{+0}_{-0}	3.2 ± 1.6	$0.3^{+0.3}_{-0.3}$	1.0	
MIPS0027217_1	1.0200	Synthesizer	$10.8^{+0.1}_{-0.1}$	old	204^{+56}_{-81}	$1.0^{+0.1}_{-0.1}$	$1.3^{+0.1}_{-0.2}$	1.0	
				you	$18.2^{+3.4}_{-3.0}$	69^{+27}_{-29}	$1.9^{+0.1}_{-0.1}$	1.0	15^{+6}_{-5}
		CIGALE	11.0 ± 0.1	old	2115^{+8163}_{-1680}	3.6 ± 1.5	$1.4^{+0.7}_{-0.7}$	1.0	
MIPS0027657_3	1.1900	Synthesizer	$10.9^{+0.1}_{-0.1}$	old	158^{+72}_{-52}	$1.5^{+0.3}_{-0.2}$	$1.5^{+0.1}_{-0.1}$	1.0	
				you	$18.2^{+3.2}_{-3.1}$	74^{+22}_{-19}	$2.0^{+0.1}_{-0.2}$	1.0	17^{+7}_{-6}
		CIGALE	10.9 ± 0.1	old	1901^{+7377}_{-1511}	3.4 ± 1.6	$1.4^{+0.7}_{-0.7}$	1.0	
MIPS0033008	1.1900	Synthesizer	$11.1^{+0.1}_{-0.2}$	old	179^{+79}_{-77}	$3.8^{+1.1}_{-1.2}$	$1.3^{+0.2}_{-1.0}$	1.0	
				you	$17.4^{+3.5}_{-2.6}$	199^{+75}_{-95}	$1.0^{+0.1}_{-0.1}$	1.0	36^{+9}_{-7}
		CIGALE	10.9 ± 0.2	old	1686^{+7017}_{-1360}	3.3 ± 1.6	$0.4^{+0.3}_{-0.3}$	1.0	
				you	20.0	143^{+254}_{-91}	0.9 ± 0.3	1.0	32 ± 28

This paper has been typeset from a \LaTeX file prepared by the author.